UoC

IESL- FORTH

UNIVERSITY OF CRETE – DEPARTMENT OF MATERIALS SCIENCE & TECHNOLOGY

INSTITUTE OF ELECTRONIC STRUCTURE AND LASER-FOUNDATION FOR RESEARCH AND TECHNOLOGY

BACHELOR THESIS

High-resolution and large volume 3D porous media through beam interference nonlinear laser additive manufacturing with applications in photocatalysis.

MISDANITIS KONSTANTINOS
UNIVERSITY NUMBER: 1420

Supervisor: Prof. Tzortzakis Stelios

Ultrashort Nonlinear Laser Interactions and Sources research Lab

Heraklion, February 2022

Table of contents

Acknowledgments 4
Abstract 5
State of the art 6
PART I - THEORETICAL BACKGROUND 8
Chapter 1: Direct Laser Writing by Multi-photon polymerization 9
1.1 Direct Laser Writing 9
1.2 Two- photon absorption 10
1.3 Femtosecond Laser 12
1.4 Photopolymerization 12
1.5 Diffraction limit 14
1.6 Photoinitiators 15
1.7 Material Synthesis (SZ2080) 16
1.8 Direct Laser Writing Long processing time problem 17
Chapter 2: Laser Beam Shaping 19
2.1 Laser Beam Shaping 19
2.2 4f optical system 21
2.3 Spatial Light Modulator 22
Chapter 3: Multiple-beam Interference 25
3.1 Wave Interference 25
3.2 Multiple-Beam Interference 26
3.2.1 Two beams Interference 26
3.2.2 Three beams Interference 27
3.2.3 Four beams Interference 27
3.2.4 Five beams Interference 28
Chapter 4: Pulsed Laser Deposition 29
4.1 Pulsed laser deposition 29
4.2 Ablation mechanism 30
Chapter 5: Photocatalysis and ZnO nanorods 33
5.1. Photocatalysis 33
5.2. ZnO nanorods 34
PART II – EXPERIMENTAL PART 36
Chapter 6: Experimental generation of Multi-beam Interference patterns 37
6.1. Introduction 37

6.2. Experimental Set-up 38
6.3. Imaging Results 38
6.3.1. Two beams 38
6.3.2 Three beams 42
6.3.3 Four beams 46
6.3.4 Five beams 54
Chapter 7: Multiple-Beam Interference Laser Lithography 60
7.1 Introduction 60
7.2 Experimental set-up 60
Sample preparation 61
7.3 Results 62
7.3.1 Fabrication of the 3D porous periodic structure by Multi-Beam Interference Lithography 62
Chapter 8: Pulsed Laser Deposition and ZnO growth results 70
8.1 Pulsed Laser Deposition technique 70
8.1.1 Experimental process and set-up 70
8.1.2 Results 72
8.1.2.1 Deposition of thin fim of Zn in polymer film 72
8.1.2.2 Deposition of thin film of Zn in the three-dimensional porous 73
structures. 73
8.2 ZnO growth technique 74
8.2.1 Aqueous Chemical Growth 74
8.2.1 Aqueous Chemical Growth Process 74
8.2.1.1 Aqueous Chemical Growth on polymer film 75
8.2.1.2 Aqueous Chemical Growth on the fabricated three-dimensional porous structure 77
Chapter 9 : Photocatalytic activity Results 78
9.1 Introduction 78
9.2 Experimental Set -up 78
9.3 Methylene blue photodegradation Results 79
Chapter 10 : Future Work 81
10.1 Introduction 81
10.2 Creation of 3D printed grid substrates 82
10.3 Deposition of a thin film of Zn via PLD in the 3D printed substrates 88
Chapter 11: Conclusion 90
References 91

Acknowledgments

The accomplishment of this bachelor thesis would not have been possible without the support and guidance of some people. So, I would like, as a minimum sign of gratitude, to give them a warm "thank you" for the help and knowledge they provided me.

First and foremost, I would like to express my deepest appreciation to Prof. Stelios Tzortzakis who gave me the opportunity to collaborate and be part of his research group during my thesis (Ultrashort Nonlinear Interactions and Sources research group). His support, his practical and efficient guidance in any research topic that appeared helped me not only to complete my thesis but also in my way of thinking. The motivation and the push that give me through my work make me more motivated for success and I hope to collaborate with Prof. Tzortzakis again in the future.

Next, I will be always indebted to Dr. Mary Manousidaki. From the beginning of this thesis, Dr. Manousidaki Mary was by my side, providing all the appropriate tools to achieve my goal. From knowledge sharing, laughs, adages and support in difficult occasions. I think we were a pretty good team and I wish her the best.

Moreover, I am deeply grateful to all members of the research group (UNIS) for all the help and fun moments that we share throughout my time in the lab. Also, I would like to thank Dr. Farsari Maria, Dr. Klini Argyro and Mr. Syngelakis Ioannis for all the help that provide to me in crucial moments of this thesis.

Last but not least, I want to thank my family and friends for their support and endless love that give me during this bachelor thesis. They were always believed in me and I will never disappoint them!!

Abstract

Direct Laser Writing (DLW) by Multi-photon polymerization is a well-established technique for the fabrication of sub-100nm resolution three-dimensional structures. In particular, the beam of an ultrafast laser is tightly focused into the volume of a transparent, photosensitive material, and the polymerization process can be initiated by nonlinear absorption only within the focal volume pixel. However, this technique considers to be time-consuming when the fabrication of large and complex area structures for realistic applications is required, due to the point-by point laser writing configuration. In this bachelor thesis, we propose Multi-beam Interference Lithography as an approach for reducing the processing time, and we employ this method for the fabrication of centimeter-scale area complex micro-featured porous structures for Photocatalysis applications.

Until now, the fabrication of structures by DLW for practical applications such as photocatalysis, usually do not exceed a surface of more than a few square millimeters area due to long processing time difficulties. To surpass these limitations, and achieve rapid fabrication of centimeter-scale area nanomaterial-coated micro-featured structures, that can present strong photocatalytic activity due to high active surface area, we propose the fabrication of large area porous structures by Multiple-beam Interference Laser lithography. Multi-beam interference is a method that permits the creation of periodic laser patterns due to the intensity distribution of the interfering beams. Here, we properly shaped the laser beam profile, generating different interference patterns from two to five interfering beams. The shaping of the laser beam was achieved with the use of a Liquid Crystal on Silicon-Spatial Light Modulator (LCOS-SLM) while the generated interference patterns in combination with a high nano-accuracy translation stages system were employed for the fabrication of the porous periodic three-dimensional structures. The proposed method offers 100 times faster fabrication of 3D porous structures in comparison with the conventional point-by-point DLW, and 20 times higher resolution (1μm) than the state-of -the-art commercially available 3D printer.

For the Photocatalysis application, ZnO nanorods were grown onto the surface of the structures. Pulsed Laser Deposition (PLD) technique followed by Aqueous Chemical Growth (ACG) were used for ZnO nanorods growth. The photocatalytic activity of the ZnO NRs-coated 3D porous media, was quantified by studying the photodegradation rate of organic pollutants over time under UV light irradiation.

State of the art

Although Direct Laser Writing by Multi-photon polymerization has been regarded as a powerful method for many applications, the long processing time will be the most obstacle when the fabrication of large-scale area and volume of complex micro-featured structures is required. During the years, several fabrication techniques, including multi-foci,[14] holographic lithography[15], shaped laser beams, multi-beam interference [24], and focal beam engineering [51] has been proposed to address the need for faster fabrication and more complex designs. In multi-foci based on an SLM, a femtosecond laser beam is modulated to a predesigned 2D multi-foci pattern. In addition, rapid fabrication of 3D microstrucures is achieved but certain limitations such as low spot numbers and problem with their interfernce due to the produced spectral noise among the spots. *In this thesis, we propose Multiple-Beam Laser Interference Lithography as a method for the high-resolution fabrication of large and complex periodic microstructures with low fabrication time. The rapid fabrication of periodic three-dimensional porous microstructures was achieved by Multiple-Beam Laser Interference Lithography and this promising method accelerated the processing time up to 100 times in comparison with the conventional point-by-point DLW technique, offering a high fabrication resolution of 1μm. The photocatalytic efficiency of the 3D porous media was tested and the photodegradation constant rate of methylene blue was quantified to be* k_{work} *=0.0241* min^{-1}.

Christian Maibohm et.al., in [52] showed that they fabricated a 3D grid structure covering an area of 450 × 450 x 15 μm by multi-foci lithography with a total fabrication time of 37 mins. In our work, we demonstrated that by using Multi-beam Interference Lithography we fabricated a fully 3D complex porous periodic structure of 450 x 450 x 108 μm within a total fabrication time of 3.28 minutes.

After the achievement of the cm scale complex periodic microstructures, the growth of ZnO Nanorods for testing the photocatalytic activity of the 3D porous media was followed. Taking as a reference the following work [38], in which the photocatalytic activity of 3D nanodevices of an array of 490x490 μm was showed, we studied the photocatalytic activity of our cm scale porous media. If we compare the results from this reference work and the current work, we can observe that indeed there was a similar photocatalytic activity in our case (k_{work} =0.0241 min^{-1} and k_{ref} ≈0.0284 min^{-1}). Correspondingly, in comparison with the most recent photocatalytic studies of ZnO nanorods on top of glass surface, [53] the k rate constant of the MB concentration degradation calculated in this thesis, is considering as a promising result for the photocatalytic activity of the three-dimensional cm scale porous media (k_{work} =0.0241 min^{-1} , k_{ref} ≈0.0170 min^{-1}).

In parallel, comparing the resolution (1μm) achieved in our proposed method, with the state-of-the-art commercially available 3D printer, which obtains a resolution of about 20μm, Multi-Beam Interference Lithography can offer remarkable acceleration of complex high-volume 3D media fabrication and high fabrication resolution. 3D printers

have also been proposed for the fabrication of photocatalytic structures. Mathieu Grandcolas et.al in ref [54] showed the fabrication of a 3D 5 x 5 x 5 cm printed porous domain and the photodegradation of Methylene Blue over time under UV light induced by this ZnO coated structure. The results of this bachelor thesis indicated that using Muti-beam Interference Laser Lithography, followed by the two-step procedure for ZnO nanorods growth onto the fabricated structure, the rate constant of decreasing the Methylene Blue concentration was measured to be 2,09 times higher (k_{work} =0.0241 min^{-1} and k_{ref}=0.0115 min^{-1}), showing that our 3D porous media (1cm x 1cm x 108μm) have higher photocatalytic efficiency compared with the 5 x 5 x 5 cm printed porous domain.

PART I - THEORETICAL BACKGROUND

Chapter 1: Direct Laser Writing by Multi-photon polymerization

1.1 Direct Laser Writing

Direct Laser Writing (DLW) by Multi-Photon Polymerization (MPP) is a three-dimensional printing technology which allows the fabrication of readily assembled structures with sub-100nm resolution. It appears to be a remarkable and fast evolutionary technique since it is based on the nonlinear photon absorption by photopolymers. Through DLW, the beam of an ultra-fast laser is tightly focused inside the volume of a transparent photosensitive material giving rise to absorb two or more photons and polymerize locally. MPP and the polymerization process can be initiated by non-linear absorption only within the focal volume pixel (voxel). By point -by-point scanning the voxel in space, following a path derived from a computer designed 3D model, one can thus create arbitrary 3D structures.

Another important point of Direct Laser Writing is that it has plenty applications in fields such as metamaterials, tissue engineering, photocatalysis, photonic crystals, micro-fluids, micro-optics, biomedical implants and 3D models. In the following figures someone can observe fabricated structures using DLW by MPP of the previous applications. [1] , [2], [3]

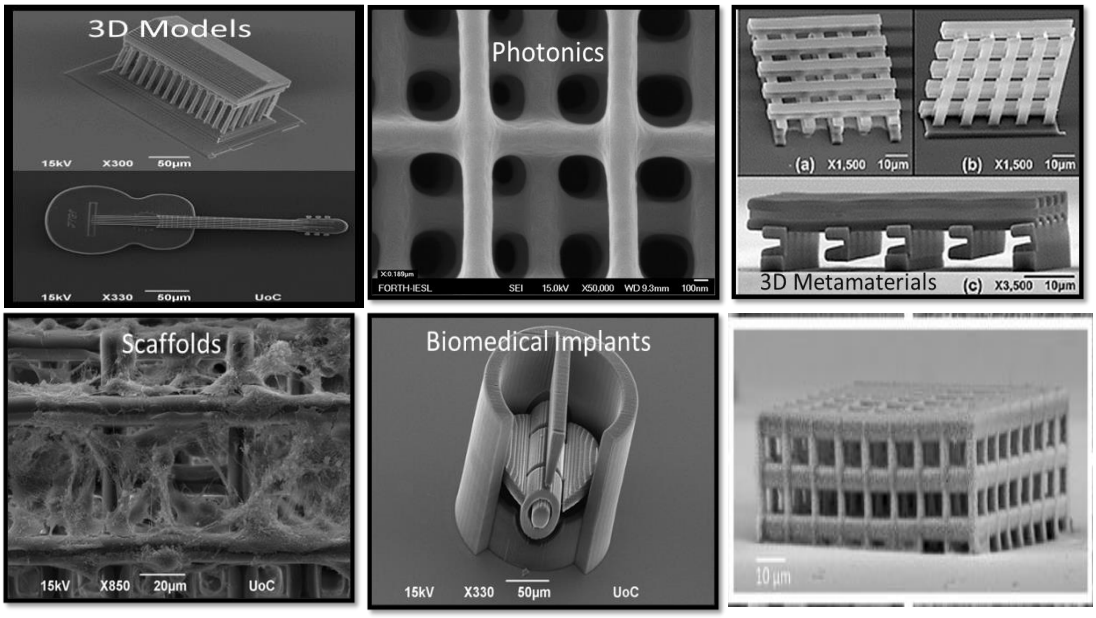

Figure 1.1.1: Presentation of abruptly 3D structures fabricated using MPP via DLW for a variety of applications

In the following figure (1.1.2) a typical Direct Laser Writing experimental set up is presented. [6] Initially a femtosecond laser beam gets tightly focused into the volume of the photosensitive material that is placed on top of a cover glass. Then, by moving the sample through the stages in the three dimensions (X, Y, Z), the development of the desired polymeric structure begins. After the end of the process, the glass where our material is placed to be rinsed in specific solvent which cannot destroy the fabricated structure and during the rinse the non-polymerized material gets removed from the glass and the 3D polymeric structure remains only for further studies. structure.

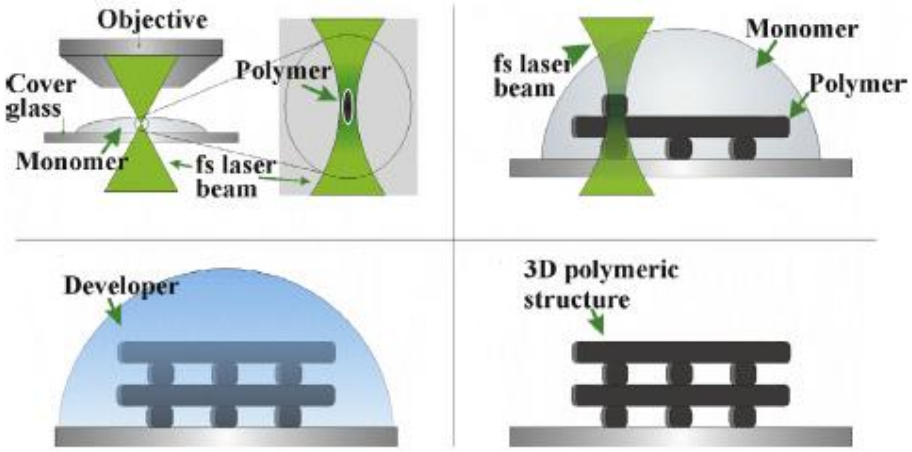

Figure 1.1.2: Schematic illustration of a typical Direct Laser Writing experimental procedure.

1.2 Two- photon absorption

In generally, there are two major categories of two photon absorption. The sequential absorption and the simultaneous absorption. As concern the sequential state the one photon excited in a real intermediate energy state and by this point the second photon gets absorbed. The presence of the intermediate energy state implies that the material absorbs at this specific wavelength; it will therefore be a surface effect and will follow the Beer–Lambert law. [4]

The principles of two-photon polymerization based on the simultaneous absorption which was originally predicted by Göppert-Mayer in 1931 in her doctoral dissertation. It is defined as ‘an absorption event caused by the collective action of two or more photons, all of which must be present simultaneously to impart enough energy to drive a transition’ In this case there is no a real intermediate energy but instead there is a virtual intermediate state and two-photon absorption happens only if another photon arrives within the virtual state lifetime. The lifetime’s order of magnitude can be

predicted from the Heisenberg's uncertainty principle. Considering that the state's energy level should be around 10^{-1} eV, its estimated lifetime is of the order of few femtoseconds. Due to virtual state's short lifetime the cross-section of a simultaneous two photon absorption is small. For the accomplishment of this procedure, it is required to use a tightly focused femtosecond laser beam. The electron transition in this case is caused by two photons of energy *hv*/2 rather than one of energy *hv*. The following figures represent the single photon absorption and the two main categories of the two-photon absorption. [5], [6]

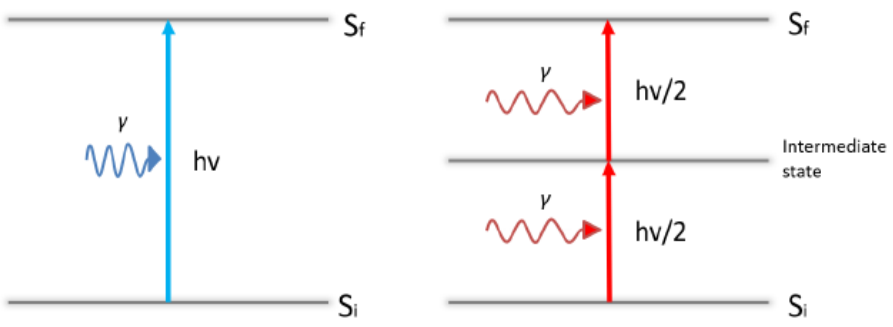

Figure 1.2.1: Illustration of one- photon absorption (left) and two-photon absorption (right).

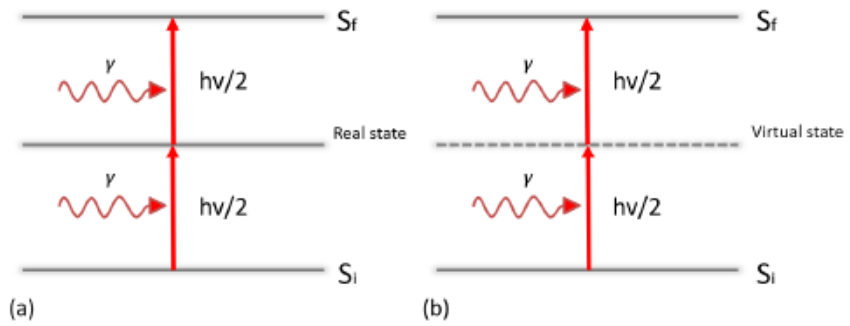

Figure 1.2.2: Sequential two-photon absorption (a)
Simultaneous two- photon absorption (b)

1.3 Femtosecond Laser

A femtosecond laser is a laser which emits optical pulses with a duration well below 1ps (ultrashort pulses), i.e., in the domain of femtoseconds (1fs = 10^{-15} s). It thus also belongs to the category of ultrafast or ultrashort pulse lasers. Femtosecond lasers have a huge variety of applications such as laser material processing, medical applications, laser microscopy, measurements and telecommunications. Femtosecond lasers have the advantage of producing very short pulses in order of a few tens of femtoseconds so that they cannot cause any thermal damage in the material. Also taking into advantage the wavelength of femtosecond lasers which is twice or bigger of the wavelength required for single photon polymerization of a wide range of photopolymers. Additionally, the majority of photopolymers are transparent at 800nm and that allows the in-volume focusing of the laser beam with minimal scattering [7] , [47].

1.4 Photopolymerization

Polymerization is a process in which monomer molecules are connected with bonds to form polymer molecules. In the case of photopolymerization, light irradiation of a tightly focused laser beam provides the energy needed to induce the conversion of small unsaturated molecules in the liquid state to solid macromolecules through polymerization reactions. The monomers can be solidified in two main ways after being excited by light: polymerization and crosslinking. The chain reaction from which macromolecules are generated is an important aspect of polymerization, however cross linking is mainly concerned with the production of crosslinking with chemical bonds.

In generally, polymerization is realized through chain reactions where M is a monomer unit and M_n is the macromolecule containing n-monomer units.

$$M \xrightarrow{M} M_2 \xrightarrow{M} M_3 \xrightarrow{M} \dots M_{n-1} \xrightarrow{M} M_n,$$

Figure 1.4.1: General idea of polymerization

To improve photopolymerization efficiency, low weighing photosensitive molecules can be inserted to the material. Photo initiators are compounds that can absorb light irradiation and activate the polymerization process through excitation and decomposition. The initiating species may be radicals, cations, or anions. When the laser is focused tightly into the material, the photo initiator uses to initiate the polymerization will absorb two photons and produce radicals. As the material response is proportional to the square of the intensity, this will only happen at the focal point in which, combined with the fact that the two-photon transition rate is very small, will

provide very high spatial resolution. The radicals that are formed react with monomers or oligomers to produce radical monomers. The procedure is depicted in the figure below. This chain reaction will continue until two radicals meet, and at a certain point the reaction will terminate. An effective initiator has a high quantum yield in the formation of active moieties, is highly soluble in the polymerization medium, and is thermally stable and steady in darkness. Free-radical polymerizations are chain reactions in which the addition of a monomer molecule to an active chain-end regenerates the active site at the chain-end. The free-radical photopolymerization mechanism involves at least three different kinds of reactions: Initiation, propagation and termination.

Initiation	$I \xrightarrow{hv+hv} I^{*} \longrightarrow R^{\bullet}$	**1**
Propagation	$R^{\bullet} + M \longrightarrow RM^{\bullet} \xrightarrow{M} RMM^{\bullet} \cdots \longrightarrow RM_n^{\bullet}$	**2**
Termination	$RM_n^{\bullet} + RM_m^{\bullet} \longrightarrow RM_{n+m}R$	**3**

Figure 1.4.2: Polymerization process where (I) is the initiator, (R) radical, (M) monomer and the (I*) is the excited state of the photo initiator after the two-photon absorption

- The first step is the initiation during which the free-radical initiator is decomposed with light in the presence of a monomer to form an active species
- In the next step, known as the propagation, the initiator fragment reacts with a monomer molecule to form the first active adduct that is capable of being polymerized. Monomers continue to add in the same manner resulting in the formation of macroradicals which are end-active polymers
- The final step is termination, which involves deactivating the growth center and forming the final polymer molecules. This stage usually entails a reaction between two polymers with active centers, which can take place by using one of two mechanisms: combination or disproportionation, resulting in the production of one or two polymeric chains.

    - Combination termination is known as coupling and occurs when two free radicals join together.
    - Disproportionation termination is when one molecule abstracts a hydrogen atom from the other and the other molecule forms a double bond.

$$RM_n^{\cdot} + RM_m^{\cdot} \rightarrow RM_n + RM_m \qquad RM_n^{\cdot} + RM_m^{\cdot} \rightarrow RM_n\text{-}M_mR$$

Figure 1.4.3: Illustration of a combination termination (left)
Illustration of a disproportionation termination(right)

Finally, except from the referred methods, other reactions, such as chain transfer and chain inhibition sometimes take place and complicate the mechanism of free-radical polymerization. [8] , [5] , [9], [10]

1.5 Diffraction limit

Theoretically, there is a limit of how much a light beam can be focused, thus this should be used to evaluate the fabrication precision. Abbe's diffraction limit implies the highest resolution that a focused laser beam can acquire.

$$Diffraction\ limit = \frac{0.5\times\lambda}{NA}, \quad Diffraction\ limit = \frac{0.5\ x\ 1030}{0.4} = 1287{,}5nm$$

where λ is the laser wavelength and NA is the numerical aperture of the objective lens.[11]

Materials with a well-defined photopolymerization threshold ought to be used to produce 3D structures with in-volume patterning and photopolymerized voxels smaller than those defined by the diffraction limit. Although using multi-photon polymerization, it can be used to circumvent the diffraction limit and produce structures of very high resolution. This can be done by modifying the light intensity at the focal volume in a manner such that the light-produced radicals exceed the quenchers and initiate polymerization only in a region where exposure energy is larger than the threshold. In this case the diffraction limit becomes just a measure of the focal spot size and it does not really determine the voxel size. [5]

Two-photon polymerization (2PP) has been successfully used to produce a variety of photonic and micromechanical devices, since it is currently the only micro-processing technique with intrinsic 3D fabrication capability. When compared to single-photon absorption, which is employed in conventional rapid prototyping, the two-photon process has at least two advantages: [12] [13]

- Since common polymers have little linear absorption in the red, near-infrared region, the laser can penetrate deeply into materials and promote polymerization from inside without contaminating outside of the focal volume

- The quadratic dependence of polymerization rate on light intensity allows for superior 3D spatial resolution and greater accuracy than single photons.

Two-photon microscopy uses a laser to excite a fluorescent tag within a sample and detectors to measure the emitted light. However, the lasers used in two-photon microscopy excite by using near simultaneous absorption of two long wavelength (~800 nm) photons. The long wavelengths used for two-photon microscopy are less damaging and penetrate more deeply into the volume of the material. In addition, the requirement for near simultaneous absorption of two photons means that excitation is only achieved near the focal plane where the laser light is most concentrated. In the following figure the fluorescence from a photopolymer solution, caused by single-photon excitation from a UV lamp and by two-photon excitation from femtosecond laser is presented.

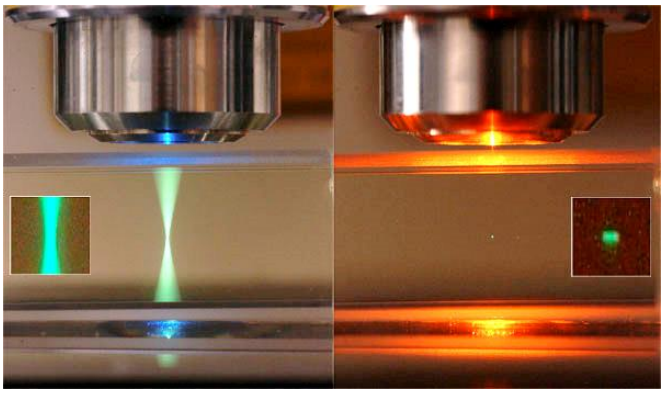

Figure 1.5.1: Fluorescence from a photopolymer solution, caused by single-photon excitation from a UV lamp (left) and by two-photon excitation from femtosecond laser (right).

1.6 Photoinitiators

Photoinitiators are molecules that absorb photons when irradiated with light and form active particles out of the excited state, which initiate sequential reactions. The initial particles may be radicals, cations or anions. Root photoinitiators are widely available. Cationic photoinitiators, mostly chemical salts, as well as iodine salts from and iron complexes, are available in smaller quantities. Benzyl (phenyl-CO-) is a key component of almost all radical photoinitiators. [6],[9] A photoinitiator should exhibit several properties, from which the most important are:

- high absorption at the exposure wavelength and high molar extinction coefficient
- high quantum yield of formation of initiating species
- high reactivity of the radical towards the monomer.

During the experimental part of this bachelor thesis, the organic-inorganic hybrid material SZ2080 was doped by two different types of photo initiators. The first one was the BIS (4, 4'-bis-diethylamino-benzophenone) and the second one was Eosin-Y. The following figures present the absorption spectrum of the upper photoinitiators as long as their chemical formula type.

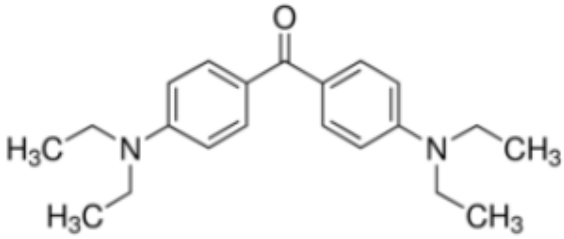

Figure 1.6.1: 4, 4'-bis-diethylamino-benzophenone

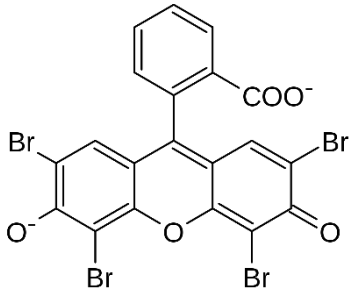

Figure 1.6.2: Eosin Y

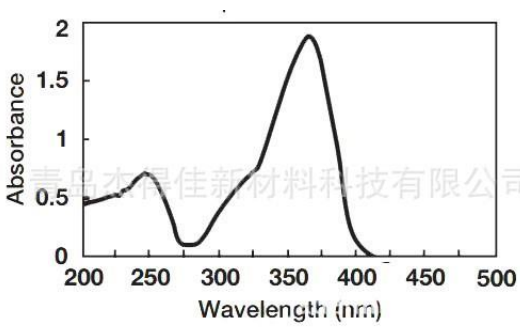

Figure 1.6.3: 4, 4'-bis-diethylamino-benzophenone absorption spectra

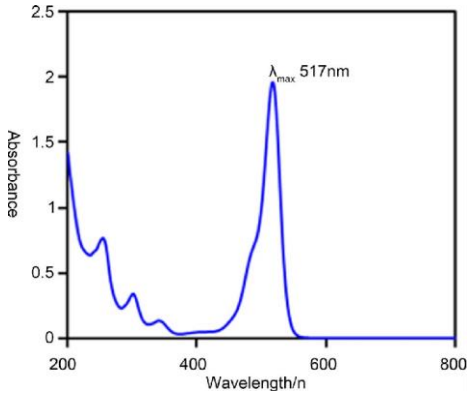

Figure 1.6.4: Eosin Y absorption spectra

1.7 Material Synthesis (SZ2080)

In this thesis the materials which were utilized in order to produce the hybrid organic-inorganic material is the Methacryloxy-Propyltrimethoxysilane (MAPTMS) and methacrylic acid (MAA) as organic monomers, zirconium propoxide (ZPO) for the formation of inorganic network and also 4,4'- Bis(diethylamino) benzophenone (BIS) and Eosyn Y (EOSIN) as photoinitiators. All chemicals were purchased from Sigma-Aldrich.

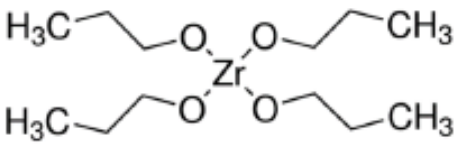

Figure 1.7.1: zirconium propoxide (ZPO)

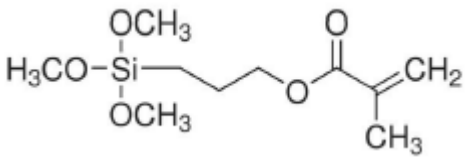

Figure 1.7.2: Methacryloxy-Propyltrimethoxysilane (MAPTMS)

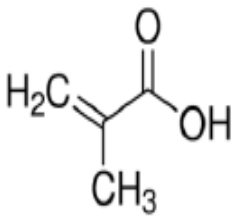

Figure 1.7.3: methacrylic acid (MAA)

For the preparation of the composite, MAPTMS was hydrolyzed using HCl solution (0.1 M) at a ratio of 1:0.1and ZPO was stabilized by MAA (molar ratio 1:1). After 5 minutes, the Zirconium complex was slowly added to the hydrolyzed MAPTMS at a 2:8 molar ratio. Finally, the PI, at a 1% mass ratio to the monomers was added to the mixture. After stirring for 15 minutes further, the composite was filtered using a 0.22 µm syringe filter. The samples were prepared by drop-casting onto 100 micron-thick silanized glass substrates, and the resultant films were dried at 100 °C for 10 minutes before the photopolymerization.

1.8 Direct Laser Writing Long processing time problem

Recently, there is an increasing interest for modification of the conventional (DLW) fabrication technique, as a fundamental aspect for solving important issues such as rapid fabrication, parallel processing, and large-scale structuring or 3D printing engineering. Although Direct Laser Writing by Multi-photon polymerization has been regarded as a powerful method for many applications, the long processing time will be the most obstacle when the fabrication of large-scale area complex micro-featured structures is required.

During the years, several fabrication techniques, including multi-foci,[14] holographic lithography,[15] shaped laser beams, multi-beam interference, and focal beam engineering has been proposed to address the need for faster fabrication times and more complex designs. Driven by the previous, in this thesis we propose Multiple-Beam

Laser Interference Lithography as a method for the fabrication of large and complex periodic microstructures with faster fabrication time than the conventional Direct Laser Writing by Multi-Photon Polymerization. With the use of a Spatial Light Modulator, we are able to shape the laser's beam profile as we apply on the SLM a properly code-generated phase mask in order to generate different interference patterns that were actively employed for the parallel processing of a photosensitive material by MPP. The rapid fabrication of cm-scale periodic three-dimensional porous microstructures was achieved while this promising method accelerated the processing time up to 100 times in comparison with the classic point-point direct laser scanning technique.

Chapter 2: Laser Beam Shaping

2.1 Laser Beam Shaping

The process of redistributing the irradiance and phase of an optical beam is known as beam shaping. The irradiance distribution determines the beam shape while the phase of the shaped beam is a key aspect in determining the beam profile's propagation properties. For example, a large beam with a uniform phase front will maintain its shape over a considerable propagation distance. The beam shaping technology can be applied either in coherent or incoherent beams. A variety of applications included industrial, medical or even military area can benefit from the use of laser beam with specified shape. But there is not only one single beam shaping method that addresses all situations well. Based on that, there is continuous research on phase modulation procedures and optical methods that can redistribute a beam's profile, reshaping its wavefront and modifying the propagation dynamics of this beam. Nowadays, beam shaping composes a significant factor for numerous processes such as lithography, circuit component trimming, laser printing, material processing, optical data storage, optical metrology, medical applications and laboratory research. [16],[17]

To fully understand the process of the beam shaping, we should focus in phase modulation. Taking as an example the Harmonic plane wave equation:

$$U(\boldsymbol{r},t) = u_o e^{i(\boldsymbol{k}\cdot\boldsymbol{r}-\omega t)},\ \boldsymbol{k} \equiv n\frac{2\pi}{\lambda_0}\hat{\boldsymbol{k}}$$

where $\underline{k}$ is the wave vector normal to the wavefront, n is the refractive index, $\underline{u_o}$ is the wave's amplitude and the term $(\boldsymbol{k}\cdot\boldsymbol{r}-\omega t)$ describes the phase of the wave. If now we assume that the wave propagates along z axis:

$$\left.\begin{array}{l}\hat{\boldsymbol{k}} \equiv \hat{\boldsymbol{z}}\,, \\ \boldsymbol{k} \equiv \boldsymbol{n}\,\frac{2\pi}{\lambda o}\hat{\boldsymbol{k}}\end{array}\right\} \qquad \boldsymbol{k} \equiv \boldsymbol{n}\,\frac{2\pi}{\lambda o}\hat{\boldsymbol{z}} \qquad \rightarrow \qquad \boldsymbol{k}\cdot\boldsymbol{r} = \frac{2\pi}{\lambda o}\boldsymbol{n}\cdot\boldsymbol{z}$$

The upper equation corresponds to the optical path. Optical path is the path that light follows when travelling through an optical system. Therefore, the harmonic wave equation becomes:

$$U(\boldsymbol{r},t) = u_o e^{i(\frac{2\pi}{\lambda_0}n\cdot z-\omega t)}$$

We can notice that the modulated phase of a plane wave can be derived by measuring the optical path length that a beam follows when interacts with an optical system. So, it can conclude that the phase is equivalent to the optical path. The latter result facilitates the problem of phase determination for beam shaping. We can shape the wavefront of a beam by spatially controlling the optical path length (OPL) of each point in the

wavefront. The OPL is defined by the product of the refractive index n of a specific medium, with the physical length d of the medium.

$$OPL = n \cdot d$$

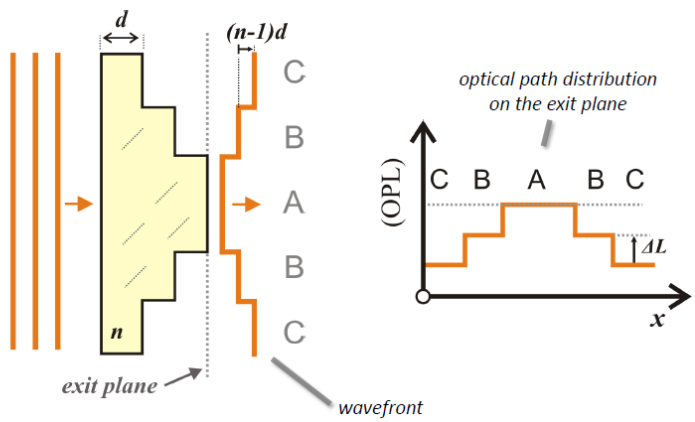

Figure 2.1.1: Illustration of a wavefront shaping example

This is a general wavefront shaping example of a beam due to an optical element is represented. Plane waves incidence upon an optical element with refractive index *n*, and the modulation of the outgoing wavefront due to the different optical path lengths that the light follows point by point, can be seen behind the exit plane. At this point it is interesting to calculate the optical path difference which corresponds to the phase shift that occurs when the wave passed through the material with *n* appearing to travel a greater distance than an identical wave in air. So, we have:

$$\left.\begin{aligned} (OPL)_A &= 3n \cdot d \\ (OPL)_B &= 2n \cdot d + d \\ (OPL)_C &= 2n \cdot d + 2d \end{aligned}\right\} \rightarrow \Delta L = (OPL)_A - (OPL)_B = (OPL)_B - (OPL)_C = (n-1)d$$

where, $\underline{\Delta L}$ is the optical path difference. As a result, controlling the optical path difference we can determine the phase difference and the phase modulation would appear to the beam. One simple method of beam shaping is by spatially controlling the optical path delay of each point in the wavefront.

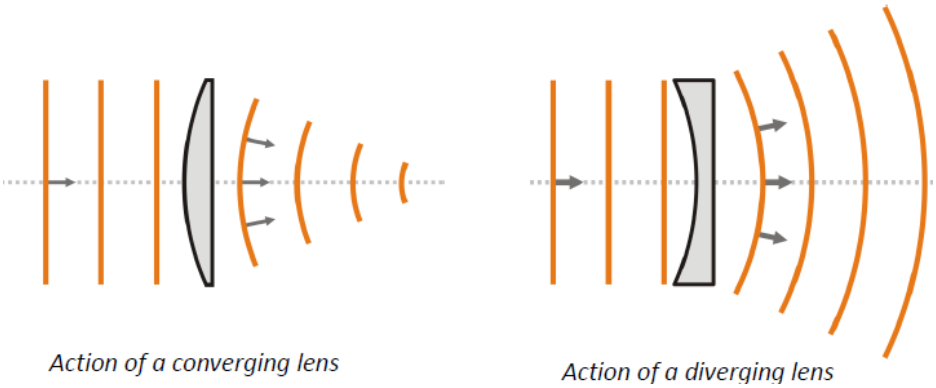

Figure 2.1.2: Schematic illustration of a simple wavefront shaping using a converging or a diverging lens.

Taking as an example , we can use simple lenses and reshape (convert) a plane wavefront to a spherical one as someone can observe in the upper figure. [18]

2.2 4f optical system

The *4f* optical setup is considered with a wave modulation by SLM (spatial light modulator) located in the focal plane of the lens.

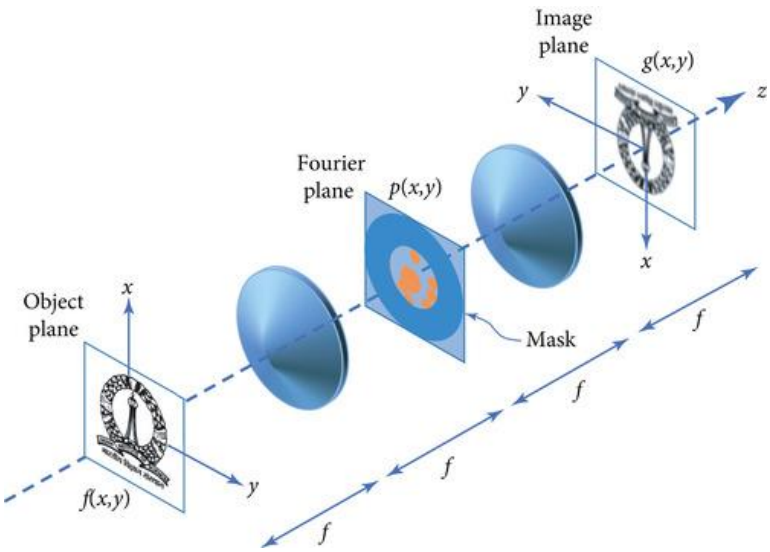

Figure 2.2.1: Basic structure illustration of a 4f optical system

The input plane is one focal length in front of lens 1 while the output plane is located one focal length after lens 2. In between the two lenses, we have the Fourier plane. There is the point where we have the Fourier transformation of the object placed at the output plane. At the Fourier plane, we can place masks of different shapes and opacities that can filter-out unwanted components from our original image. The Fourier transformation of an image is very similar to a diffraction pattern, where low frequency components are located close to the optical axis and higher frequency ones are placed farther away from the origin. The shape of the mask varies depending on the application that we need to proceed. [48], [19]

2.3 Spatial Light Modulator

A Spatial light modulator (SLM) is a device that can alter the amplitude, polarization, and phase of light. SLM technology is based on liquid crystal properties. Essentially, a SLM is a pixelated display constructed with hundreds of thousands of liquid crystal-filled pixels cells that are self-contained and controllable. Spatial light modulators are also used to spatially modify an optical wavefront into almost any desired field distribution, while it can replace the dynamic operation of every optical element such as lenses, axicon, grating etc. There is a broad categorization of SLMs into two classes that can be made at the start. The first one is electrically addressed SLMs and the second by optically addressed SLMs. In the first case, electrical signals representing the information to be input to the system directly drive a device in such a way as to control its spatial distribution of absorption or phase shift. In the latter case, the information may be input to the SLM in the form of an optical image at the start rather than in electrical form.

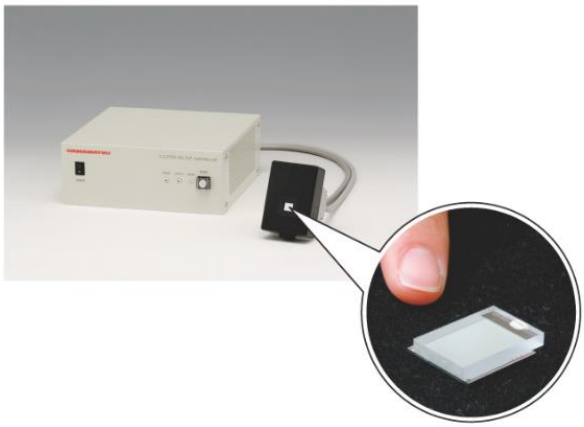

Figure 2.3.1: Illustration of a LCOS-SLM (Hamamatsu LCOS-X10468-2) that has been used for this bachelor thesis.

In this bachelor thesis, a Liquid Crystal on Silicon) phase only reflecting Spatial Light Modulator (LCOS-SLM is being employed (Figure 2.3.1). The LCOS-SLM (Liquid Crystal on Silicon-Spatial Light Modulator) is a reflection type spatial light modulator that freely modulates the light phase as needed. A laser beam incident to the LCOS-SLM is phase-modulated and then reflected to freely control the wavefront of (reflected) light as needed. This ability to accurately control the light wavefront makes the LCOS-SLM ideal for applications such as optical beam pattern forming.

The phase of the laser beam can be controlled in two dimensional by a structure in which liquid crystal is sandwiched between a CMOS chip in which pixel electrodes are arranged in two dimensions and a transparent electrode deposited on a glass substrate. The digital images output from the PCs are converted to analog signals by a dedicated drive circuit, and voltage is applied to the pixel electrodes on CMOS chip. [20] ,[21],[22] ,[18]

In the following figures there is a schematic illustration of how a Liquid Crystal on Silicon- Spatial Light Modulator operates. (See figure 2.3.2 and 2.3.3).

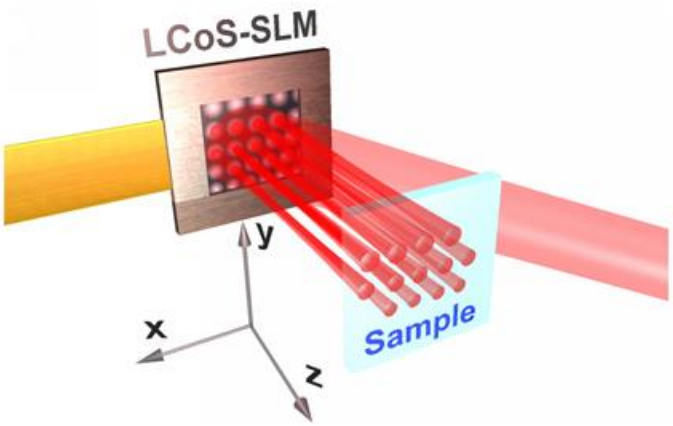

Figure 2.3.2: Liquid crystal Spatial Light Modulator.

.

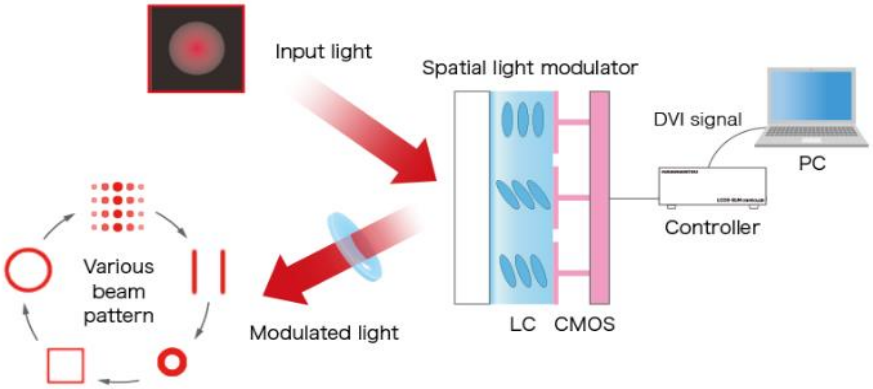

Figure 2.3.3: Side view of a LCOS modulator with nematic liquid crystals.

In the next figure (2.3.4) we present examples of various beam patterns after the initial laser beam entered into the LCOS- SLM. The first example is a non-diffracting Bessel beam generated by a diffractive axicon. The second example is an Airy beam generated by a diffractive cubic phase mask in the back focal plane of a convex lens. Finally, the last example is an optical vortex beam generated by a helical phase mask and focused by a lens. [22]

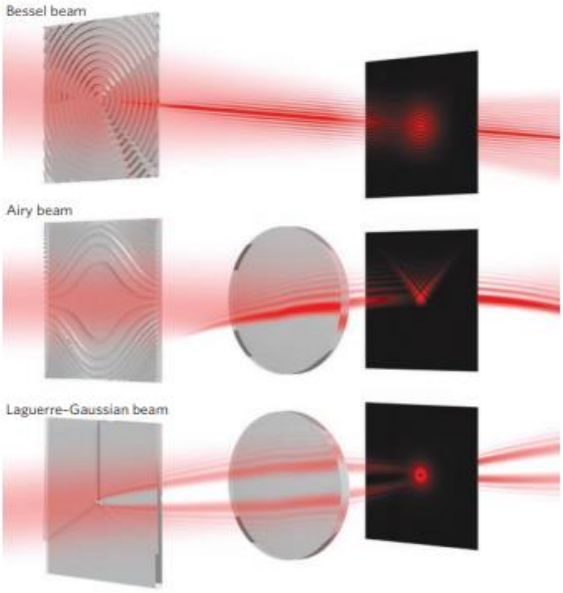

Figure 2.3.4: Characteristic examples of laser shaped beam by a Spatial Light Modulator (SLM).

Chapter 3: Multiple-beam Interference

3.1 Wave Interference

When two or more optical waves are presented simultaneously in the same region of space, the waves interfere and generate a periodic spatial modulation of light. There are two major categories of interference: constructive and destructive interference. Constructive interference occurs when the maxima of two waves add together (the two waves are in phase), so that the amplitude of the resulting wave is equal to the sum of the individual amplitudes. Destructive interference occurs when the maxima of two waves are out of phase (pi phase) and a positive displacement of one wave is cancelled exactly by a negative displacement of the other wave and so the amplitude of the resulting wave is zero. In the following figure the two main categories of interference are presented. [23]

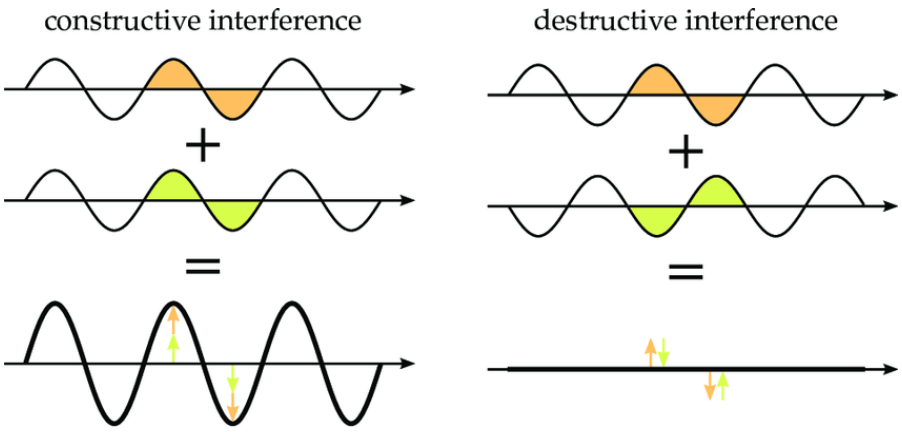

Figure 3.1.1: Illustration of wave interference categories.

3.2 Multiple-Beam Interference

When there are two disturbances near one another and their respected series of waves overlap this is called an interference pattern. A light wave can be described by its frequency, amplitude, phase and the resulting interference pattern between two waves shall be depended on these properties too.[24] Each plane wave may be defined by

$$Ei(r,t) = Eicos(\omega t - k_i \cdot r + \varphi_i)\, \hat{e_i}$$

, where Ei is the amplitude, ω is the frequency, k_i is the wavevector, φ_i is the phase and $\hat{e_i}$ represents the linear polarization vector, and i = 1,2. In generally, interference among any N (≤4) collimated, coherent laser beams produce an intensity grating with (N≤1) dimensional periodicity if the difference between the wave vectors is non-coplanar. The interference of the two plane waves produces a one-dimensional (1D) fringe pattern, three-beam interference produces up to three 1D fringe patterns that combine to form a two-dimensional (2D) pattern, four-beam interference provides three-dimensional (3D) patterning with up to six interfering beam pairs. Increasingly complex designs are realized as the number of interfering beams increases and elliptical or circular beam polarizations are considered. [25]

3.2.1 Two beams Interference

The cosine term in intensity function for two beam interference describes a periodic intensity function that when it is recorded on a substrate forms fringes at the incident plane. In the following figure we observe two linear polarized beams with wavelength λ, polarization vectors êi and wavevectors ki, interfere at an angle θ and form fringes at the x-y plane. [26]The periodicity can be calculated by the equation: $\Lambda = \frac{\lambda}{2sin\theta}$

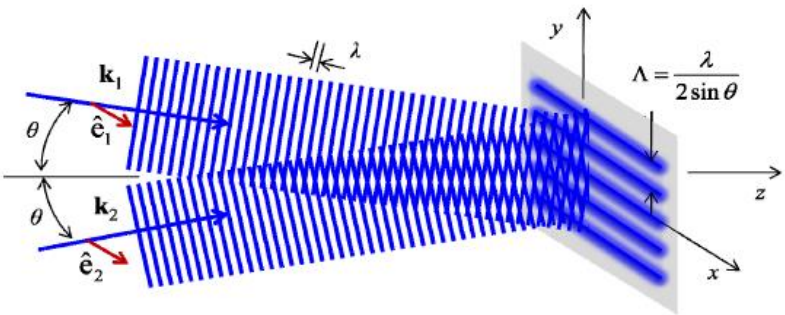

Figure 3.2.1.1: Schematic illustration of a two-beam interference.

3.2.2 Three beams Interference

In the scenario of three-beams interference, it can form a more complex design than the previous occasion because it is depending by the way of the interaction since each of the beam pair forms a one-dimensional interference fringe pattern and the combination between them leads to the creation of the square lattice symmetries. Characteristic examples of this procedure are the formation of a p4m symmetry and cmm symmetry as described later in the figure. [26]

As concern the periodicity, the equivalent equation is: $\Lambda = \frac{\lambda}{\sqrt{2}sin\theta}$

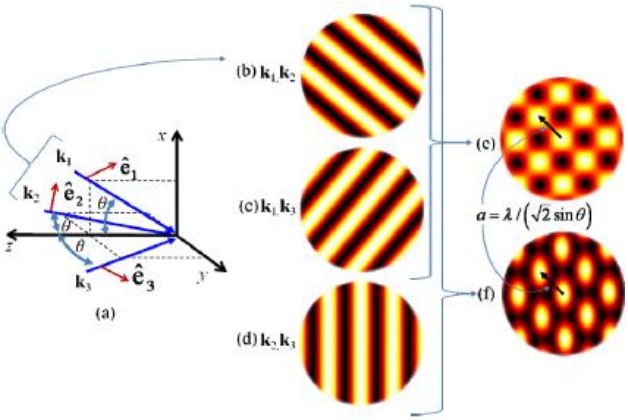

Figure 3.2.2.1: Three beam interference and the two categories of pattern formation

3.2.3 Four beams Interference

Four beams interference has become a powerful tool in the fabrication of various three-dimensional structures. In generally, four-beam interference form a square lattice symmetry pattern. But in some cases, blocking the proper beams we can observe either two or three interference behavior. [27] The periodicity of the four-beams interference is given by the equation: $\Lambda = \frac{\sqrt{2}\lambda}{2sin\theta}$

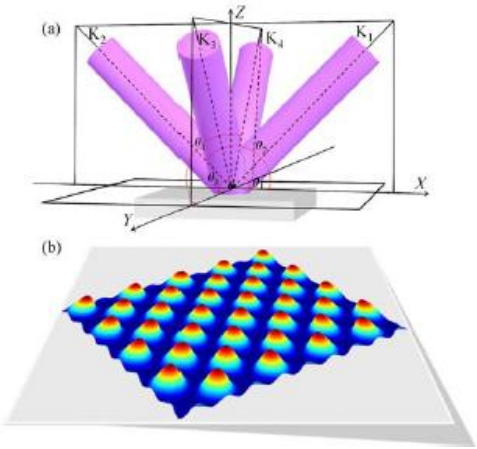

Figure 3.2.3.1: a) Four beams interference b) Four beams interference pattern

3.2.4 Five beams Interference

When four symmetrical beams and one central beam interfere with each other, the expected interference pattern is remarkably similar to the interference pattern of three beam interference. A 1D fringe pattern is generated when three of the five beams interact. When the rest two beams contact the pattern is similar to the pattern formed in two-beam interference. Finally, the combination of these designs creates a square lattice with p4m plane group symmetry. [28]In five-beams interference pattern the periodicity is different along x-y axis and z axis which described by:

$$\Lambda(x,y) = \frac{\lambda}{sin\theta}, \Lambda(z) = \frac{\lambda}{1 - cos\theta}$$

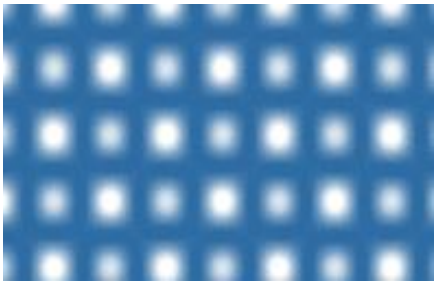

Figure 3.2.4.1: Five-beams interference

Chapter 4: Pulsed Laser Deposition

4.1 Pulsed laser deposition

Pulsed laser deposition (PLD) is a physical vapor deposition technique where a high-power pulsed laser beam is focused to strike a target of the desired composition. Material is then vaporized and deposited as a thin film on a substrate facing the target. This process can occur in ultra-high vacuum or in the presence of a background gas, such as oxygen when depositing films of oxides. Light is absorbed by material, and the outcome is governed by the value of incident laser power density in relation to an ablation threshold. The laser pulse would just heat the target if the laser fluence (laser power density) was less than the ablation threshold. The ablation threshold is determined by the target material, its absorption coefficient, the wavelength and duration of the laser pulse. Only when the laser fluence is high enough to pass through the ablation threshold does the target material vaporize. A finite volume of solid target material is converted into vapor phase elements such as ions and neutrals, forming a high-temperature "plasma plume". The ablation plume then expands adiabatically, moving vapors from the target material to the substrate in this fashion. Finally, the material flow required for film growth is provided by the recondensation of this plasma plume and a substrate is placed across to the target at a distance of a few centimeters. [29],[30] ,[31] ,

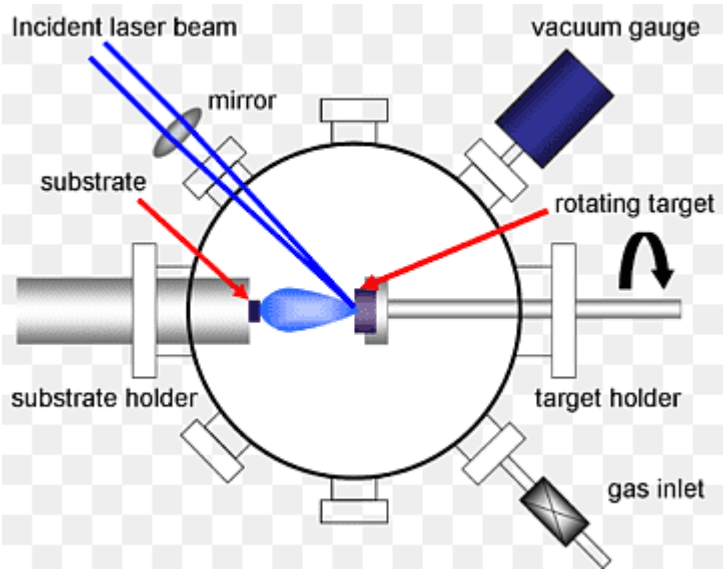

Figure 4.1.1: Schematic illustration of a typical Pulsed Laser Deposition experiment and the mechanisms that occur during an experiment.

Laser ablation for thin film growth has many advantages against classical thermal growth techniques like chemical vapor deposition (CVD), metalorganic chemical vapor deposition (MOCVD) or ion-beam growth techniques like molecular beam epitaxy (MBE). Examples of the advantages that laser ablation are:[32],

- the energy source is outside the vacuum chamber which, in contrast to vacuum-installed devices, provides a much greater degree of flexibility in materials use and geometrical arrangements
- almost any condensed matter material can be ablated
- the pulsed nature of PLD means that film growth rates may be controlled to any desired amount
- the amount of evaporated source material is localized only to that area defined by the laser focus
- under optimal conditions, the ratios of the elemental components of the bulk and film are the same, even for chemically complex systems
- the kinetic energies of the ablated species lie mainly in a range that promotes surface mobility while avoiding bulk displacements
- the ability to produce species with electronic states far from chemical equilibrium opens up the potential to produce novel or metastable materials that would be unattainable under thermal conditions.

4.2 Ablation mechanism

The ablation of the target material by laser irradiation, the development of a plasma plume with high energetic ions, electrons, and neutrals, and the crystalline growth of the film itself on the heated substrate are all very complex mechanisms. The PLD technique can be divided into four stages:[33],[34]

1. Laser light absorption by a target material
2. Formation of a plasma plume
3. Expansion of this plasma plume
4. Material deposition on a substrate for film growth.

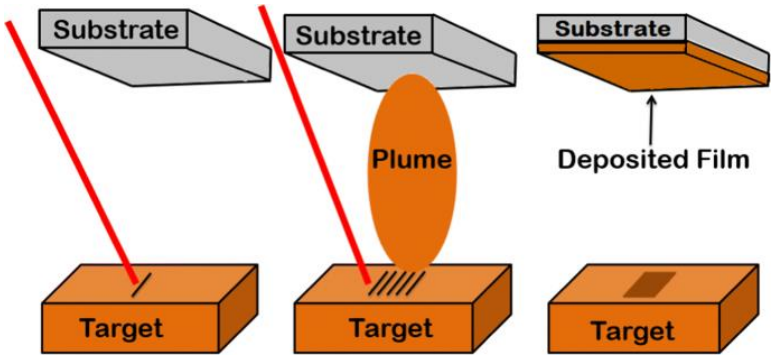

Figure 4.2.1: Schematic illustration of the steps that occurred in the ultra-high vacuum during a Pulsed Laser Deposition experiment

The first stage involves photon absorption at the target surface, in which the energy of the incident laser is converted into electronic excitations before being transformed into thermal, chemical, and mechanical energy. The second step consists of the target material vaporization and the plasma formation. Species in the heated area are ejected from the target during the multiphoton ionization of the gaseous phase, creating the characteristic plume. These ejected species continually absorb the incident laser light, resulting in a strong interaction between the plume and the incident laser beam as well as the reheating of the plume. This reheating process is prominent for excimer lasers exhibiting relatively long pulses lasting several tens of nanoseconds. Then, the third stage involves the plasma plume expansion in vacuum, after the laser pulse. The plume expansion is considered as adiabatic, because there is no mass or energy transfer to the ablation plume.

Finally, the ablation material's film growth is the final stage. The plasma plume's ion-electron recombination occurs, producing the material flux required for film formation. The material deposition on the substrate during ablation and material transfer by the plasma plume is nonuniform due to the plume's extremely forward directed character. Scanning the ablation beam across a rotating target may result in more uniform film coverage of the desired material over the substrate. Here, we have to be careful and observant because the chamber pressure has a significant impact on the thickness of the deposited film on the substrate. In the following figure (Figure 4.2.2) it presented an approximate time scale concerning the stages and the physical operations during a Pulsed Laser Deposition experiment that mention above.[30] , [35]

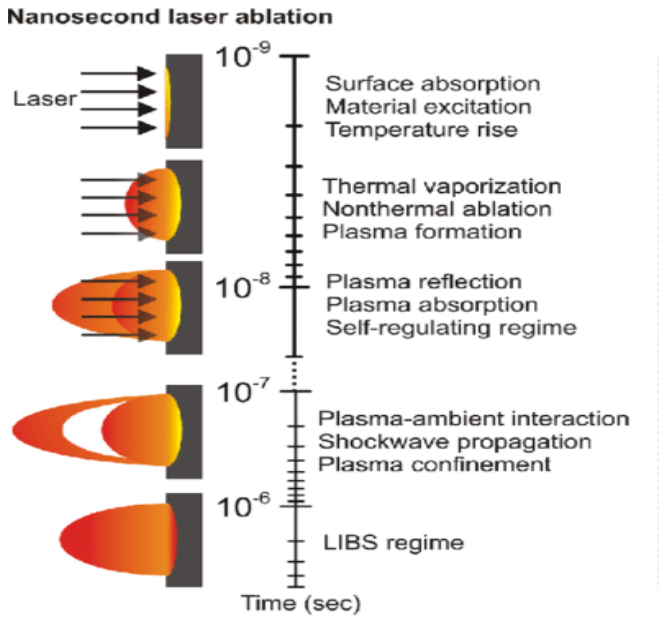

Figure 4.2.2: Approximate time scales during laser ablation using nanosecond lasers

Chapter 5: Photocatalysis and ZnO nanorods

5.1. Photocatalysis

Photocatalysis is a process in which light energy is used to drive pairs of chemical reactions. Through the absorption of light, an excited electron/hole is produced. Due to their activated state, the electron and hole perform chemical reduction and oxidation as though they were highly reactive reagents in a chemical reaction. In typical photocatalytic reactions, catalysts or substrates are activated by photons or light radiation, such as ultraviolet or visible light of suitable wavelengths, followed by electron- transfer processes to or from reactants performing coupled-redox reactions. There are two types of photocatalysis: i) Homogeneous photocatalysis and ii) Heterogenous photocatalysis. In homogeneous photocatalysis, reactants and the photocatalyst exist in the same phase while in the heterogenous photocatalysis reactants and the photocatalyst are in different phase.[36]

Most regularly used homogeneous photocatalysis processes involve the use of ozone, transition metal oxide, and photo-Fenton systems (Fe^{+} and Fe^{+} /H_2O_2), which have •OH as the reactive species that is used to reduce the reaction time. From the other hand, heterogeneous photocatalysis is more intensively studied due to its potential applications in different sectors. In heterogeneous photocatalysis, the reaction scheme implies the development of an interface between a strong metal photocatalyst and a liquid containing the reactants and products of the reaction. [36]
Photocatalysis has a plenty of advantages, which some of them are presented:

- Photocatalysis offers a good replacement for the energy-intensive conventional treatment methods (adsorption on activated carbon, ultrafiltration, reverse osmosis, coagulation by chemical agents, ion exchange on synthetic adsorbent resins) with the capacity for using renewable and pollution-free solar energy.
- Photocatalysis leads to the formation of harmless products, unlike conventional treatment measures which transfer pollutants from one phase to another.
- The photocatalytic process can be used in the destruction of a variety of hazardous compounds in different wastewater streams.
- The reaction conditions for photocatalysis are mild, the reaction time is modest and a lesser chemical input is required.
- Minimal of secondary waste generation
- It can be applied to hydrogen generation, gaseous phase, and aqueous treatments as well for solid (soil) phase treatments to some extent

Semiconducting materials (TiO_2, ZnO, SnO_2, and CeO_2) mainly act as heterogeneous photocatalysts, because of its favorable combination of electronic structures which is characterized by a filled valence band and an empty conduction band, light absorption properties, charge transport characteristics and excited states lifetime.[36], [37]An excellent semiconductor photocatalyst should be:

- able to utilize visible and/or near-UV light,
- biologically and chemically inert,
- photoactive,
- photostable (i.e., stability toward photo corrosion),
- inexpensive
- nontoxic

In this bachelor thesis, we have implied ZnO nanorods as photocatalysts in the fabricated three-dimensional periodic porous structures. At first the samples were deposited by a thin film of Zn via Pulsed Laser Deposition technique and then the ZnO nanorods were growth through a simple aqueous chemical growth that we will mention more about this technique in the experimental part of this thesis. In the following figure a typical photocatalysis mechanisms is presented.

Figure 5.1.1: Mechanism of photocatalysis of contaminants using ZnO photocatalyst in presence of UVA irradiation

5.2. ZnO nanorods

ZnO (Zinc Oxide) is considered to be a well-studied metal oxide semiconductor based on to its exceptional electrical, catalytic, optical and optoelectronic properties. Nowadays, ZnO believes to be suitable for a broad range of applications such as gas sensors, piezoelectric devices, UV light detectors, energy applications (batteries, solar cells, water splitting), photocatalytic and biological researches. Additionally, ZnO is an II-VI direct gap semiconductor with a wide bandgap (3,37 eV) at room temperature and large exciton binding energy (60meV). Not to mention the fact that ZnO has a plethora of growth geometries like nanorods, nano-wires, nanobelts etc. Another characteristic of ZnO is that its crystal lattice density is $5.67\ g/cm^3$ while its melting point is 1975°C.

Finally, ZnO crystallizes in the wurtzite structure, which is a hexagonal unit cell with lattice parameters “α” and “c” in the ratio of $\frac{c}{a} = \sqrt{\frac{8}{3}} = 1.633$. In wurtzite structure each zinc atom is surrounded by four oxygen atoms, which are located at the corners of a nearly regular tetrahedron. Due to its structure, this material presents a strong piezoelectric effect as there is conversion from mechanical energy into electrical energy. [38] [39] [40] [41] [42]. In the following figure the Cell wurtzite structure of ZnO is presented. (Figure 5.2.1)

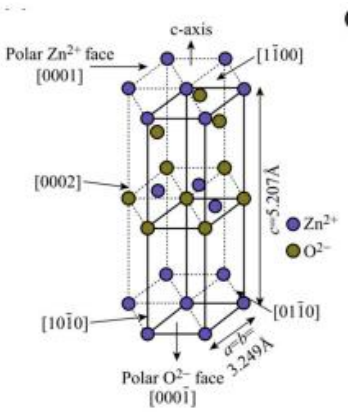

Figure 5.2.1: Cell wurtzite structure of ZnO

PART II – EXPERIMENTAL PART

Chapter 6: Experimental generation of Multi-beam Interference patterns

6.1. Introduction

Multiple-beams interference experimental research was mainly focused on studying two, three, four and five beam interference patterns. For this purpose, an imaging set-up was firstly used to easily observe if the experimental patterns were identical with the theoretically expected motifs. For the phase masks, we use the following computer-generated holographic approach: light emitted by a set of N point sources interferes with a reference plane wave that propagates along the z axis. This interference, assuming linearly polarized light, can be described at the plane of the SLM as:

$$E_S(r,t) = E_O\, e^{i(kz-\omega t)}\hat{x} + \sum_{i=1}^{N} E_i\,(r_i - r_0, t)$$

where r_0 is the position of the SLM screen, ri is the position of each point source, $E_i(r,t) = E_i e^{i(k|r|-\omega t+\varphi_i)}$, $\hat{x}$ is a spherical wave of amplitude Ei emitted from point source with index i, k is the wavenumber, and φi is a constant bias phase for every point source. Through a special designed code, we could be able to modify the number of the beams, the distance between them, the phase of this interfering beams and the point of reproduction after the initial beam pass through SLM and SLM gather the selected information's. Also, the designed phase masks should be an 8-bit grayscale image. In this way, each gray level is directly associated with a discrete increment of the phase from 0 (black) to 2π (white), and a linear relation for the intermediate values. Therefore, 2π/256 phase increments can be encoded at each pixel on the LC display by displaying an 8-bit (256) pixelated image ,which can easily be generated using a computer software the same that we write the code for the phase masks (Image J software). [2],[18], [20].

6.2. Experimental Set-up

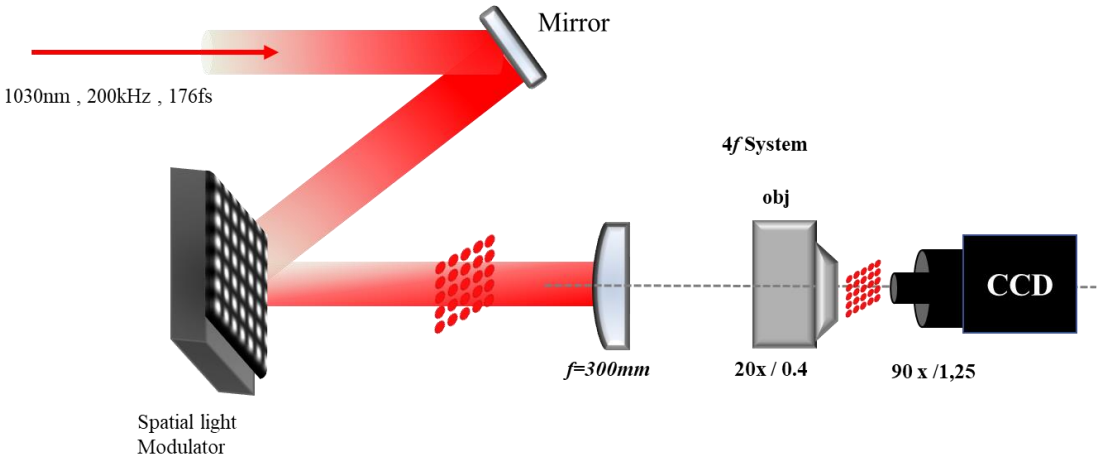

Figure 6.2.1: Schematic illustration of the experimental imaging set-up

The experimental setup is depicted in Fig. 6.2.1. The phase of a Gaussian beam is spatially modulated using an appropriate, as described above, phase mask applied on a Hamamatsu LCOS-X10468-2 phase-only reflecting SLM, generating the properly designed multiple-beam interference pattern at a specific distance. A PHAROS light conversion femtosecond laser system (1030 nm, 167 fs, 200kHz) is used as a light source. In order to adapt to the MPP application, the holographically generated 3D light distribution is further reduced in size by MD32 times in the xy plane (M2 times in the longitudinal axis), using a 4f optical system composed by a 300 mm lens, a 20 x(NAD0.4) microscope objective and a 90x (NAD 1.25). The experimentally generated interference pattern is visualized using a compact microscope imaging system coupled with a linear 14-bit charge-coupled device (CCD) camera.

6.3. Imaging Results

6.3.1. Two beams

The first interference case that has been studied was two-beams interference pattern by modifying the distance between the occurred interfering beams. Three different cases were studied. In the following figures the phase masks (left) of two beams (up left) and the corresponding interference pattern (down left) by the designed code are presented. and the visualization for each one of these during the three different distance modulation processes as captured from the CCD camera.

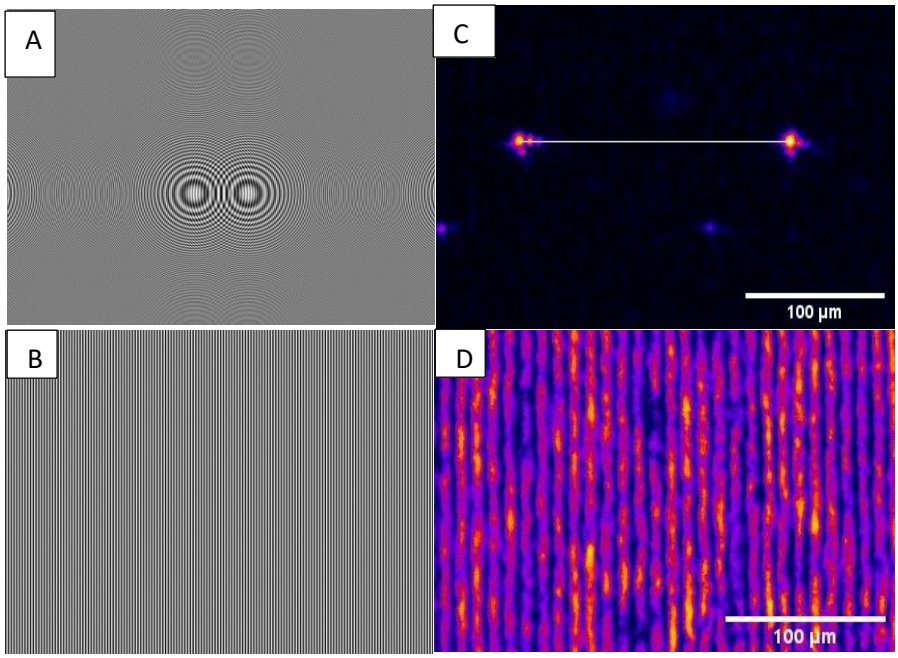

Figure 6.3.1.1: A) Code-generated phase mask, B) code-generated interference pattern C) visualization phase mask and D) visualization interference pattern at distance 190.60 µm.

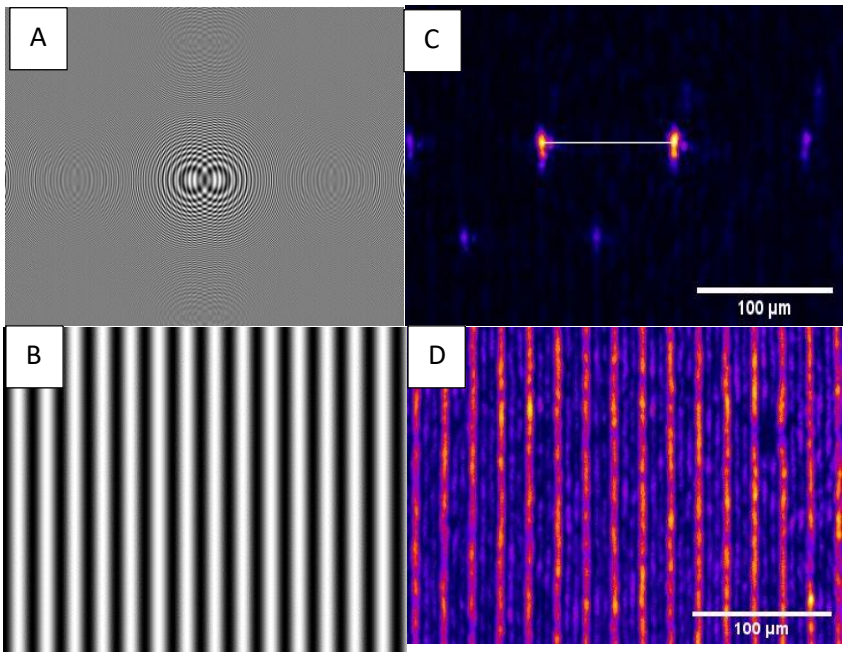

Figure 6.3.1.2: A) Code-generated phase mask, B) code-generated interference pattern C) visualization phase mask and D) visualization interference pattern at distance 97.30 µm.

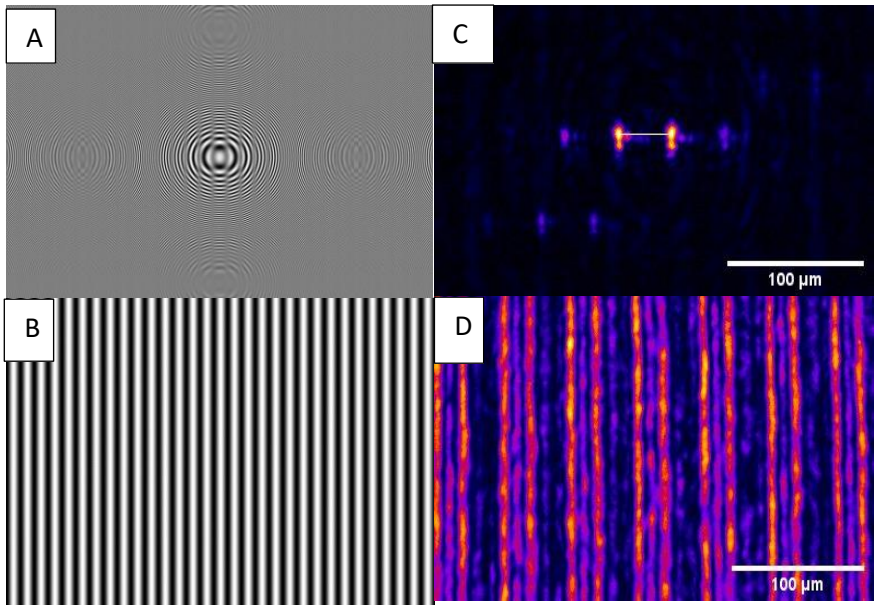

Figure 6.3.1.3: A) Code-generated phase mask, B) code-generated interference pattern C) visualization phase mask and D) visualization interference pattern at distance 38.8 μm.

For all the three different distance cases one can observe that the resultant interference patterns have the same geometry with the initial theoretical pattern that has been demonstrated in the theoretical part of this thesis. (Figure 3.2.1.1). As concern the periodicity of these interference pattern it can be calculated since the distance between the beams is known. So, for a chosen distance of 38.8 μm a fringe-like pattern of periodicity 50.73 μm and width 24.0 μm is produced. When the same beams are placed in distance 97.3 μm the fringe-like pattern gains a periodicity of 19.28 μm and width 4.28 μm. The distance is, then, altered in almost twice the previous distance (190.60 μm) resulting in a fringe-like pattern where the fringes are barely distinct.

After the alternation of the distance between the two beams, the next step was to investigate what will happen when we modulate the phase (φ) for one of the interfering beams (pointed beam) at a specific distance. The chosen distance was equal to 38.8 μm for two beams of diameter 7.0 μm while the visualized phases are $\varphi=\pi/6$ rad, $\varphi=\pi/4$ rad, $\varphi=\pi/3$ rad, $\varphi=\pi/2$ rad, $\varphi=2\pi/3$ rad, $\varphi=3\pi/4$ rad, $\varphi=5\pi/6$ rad. In the following figure (6.3.1.4) the phase masks and the interference patterns of three significant phases are only presented. ($\varphi=0$ rad, $\varphi=\pi/2$ rad, $\varphi=\pi$ rad)

	Phase mask	Interference pattern	Visual phase mask	Visual interference pattern
a	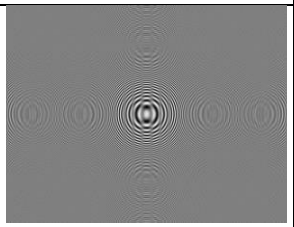	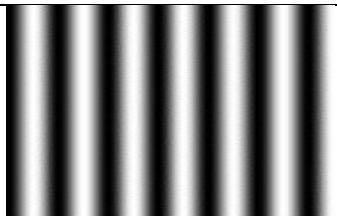	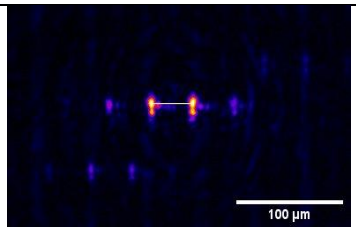	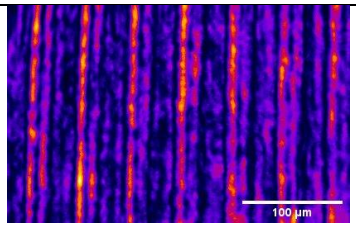
b	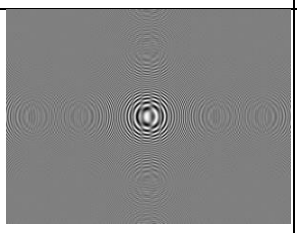	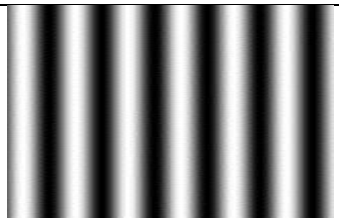	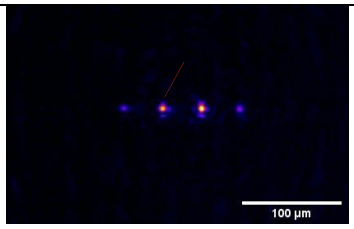	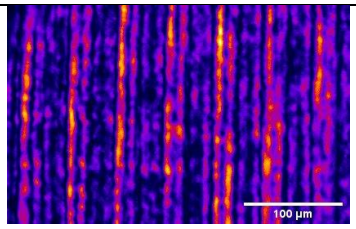
c	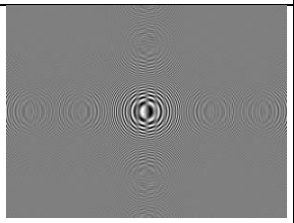	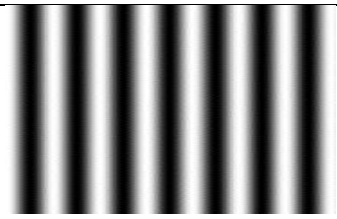	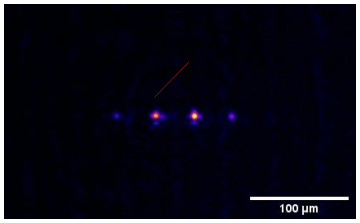	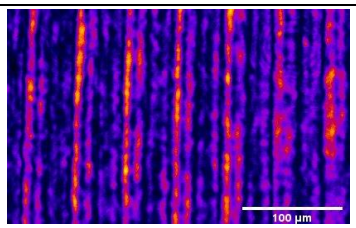

Figure 6.3.1.4: Phase mask, interference pattern and visualization result for two interfering beams at distance 38.6 μm with a) no phase modulation b) phase φ=π/2 c) phase φ=π rad applied on the left beam.

Based on the upper results we can assume that altering the phase of the beam the overall symmetry remains stable without changes in periodicity or the width of the pattern but through phase modulation the fringes tend to transfer since the bright fringes take the place of the dark fringes and correspondingly the dark fringes to bright fringes. In the follow diagram it can be discerned the differences in the spot we modulate. More specifically there are presented the initial phase, the pi/2 phase and the pi phase.

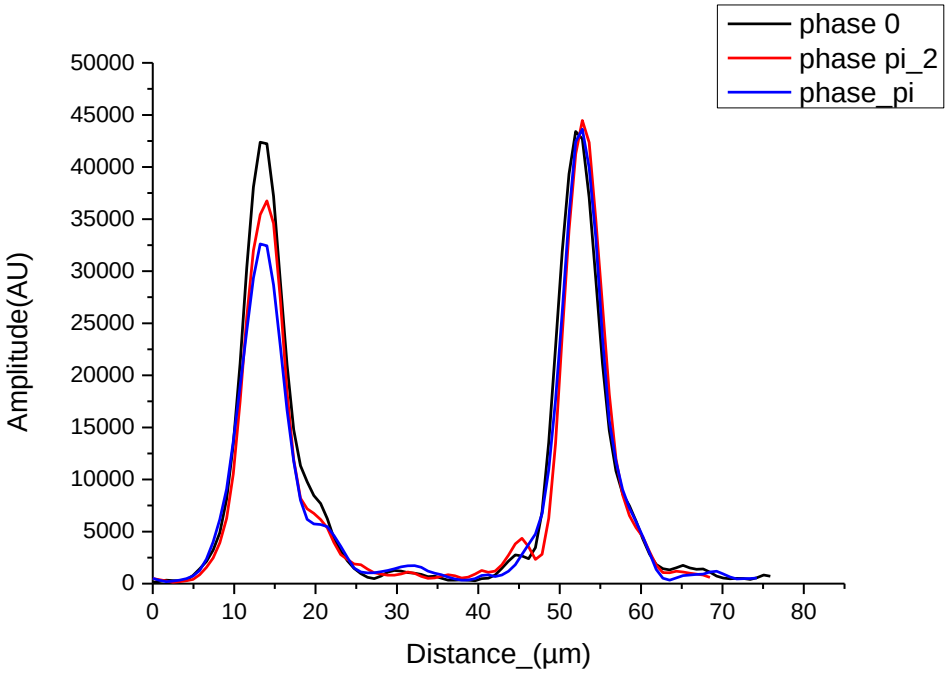

Figure 6.3.1.5: Experimental intensity (amplitude) over distance distributions (normalized curves) of the phase modulated and non- modulated beam in phase, for φ=π/2 rad and φ=π rad

6.3.2 Three beams

In this part of this thesis, we studied the behavior of the three-beams interference when we adjust the distance of the beams without any other modulation. In the following pictures there is the presentation of the phase masks, the expected interference patterns given by the designed code and the visualization for each one of these during the three different distance modulation processes as captured from the CCD camera. The behavior of this interference case was identical with the case of two beam interference, meaning that as the distance between these three beams of diameter 9.5 µm increases the periodicity of the spots tend to decrease.

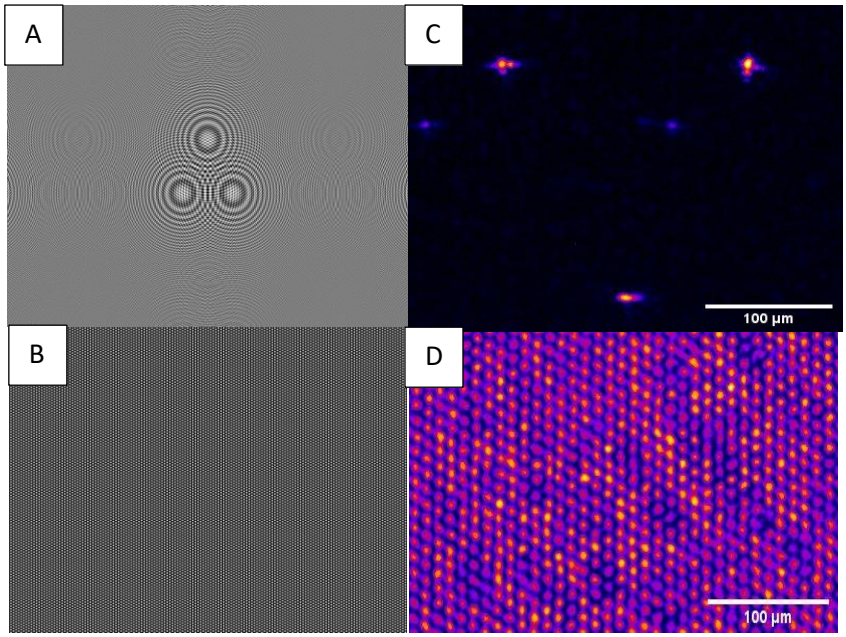

Figure 6.3.2.1: A) Code-generated phase mask, B) code-generated interference pattern C) visualization phase mask and D) visualization interference pattern at distance 193 µm (upper beams) and 218 µm (upper beams and lower one).

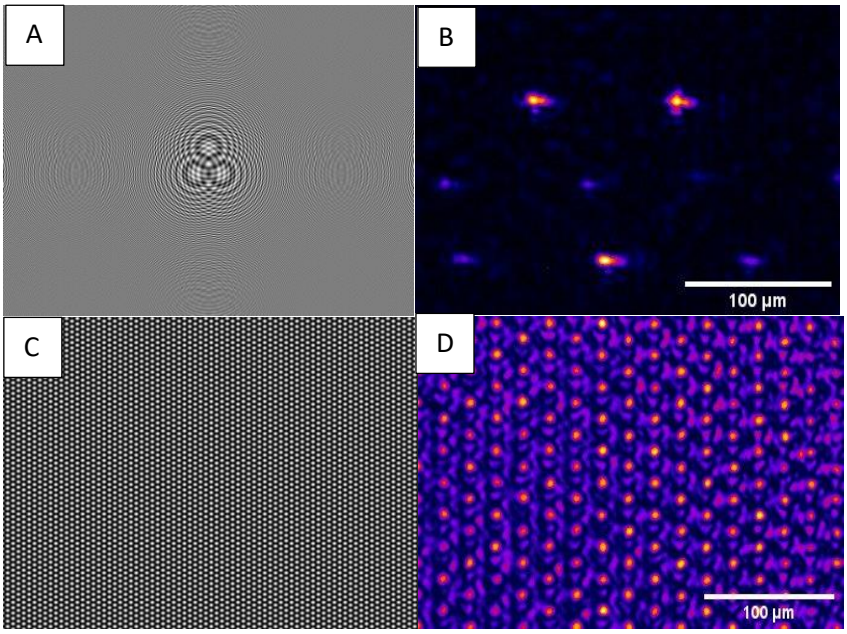

Figure 6.3.2.2: A) Code-generated phase mask, B) code-generated interference pattern C) visualization phase mask and D) visualization interference pattern at distance 98 µm (upper beams) and 110 µm (upper beams and lower one)

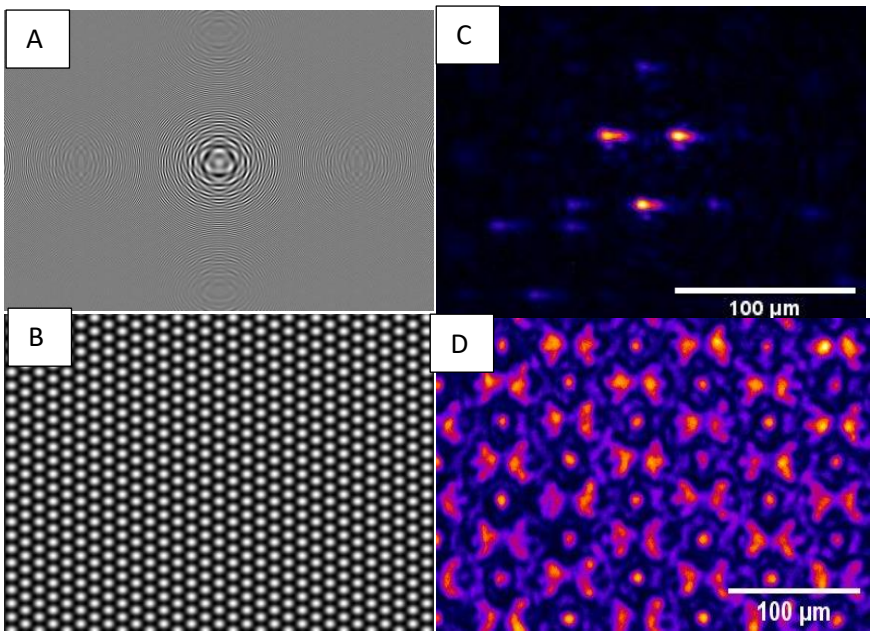

Figure 6.3.2.3: A) Code-generated phase mask, B) code-generated interference pattern C) visualization phase mask and D) visualization interference pattern at distance 40.0 µm (upper beams) and 29.0 µm (upper beams and lower one)

Just like for the two-beams interference pattern after the modulation of distance between the interfering beams we altered one of the three beams phase in order to study if it would create a different behavior in the interference patters. For this particular study we modified the upper beams (pointed beam). The distance was chosen to be equal to 40.0 µm between the lower beams and 29.0 µm between the lower beams and the upper one, while the phases that have been chosen were $\varphi=\pi/6$ rad, $\varphi=\pi/4$ rad, $\varphi=\pi/3$ rad, $\varphi=\pi/2$ rad, $\varphi=2\pi/3$ rad, $\varphi=3\pi/4$ rad, $\varphi=5\pi/6$ rad similar to the two-beams interference study. In the following figure (6.3.2.4) the phase masks and the interference patterns of three significant phases are only presented. ($\varphi=0$ rad, $\varphi=\pi/2$ rad, $\varphi=\pi$ rad)

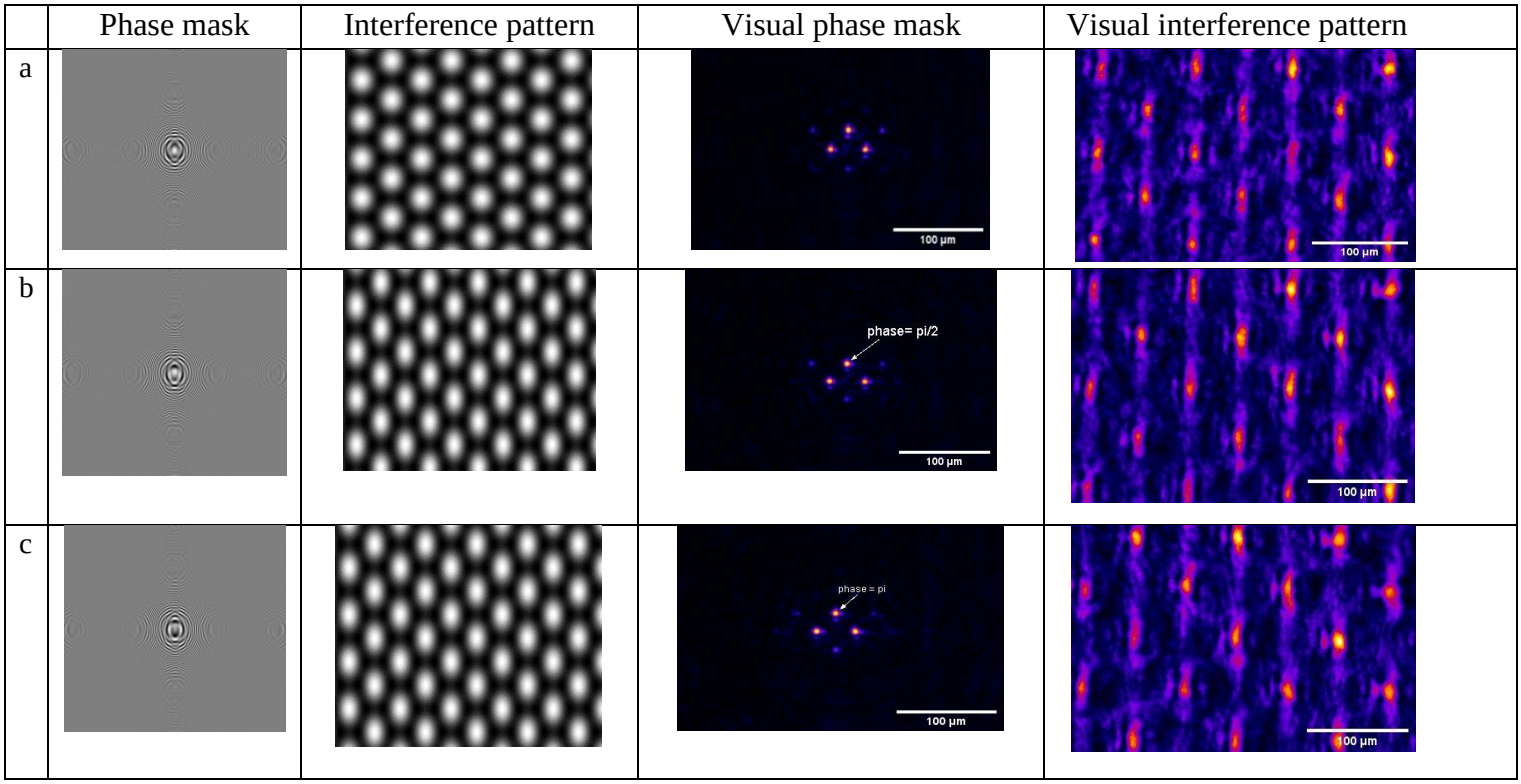

Figure 6.3.2.4: Phase mask, interference pattern and visualization results for three-beams interference for a) no phase modulation b) phase φ=π/2 rad c) phase φ=π rad applied on the upper beam.

As shown in the figure (6.3.2.4), the pattern's symmetry stays constant when the phase of the beam is changed and there are no changes in the pattern's periodicity or diameter. The stretched points, which are also apparent in the interference pattern, are the most distinguishing feature. As a result, the spots have a periodicity of 70.0 μm, and their diameter has been calculated to be 9.0 μm. Nevertheless, the overall pattern is carried downwards. Observing the interference patterns with a closer look someone will be able to see the movement of each point from no phase modulation to phase φ=π rad. As it was mention earlier, along z axis the periodicity and the diameter of the spots remain intact. Based on that, we analyzed the produced interference patterns at depth 0-60 μm with step 20 μm for no phase modulation and phase φ=π/2 rad. From that we managed to observe that in higher depths the stretched points become round and tend to gain a square lattice symmetry.

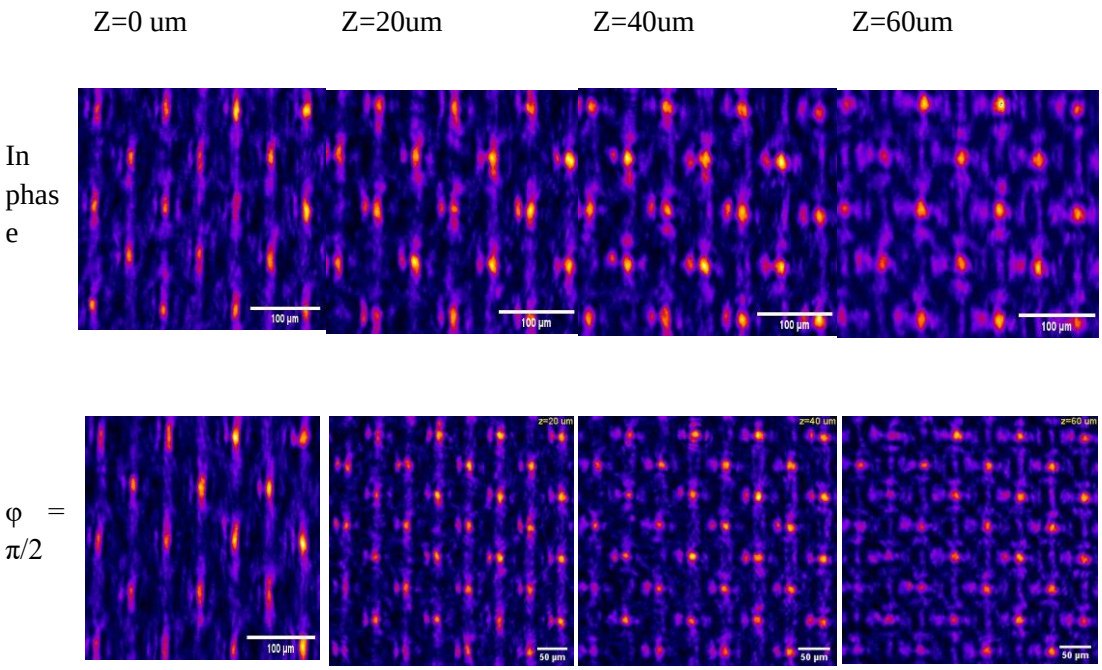

Figure 6.3.2.5: Comparison of the patterns that are produced at depth 0 to 60 μm from non-phase modulated three-beams interference and three-beams interference when phase φ=π/2 rad is applied in one of the three beams.

6.3.3 Four beams

In the scenario of four-beams interference we follow the same procedure as the previous studies. Firstly, we modulate the distance between the interfering beams and then we alter the phase not only of one but also of two of the four interfering beams with the cause of studying any potential changes. The spots-like square lattice symmetry that mentioned in the theoretical part of this thesis was actually produced by the imaging system and the distance alteration affects the periodicity of the patterns. As soon as we increased the distance between the interfering beams the periodicity of the spots tend to decrease something that is visible when someone observe the following figures. The placement of the beams at distance 38.0 μm gives a spots-like pattern of periodicity 52.4 μm and diameter 11.0 μm and when the same beams are placed in distance 95.0 μm the periodicity is equal to 20.0 μm with a diameter of 8.0 μm. Increasing even more the distance of the interfering beams (190.0 μm) in our case the spots are barely distinct Once again, the visualized phases are φ=π/6 rad, φ=π/4 rad, φ=π/3 rad, φ=π/2 rad, φ=2π/3 rad, φ=3π/4 rad, φ=5π/6 rad.

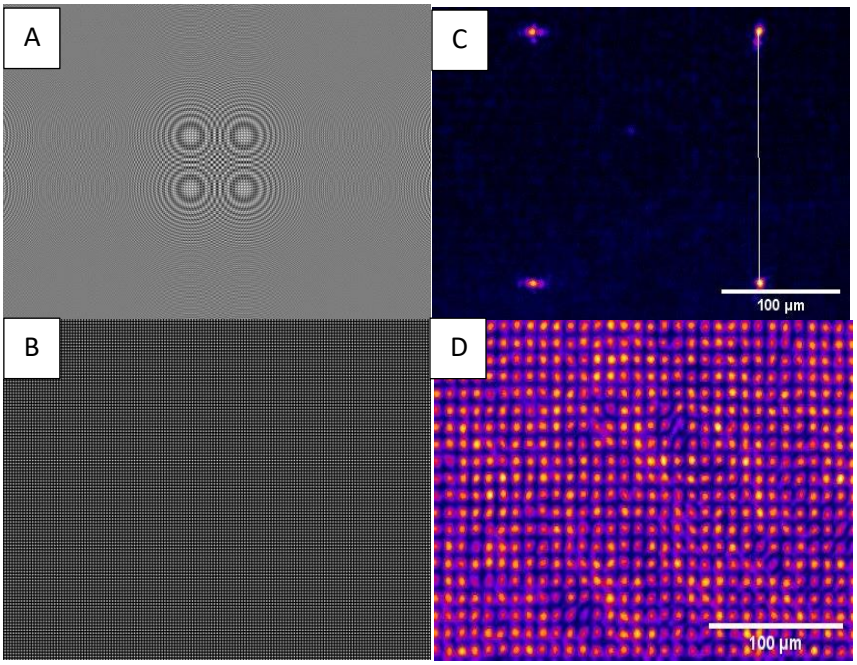

Figure 6.3.3.1: A) Code-generated phase mask, B) code-generated interference pattern C) visualization phase mask and D) visualization interference pattern at distance 190 µm.

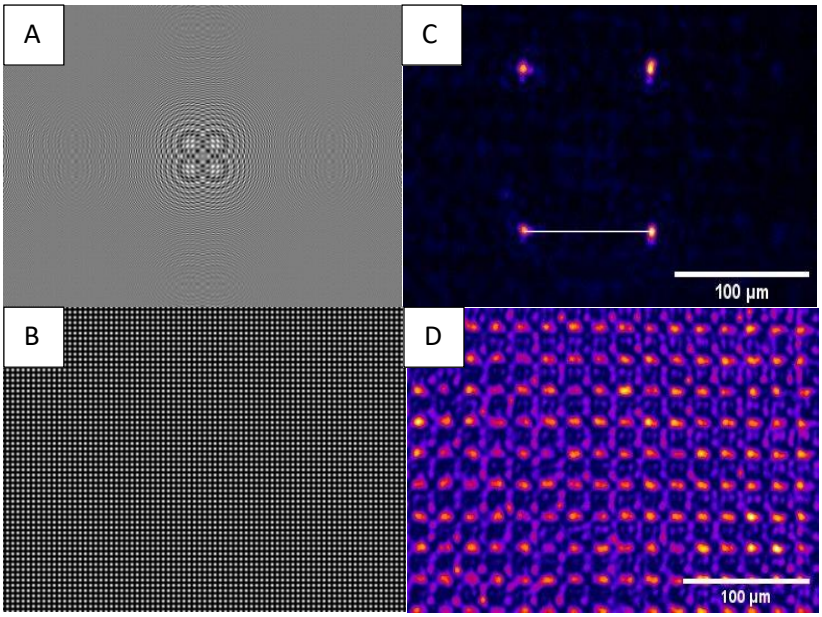

Figure 6.3.3.2: A) Code-generated phase mask, B) code-generated interference pattern C) visualization phase mask and D) visualization interference pattern at distance 95 µm.

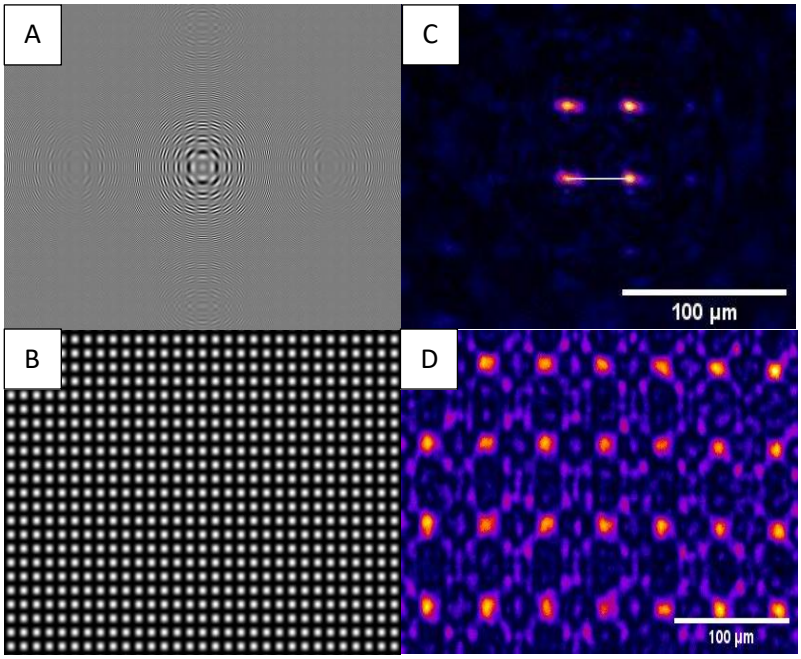

Figure 6.3.3.3: A) Code-generated phase mask, B) code-generated interference pattern C) visualization phase mask and D) visualization interference pattern at distance 38 µm.

After the analysis of the distance modulation as we mentioned we adjust the phase of one of the four interfering beams. Once again, the chosen phases remain the same ($\varphi=\pi/6$ rad, $\varphi=\pi/4$ rad, $\varphi=\pi/3$ rad, $\varphi=\pi/2$ rad, $\varphi=2\pi/3$ rad, $\varphi=3\pi/4$ rad, $\varphi=5\pi/6$ rad) and the chosen distance was 38.0 μm between all of the four beams. As someone can observe as we got through to the $\varphi= \pi/2$ the interference pattern started to change its symmetry. From spot-like symmetry tend to became a combination of spots and parallel fringes and that gave us the conclusion that changing the phase of one of the four interfering beams considers as a well-efficiency technique.

	Phase mask	Interference pattern	Visual phase mask	Visual interference pattern
a	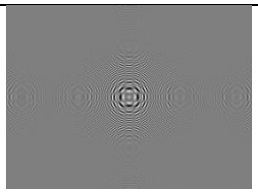	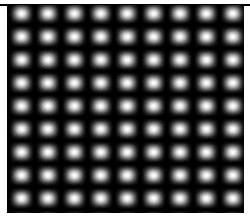	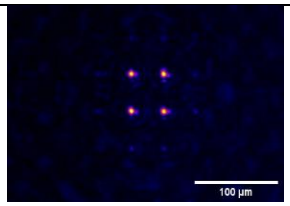	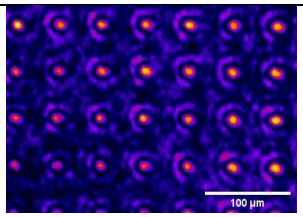
b	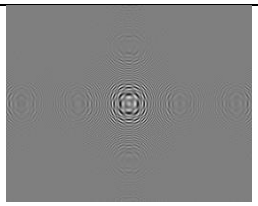	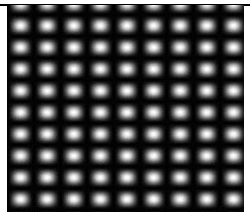	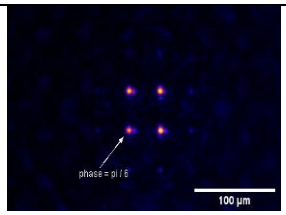	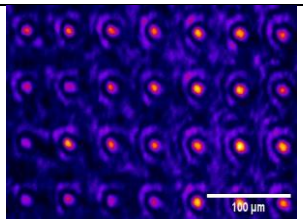
c	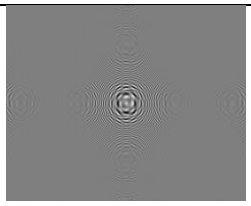	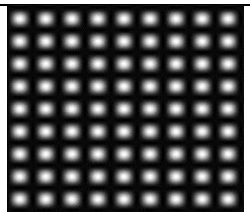	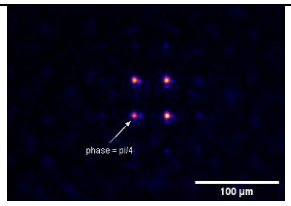	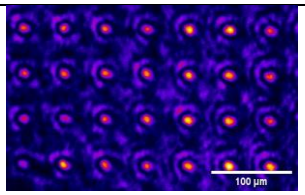
d	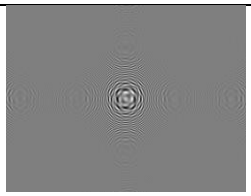		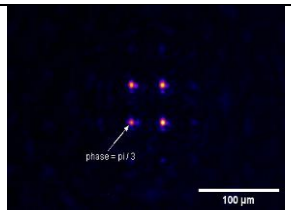	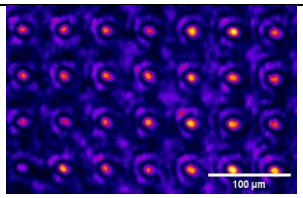
e	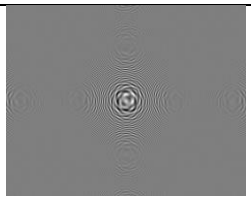		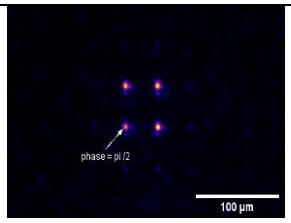	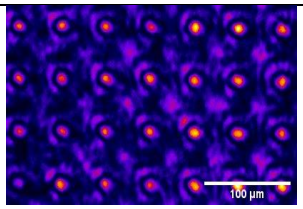
f	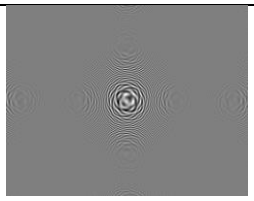		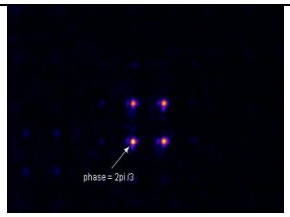	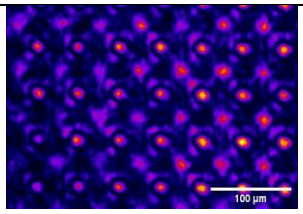

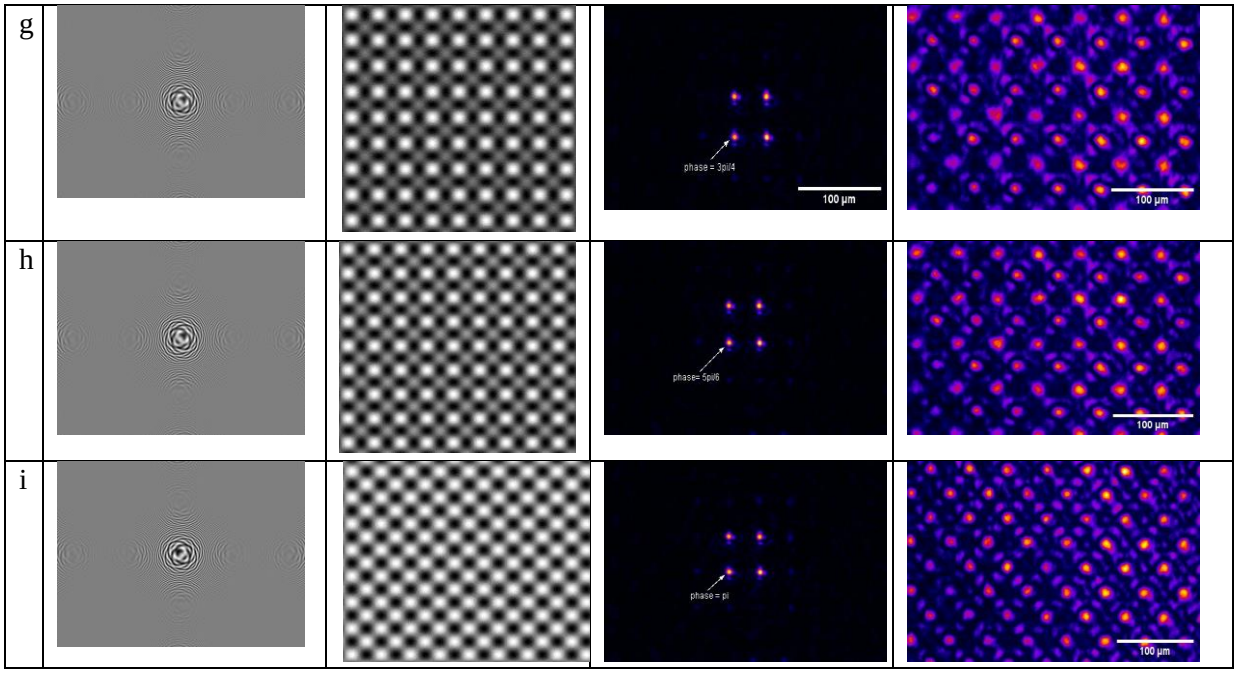

Figure 6.3.3.4: Phase mask, interference pattern and their visualization results for four interfering beams at distances 40 μm with a) no phase modulation b) phase φ=π/6 rad c) phase φ=π/4 rad d) phase φ=π/3 rad e) phase φ=π/2 rad f) phase φ=2π/3 rad g) phase φ=3π/4 rad h) phase φ=5π/6 rad i) phase φ=π rad applied on the lower left beam.

As it was stated earlier, it is worth noting that, as described before, interference does not affect only x-y plane but the z axis, too. Based on that, we analyze the produced interference patterns at depth 0-60 μm with step 20 μm for no phase modulation and phase φ=π/2 rad too as we did previous for different interferences. After a clear comparison between the two different phases but is same depth position it was showed that there indeed have some small differences but in z=60 μm the difference became more noticeable.

	Z=0 μm	Z=20 μm	Z=40 μm	Z=60 μm
In phase	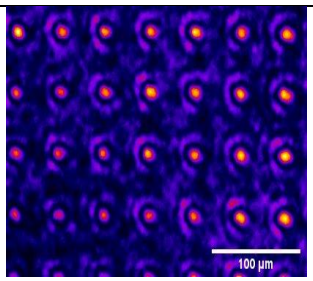	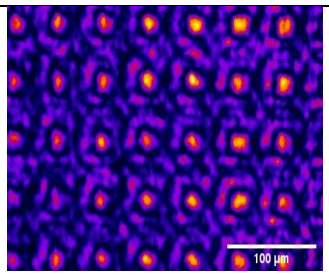	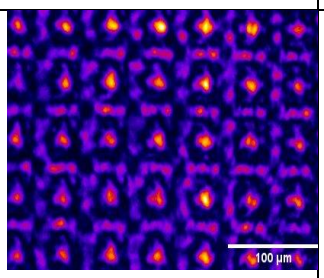	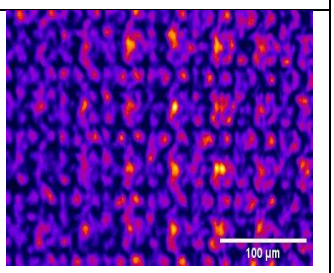
Φ = π/2	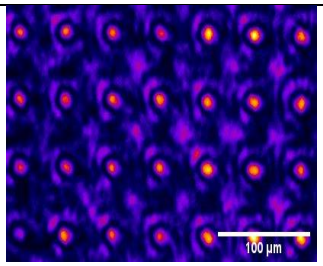	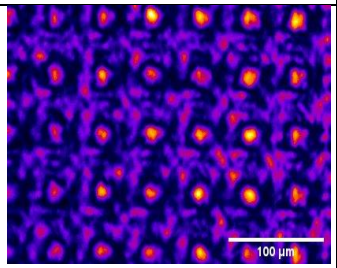	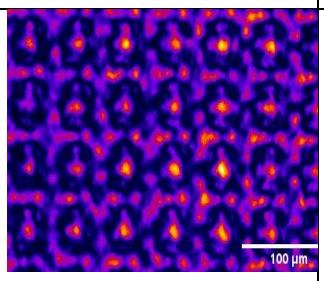	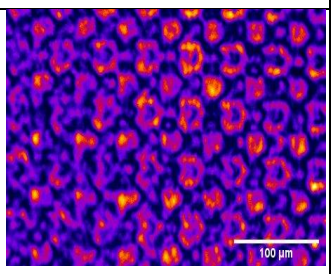

Figure 6.3.3.5: Comparison of the patterns that are produced at depth 0 to 60 μm from non-phase modulated multi-beam interference lithography and multibeam interference lithography when phase φ=π/2 rad is applied in one beam at four beam interference.

After the phase modulation of one of the four beams, we alter in this occasion two of the four beams with the cause of observe if this modulation will lead to a different interference pattern. So, this modulation was applied in the two lower beams. The distance and the diameter of the interfering beams are the same as in the previous case of phase modulation, (distance= 40.0 μm) and (diameter 5.3 μm) respectively. Despite the fact that phase modulation occurs in two beams simultaneously, the total square lattice symmetry, the periodicity (equal to 50.0 μm) and the diameter of the spots (equal to 10.0 μm) remain independent of the applied phase. The real effect of the phase modulation in the produced motifs was that it forced each spot to be transferred upwards, altering its position. The phases been used were the same as the previous study (φ=π/6 rad, φ=π/4 rad, φ=π/3 rad, φ=π/2 rad, φ=2π/3 rad, φ=3π/4 rad, φ=5π/6 rad).

	Phase mask	Interference pattern	Visual phase mask	Visual interference pattern
a	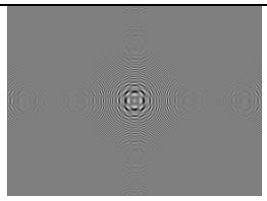	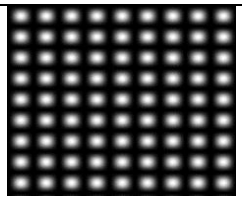	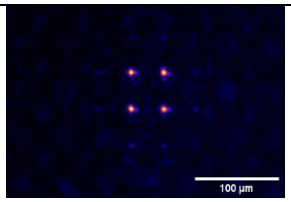	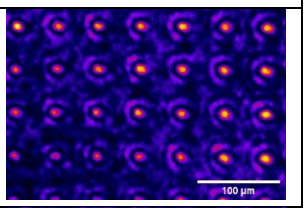
b	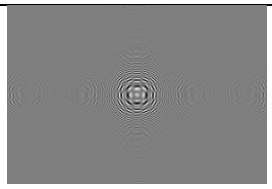	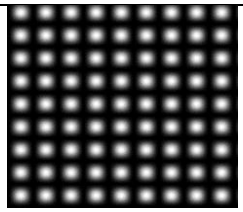	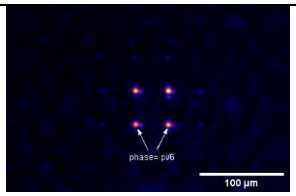	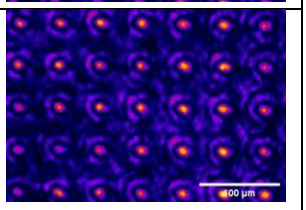
c	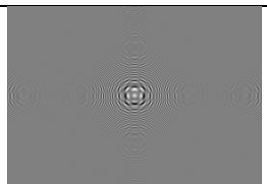	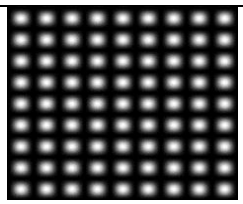	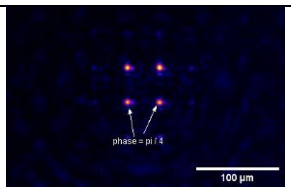	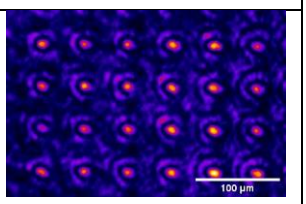
d	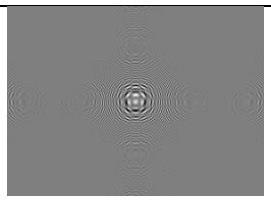	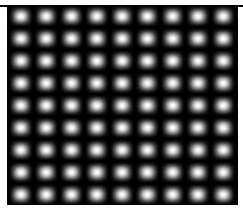	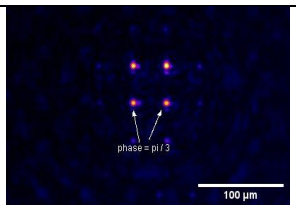	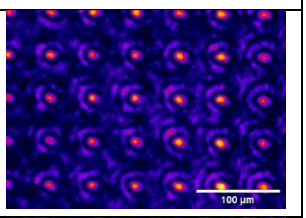
e	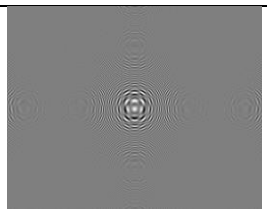	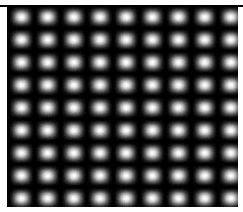	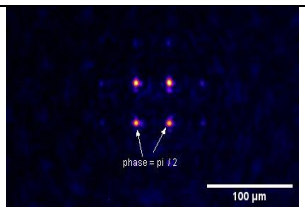	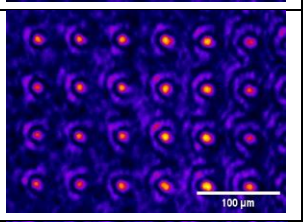
f	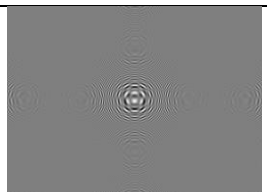	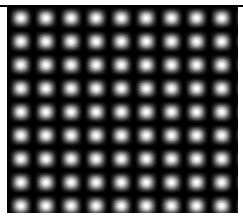	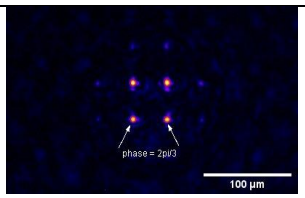	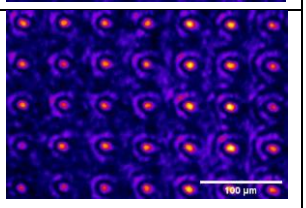
g	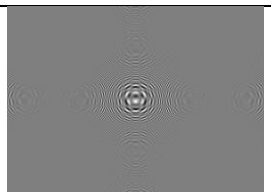	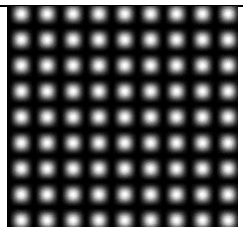	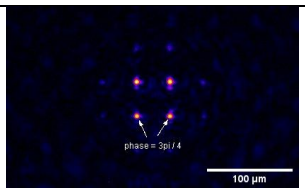	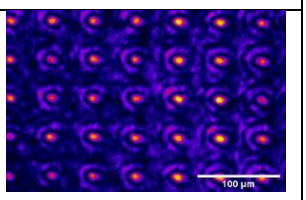
h	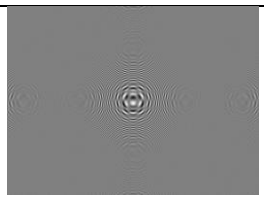	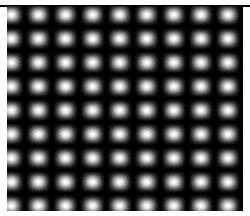	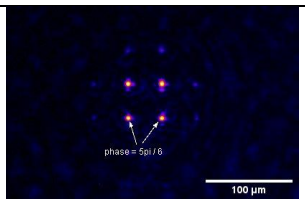	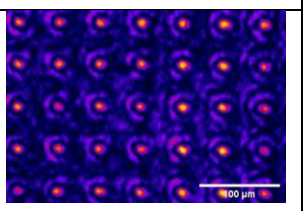

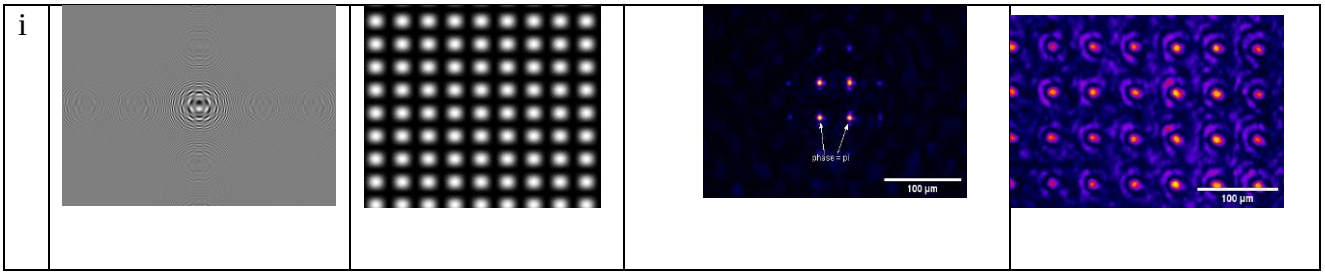

Figure 6.3.3.6: Phase mask, interference pattern and their visualization results for four interfering beams at distances 40 µm with a) no phase modulation b) phase φ=π/6 rad c) phase φ=π/4 rad d) phase φ=π/3 rad e) phase φ=π/2 rad f) phase φ=2π/3 rad g) phase φ=3π/4 rad h) phase φ=5π/6 rad i) phase φ=π rad applied on the two lower beams.

The final part of the experimental study of the four-beam interference was to try to see if we are capable of modulate the phase of each interfering beam but with different phase at each point. For this part, the phases that had been used were phases 0, phase φ=π/2 rad, phase φ= π/4 rad and phase φ=π rad.

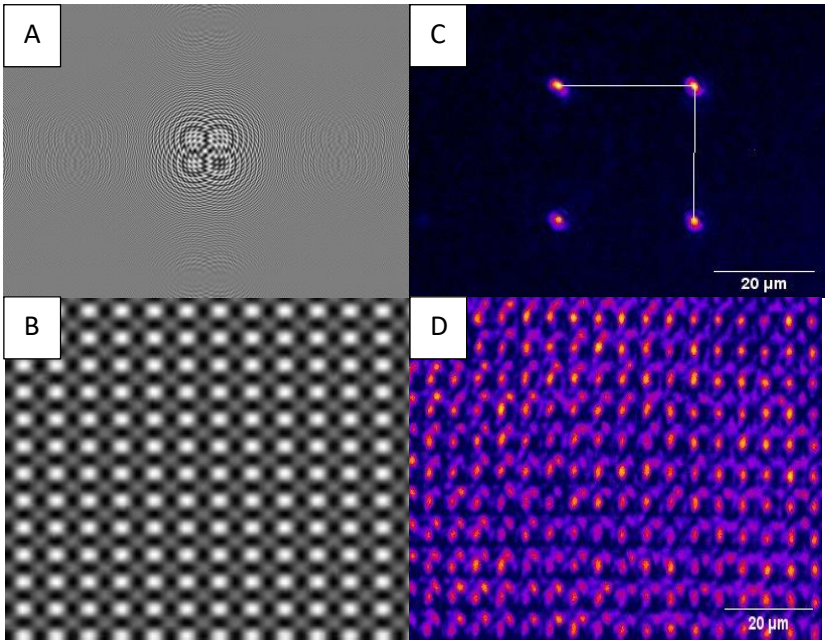

Figure 6.3.3.7: A) Code-generated phase mask, B) code-generated interference pattern C) visualization phase mask and D) visualization interference pattern at distance 26.85 µm and diameter 1.40 µm.

In the follow diagram it can be discerned the differences in the spots we modulate. As it may see there is a transient energy drop when we fetch up in pi-phase.

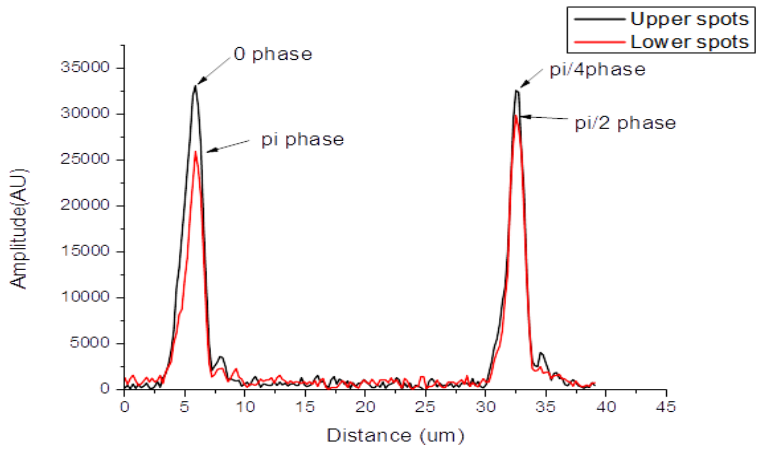

Figure 6.3.3.8: Diagram of the energy of the four interfering beams shown the phase modulation difference.

6.3.4 Five beams

Finally, the last part of this experimental results was to study any changes by alternating the distance of the five interfering beams. We modulate the phase for one, two and three of the five interfering beams with the cause of studying any potential changes among the non-phased interference pattern and between the different modulated occasions.

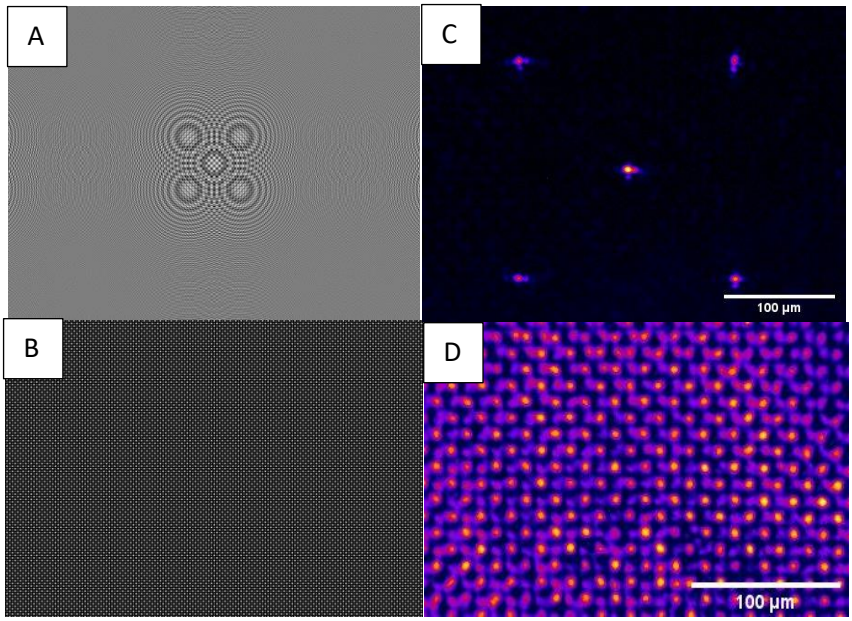

Figure 6.3.4.1: A) Code-generated phase mask, B) code-generated interference pattern C) visualization phase mask and D) visualization interference pattern at distance 138 µm.

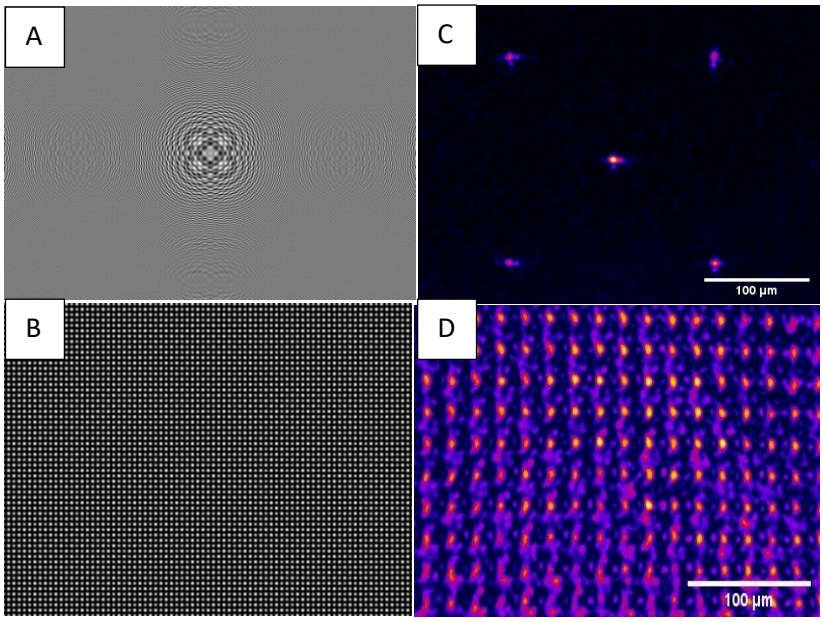

Figure 6.3.4.2: A) Code-generated phase mask, B) code-generated interference pattern C) visualization phase mask and D) visualization interference pattern at distance 69 µm.

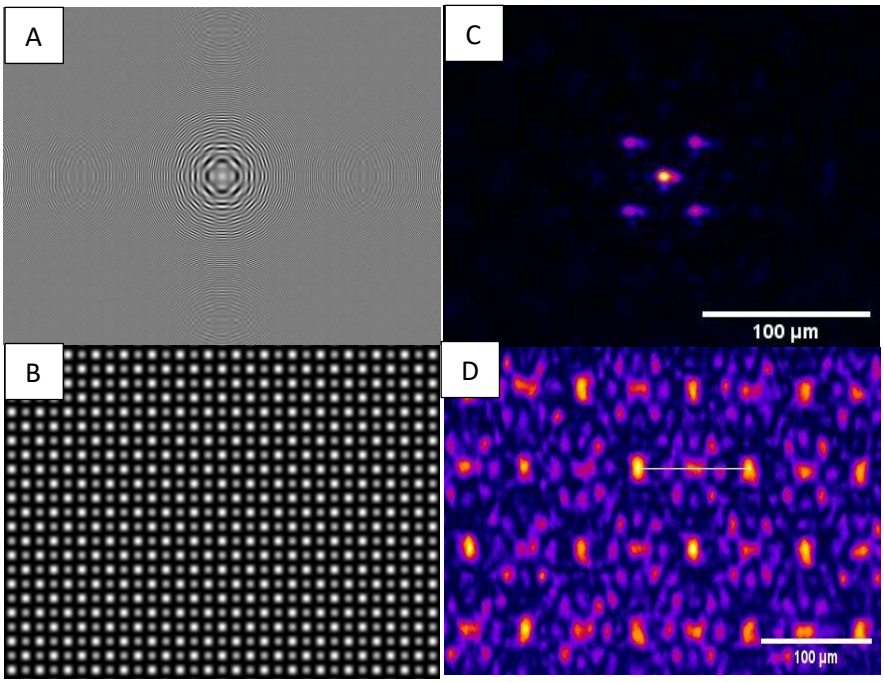

Figure 6.3.4.3: A) Code-generated phase mask, B) code-generated interference pattern C) visualization phase mask and D) visualization interference pattern at distance 28 µm.

The original geometry we created for the 5 beams was in the shape of a dice. In this scenario, the phase in the central point will be changed. The phases that this study occurred was φ=π/6 rad, φ=π/4 rad, φ=π/3 rad, φ=π/2 rad, φ=2π/3 rad, φ=3π/4 rad, φ=5π/6 rad, φ=π rad. In the following figure (6.3.4.4) the phase masks and the interference patterns of three significant phases are only presented. (φ=0 rad, φ=π/2 rad, φ=π rad)

	Phase mask	Interference pattern	Visual phase mask	Visual interference pattern
a	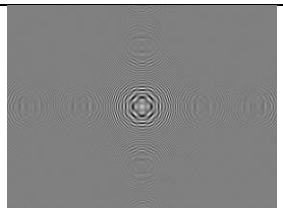	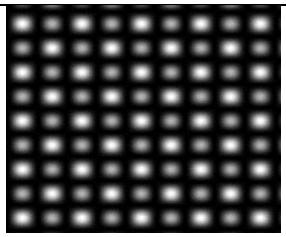	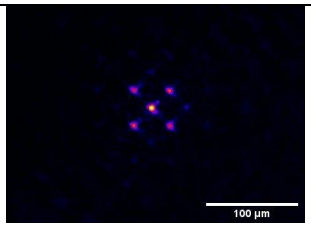	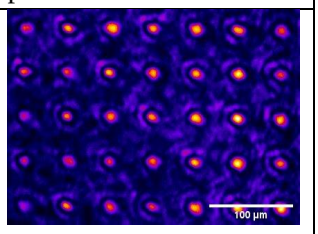
e	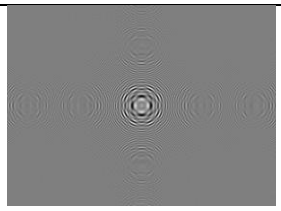	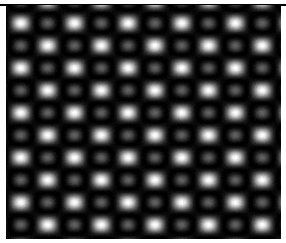	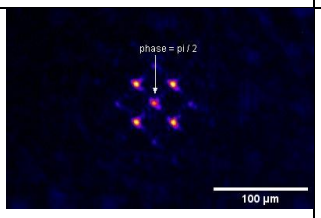	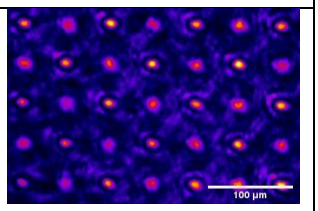
i	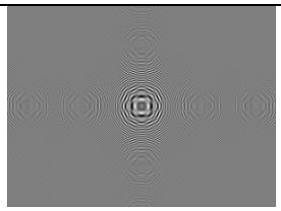	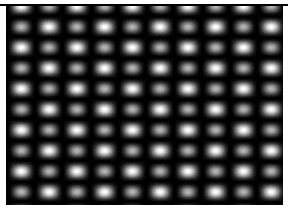	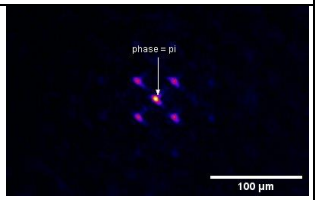	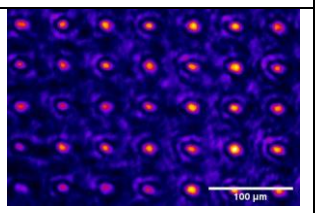

Figure 6.3.4.4: Phase mask, interference pattern and their visualization results for five interfering beams at distances 28 µm with a) no phase modulation b) phase φ=π/6 rad c) phase φ=π/4 rad d) phase φ=π/3 rad e) phase φ=π/2 rad f) phase φ=2π/3 rad g) phase φ=3π/4 rad h) phase φ=5π/6 rad i) phase φ=π rad applied in the central spot beam.

Then we modify the phase of one of the four symmetrical beams. The selected beam was the upper left (pointed beam) and concerning the phases were φ=π/6 rad, φ=π/4 rad, φ=π/3 rad, φ=π/2 rad, φ=2π/3 rad, φ=3π/4 rad, φ=5π/6 rad, φ=π rad. Once again, in the following figure (6.3.4.5) the phase masks and the interference patterns of three significant phases are only presented. (φ=0 rad, φ=π/2 rad, φ=π rad)

	Phase mask	Interference pattern	Visual phase mask	Visual interference pattern
a	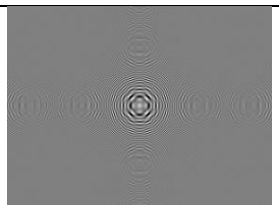	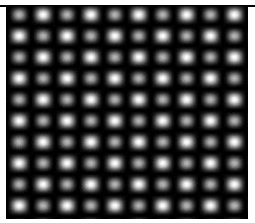	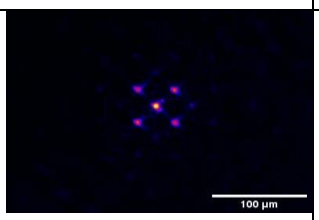	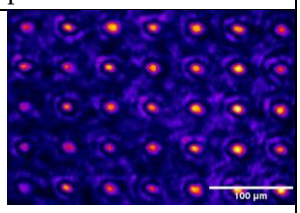
b	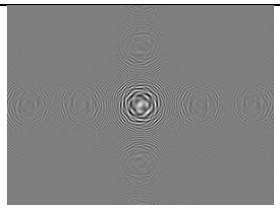	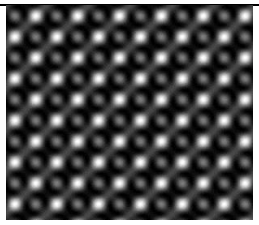	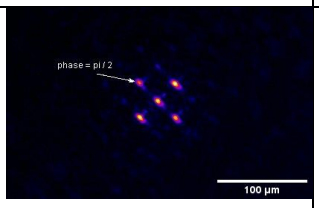	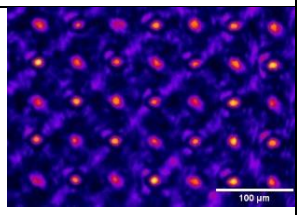
c	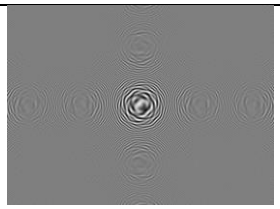	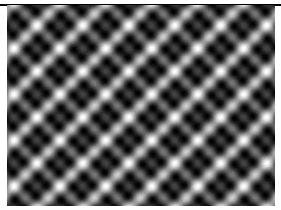	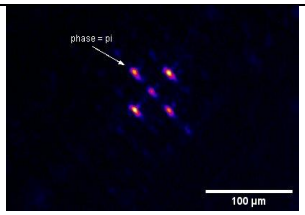	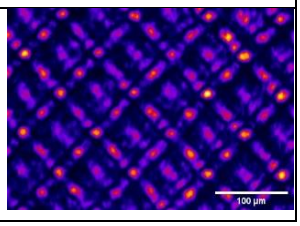

Figure 6.3.4.5: Phase mask, interference pattern and their visualization results for five interfering beams at distances 28 μm with a) no phase modulation b) phase φ=π/2 rad c) phase φ=π rad applied in the upper left beam.

The next study that we procced in the case of five-beams interference, is what happen when we alter the phase of two of the five interfering beams. The selected beams were the lower left (pointed beam) and the central point. Concerning the phases, φ=π/6 rad, φ=π/4 rad, φ=π/3 rad, φ=π/2 rad, φ=2π/3 rad, φ=3π/4 rad, φ=5π/6 rad, φ=π rad were used. Just like before, in the following figure (6.3.4.6) the phase masks and the interference patterns of three significant phases are only presented. (φ=0 rad, φ=π/2 rad, φ=π rad)

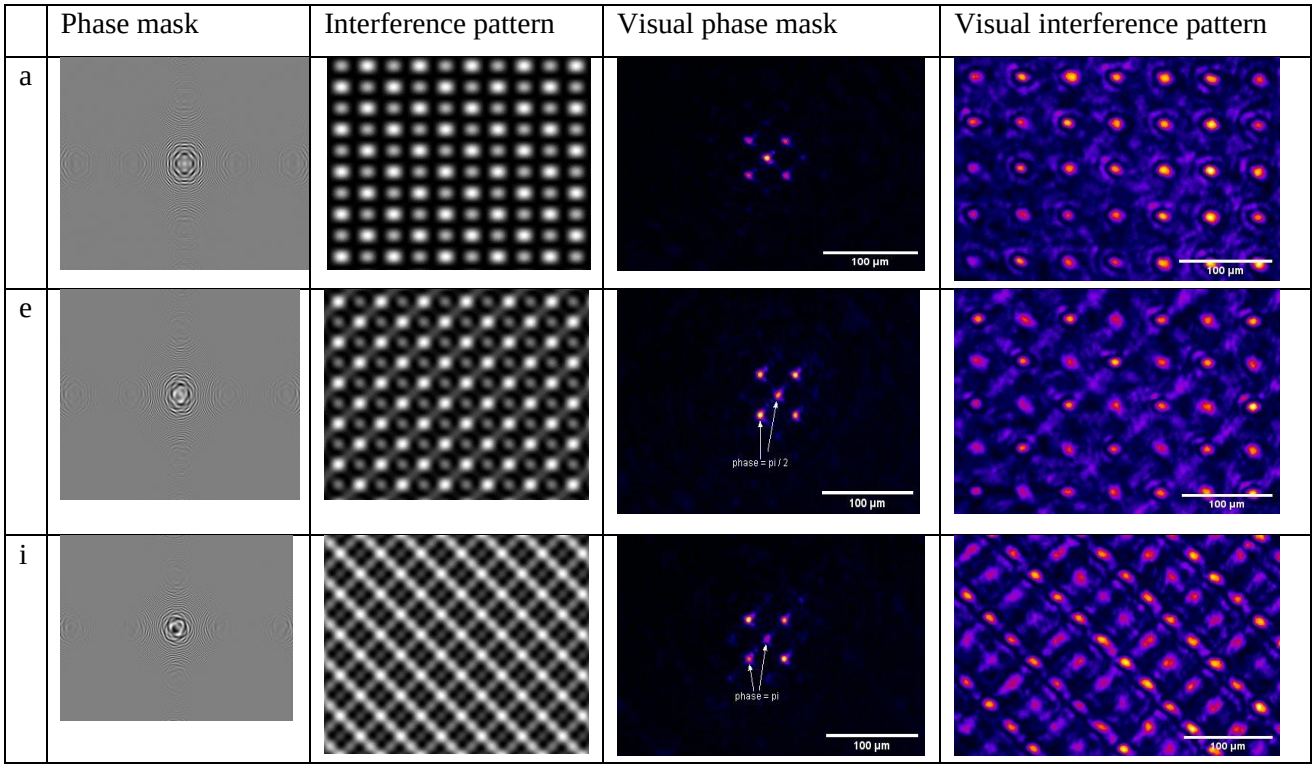

Figure 6.3.4.6: Phase mask, interference pattern and their visualization results for five interfering beams at distances 28.9 μm with a) no phase modulation b) phase φ=π/2 rad c) phase φ=π rad applied in the central and lower left beam.

Comparing the interference patterns that are produced along z axis for no phase modulation and phase φ=π/2 rad, we observed that complex interference patterns were created. In the next figures, the visualized results of the produced patterns at depth 0-60μm with step 20 μm are presented. At greater depth values the initial spot-like motifs with p4m symmetry are transformed into spots with random symmetry.

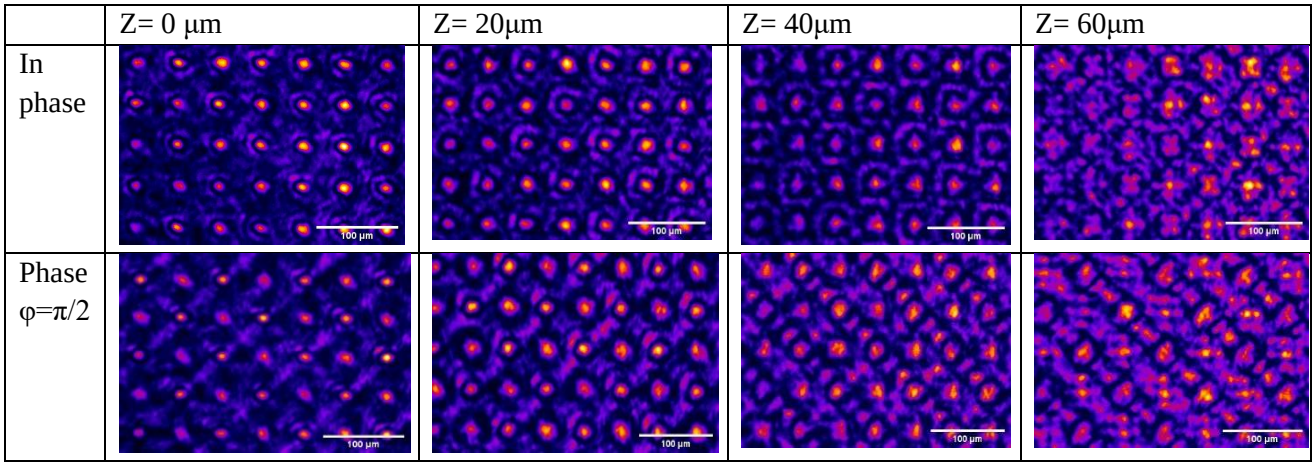

Figure 6.3.4.7: Comparison of the patterns that are produced at depth 0 to 60 μm from a) non-phase modulated multi-beam interference lithography and b) multibeam interference lithography when phase φ=π/2 rad is applied in central and lower left beam at five beam interference.

The final step of the study of five-beams interference was to apply a phase modulation on three of the five interfering beams. More specifically, we modulate the phase on the central and the two lower beams (pointed beams). As all the previous studies, the phases were φ=π/6 rad, φ=π/4 rad, φ=π/3 rad, φ=π/2 rad, φ=2π/3 rad, φ=3π/4 rad, φ=5π/6 rad, φ=π rad. In the following figure (6.3.4.8) the phase masks and the interference patterns of three significant phases are only presented. (φ=0 rad, φ=π/2 rad, φ=π rad)

	Phase mask	Interference pattern	Visual phase mask	Visual interference pattern
a	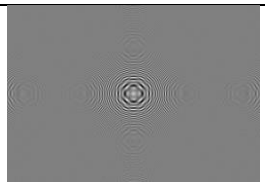		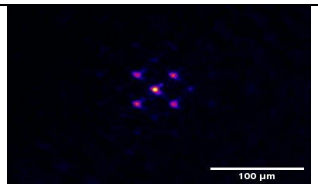	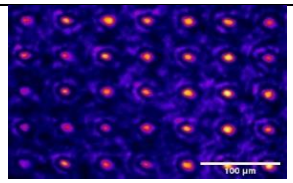
b	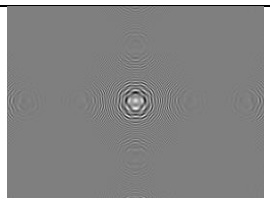	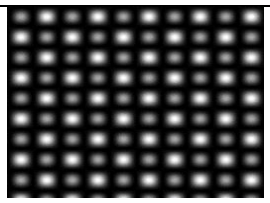	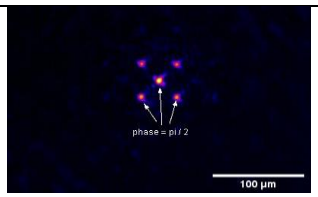	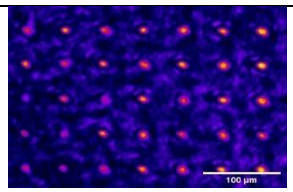
c	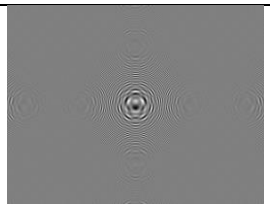	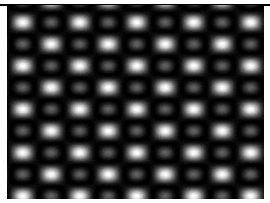	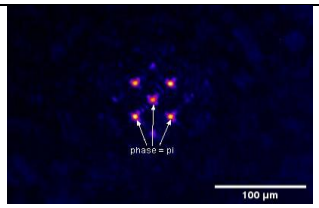	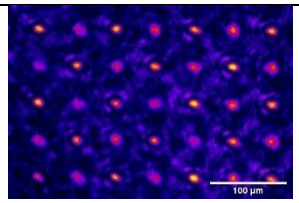

Figure 6.3.4.8: Phase mask, interference pattern and their visualization results for five interfering beams at distances 28.9 μm with a) no phase modulation b) phase φ=π/2 rad c) phase φ=π rad applied in the central and the two lower beams.

Chapter 7: Multiple-Beam Interference Laser Lithography

7.1 Introduction

Multi-beam interference allows the creation of diverse periodic light pattern intensity distributions, generated when two or more beams interfere. Here, we properly shaped the laser beam profile, generating different interference patterns, with the use of a Liquid Crystal on Silicon-Spatial Light Modulator (LCOS-SLM). The generated interference patterns in combination with a high nano-accuracy translation stages system, were used for the parallel processing of a photosensitive material by MPP, enabling the rapid fabrication of cm-scale periodic three-dimensional porous microstructures. The proposed method, accelerated the processing time up to 100 times in comparison with the conventional single point by point technique. The aim was to fabricate large area periodic structures with short fabrication time, fine surface and clear porosity inside the propagation axis. These structures will be used for photocatalysis applications.

7.2 Experimental set-up

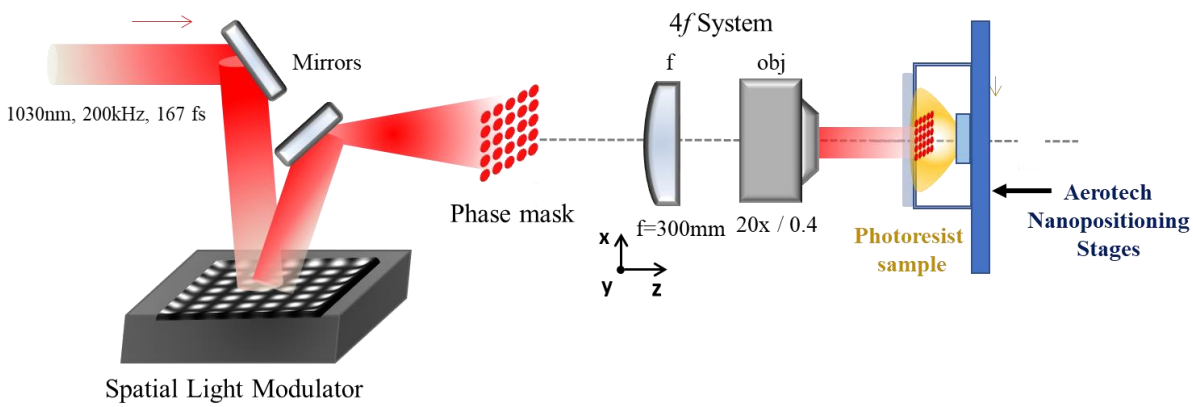

Figure 7.2.1: Schematic illustration of the multiple-beam interference lithography experimental set-up

The experimental setup of the multiple-beam interference lithography system based on SLM phase modulation is schematically depicted in the following figure. The excitation source of this experiment is a Diode-pumped Yb medium PHAROS Femtosecond Laser with wavelength of 1030 nm, 200kHz repetition rate and 167fs pulse duration incident to a Hamamatsu LCOS-X10468-2 phase-only reflecting SLM, with the appropriate

phase mask or hologram applied on it and generates the designed distribution at a specific distance.

Then the beam was focused into the volume of the photoresist material (SZ2080) after following a 4f optical system composed by a lens of *f*=300nm and an objective lens (20x NA=0.4). The sample was drop casted onto the top of the cover glass and was settled in a metallic base from Aerotech ANT95-L-Z (for z axis) and an ANT130-XY (for x-y axis) nano positioning stages system.

Sample preparation

Foe the sample preparation the following procedure was followed. First using a pipette, we placed a photoresist droplet (SZ2080) on a cover glass with the drop casting method. After that, we placed the samples on heating at a constant temperature of 35-40 degrees. In order to have uniformity, we try to make the sample as flat as possible in its entire size. After a few hours the material is ready for photopolymerization. The following figure shows a simple schematic procedure of the sample preparation while the right image is a real capture of the sample before it placed in the processing system.

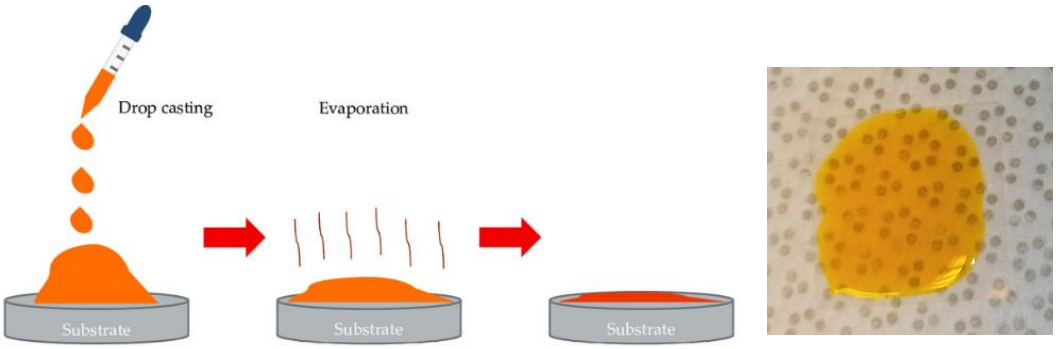

Figure 7.2.3: This is a typical process of a photoresist material is placed either in cover glass (left) and the sample before the processing system (right).

7.3 Results

7.3.1 Fabrication of the 3D porous periodic structure by Multi-Beam Interference Lithography

A porous 3D periodic structure can be fabricated by Multi-Beam Interference Lithography. More specifically we input into the SLM a four-beams interference pattern mask. In the following image the four-beams interference mask that was employed for the experimental part of this thesis, is presented.

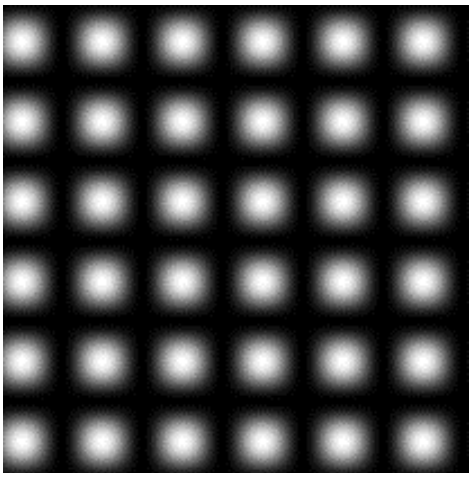

Figure 7.3.1.1: Presentation of the four-beams interference pattern mask used for this experiment

Then using a femtosecond laser, the beam is focused into the volume of the photoresist material (SZ2080). The reason behind of the reduced fabrication time up to 100 times is presented below. Inserting the four-beams interference pattern mask and let it interact with the photoresist materials (SZ2080) someone can actually produce instantly 100 voxels. So, when someone manage to move through the volume of the sample these spots either by moving the stages or via a modified code can achieve faster fabrication and parallel processing. In the following image (7.3.1.2) these 100 voxels are illustrated.

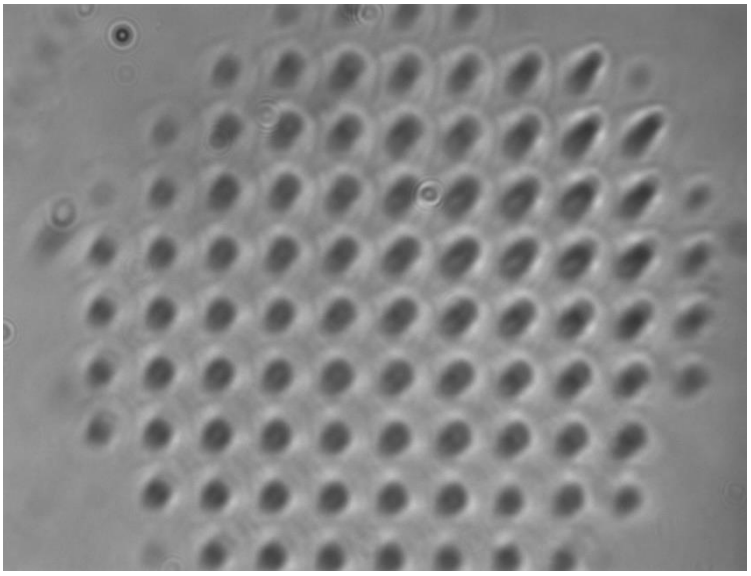

Figure 7.3.1.2: Capture of the 100 voxels from a camera connected to a PC which from this point we can observe the fabrication procedure

The following structure (figure 7.3.1.3) has an array of 500μm x 500μm and the total fabrication time was 15:38 minutes. The total power was 500mW or 2.50μJ. This was the first attempt of fabrication microstructures. Based on previous studies we investigate the parameters that we had to insert to a special designed code in 3D poli software that we would be able to control the fabrication velocity, the energy, the stages velocity of the Aerotech and the height and the length of the potential fabricated microstructure. If someone closely observe the following figures, there was a clear porosity for achieving flow in the propagation axis, but this attempt clearly needed optimization. **With this powerful technique we managed to reduce the fabrication time compared with the point-by point printing up to 100 times**. The reason behind of the reduced fabrication time up to 100 times is presented below. Inserting the four-beams interference pattern mask and let it interact with the photoresist materials (SZ2080) someone can actually produce instantly 100 voxels. So, when someone manage to move through the volume of the sample these spots either by moving the stages or via a modified code can achieve faster fabrication and parallel processing. In the following image these 100 voxels are illustrated.

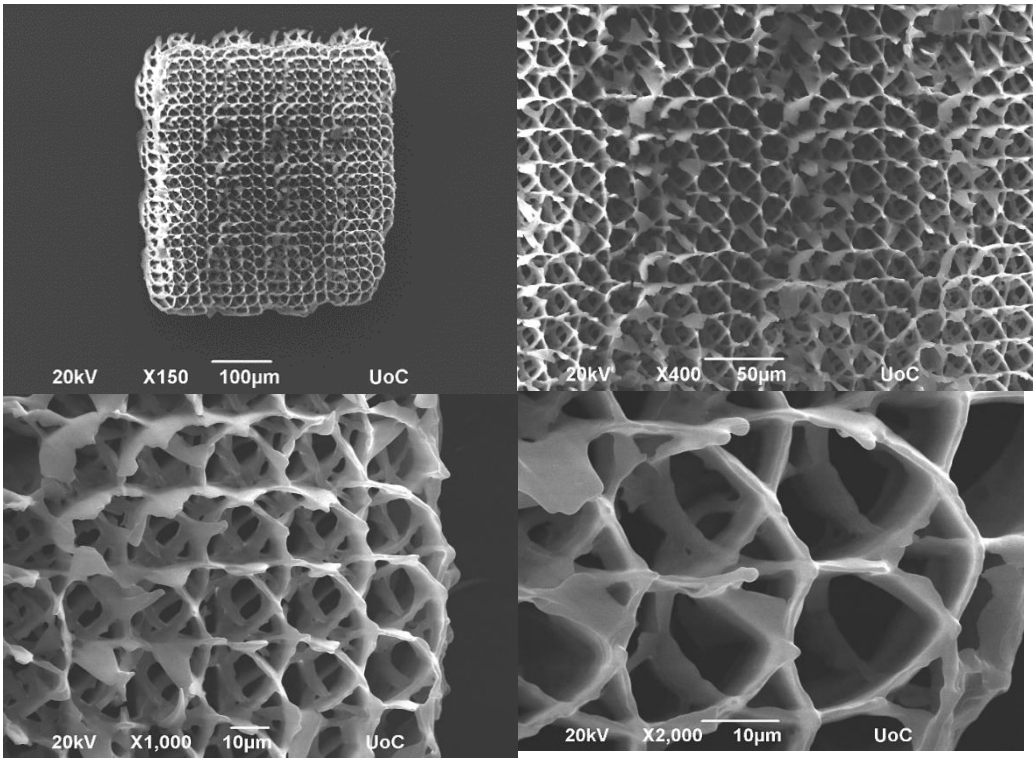

Figure 7.3.1.3: SEM images of a three- dimensional periodic porous structures. Panoramic view of the fabricated array and zoomed figures of the structure.

Based on the previous attempt (see figure 7.3.1.3) we tried to optimize both the fabrication time and the quality of the periodic structure. During several attempts, we also manage to improve the structure's array. Making a mapping of different fabrication energies and scanning speeds, we achieved an optimum combination of the processing parameters. In particular, we fabricated a periodic structure of 1000μm x 1000μm structure and the total fabrication time was 5.10 minutes. In figure 7.3.1.4 this fabricated structure is showed while it is really important to mention that we achieved a **12x faster fabrication in comparison with the previous attempt**. The total power was 694mW or 3.47μJ. It can also be noticed that the structure had a higher in volume porosity and the thickness of the spirals was even better (see figure 7.3.1.3 compared with figure 7.3.1.4). Last but not least, the following structure had a better mechanical stability than the previous one.

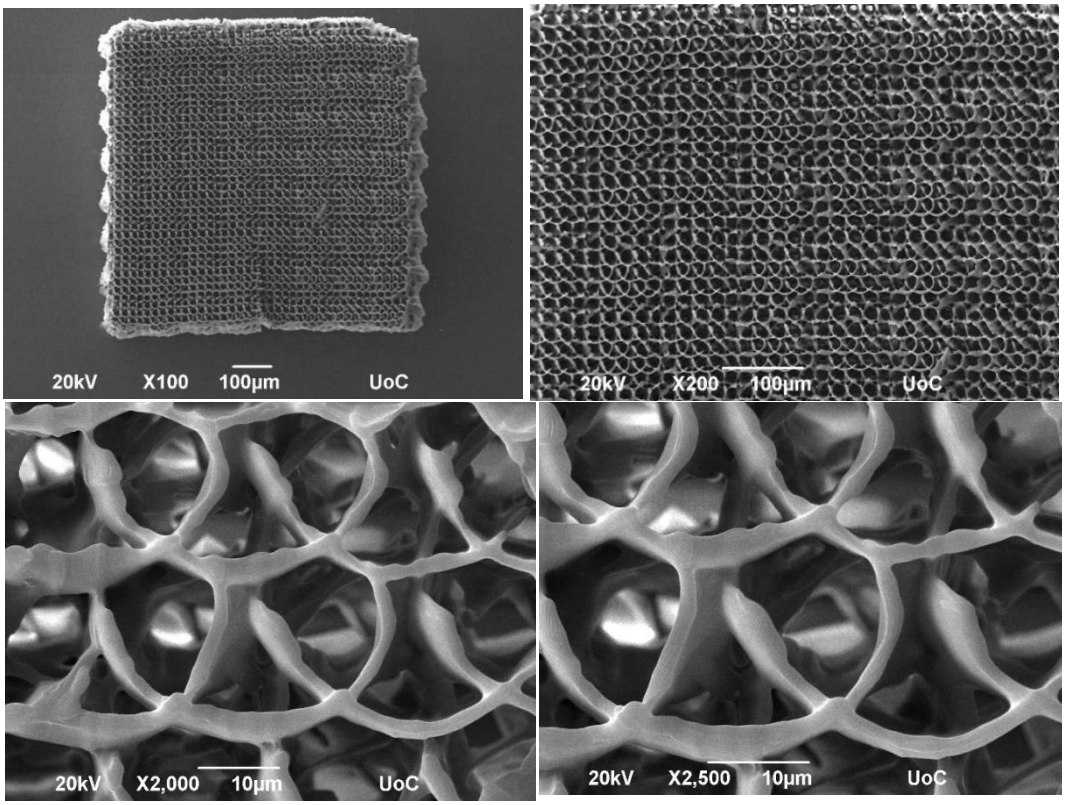

Figure 7.3.1.4: SEM images of the fabricated three-dimensional periodic porous structures. Panoramic view of the array and zoom in figures taken

Trying to reduce even more the fabrication time we decided to change the photoinitiator that we used into the photoresist hybrid material (SZ2080). The photoinitiator was EOSIN-Y which we also mentioned in the theoretical part of this thesis. The advantage that EOSIN-Y against BIS is the fact that the absorption wavelength is at 517nm leading in two-photon polymerization instead of three-photon polymerization (phenomenon with BIS because it absorbs at 348nm wavelength). So, we fabricated this time a bigger array (3500μm x 3500μm) with total fabrication time 27:00 minutes **(4x faster if we repeat the equivalent structure with PI: BIS.** As concern the porosity of the structure was every bit as the previous but it needed a bit of optimization.

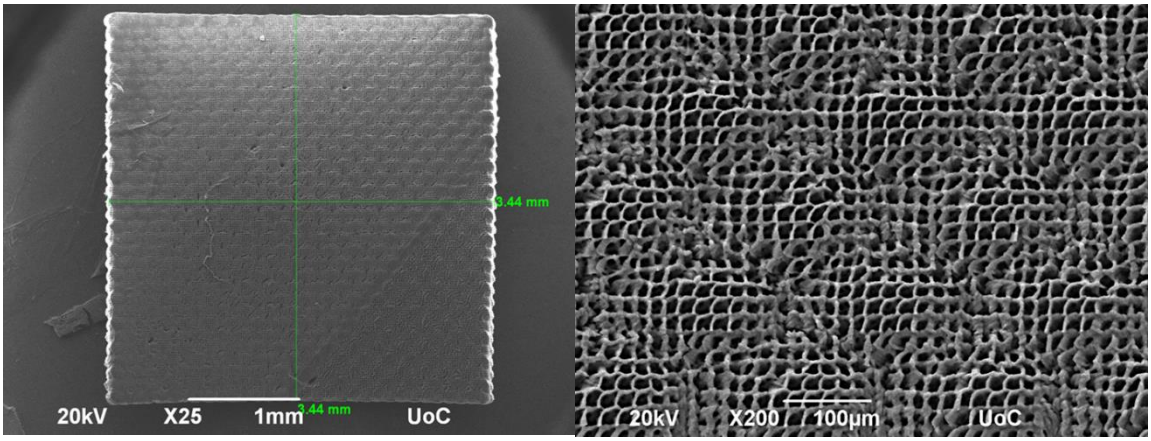

Figure 7.3.1.5: SEM images of the structure. Panoramic view (left). More detailed capture (right).

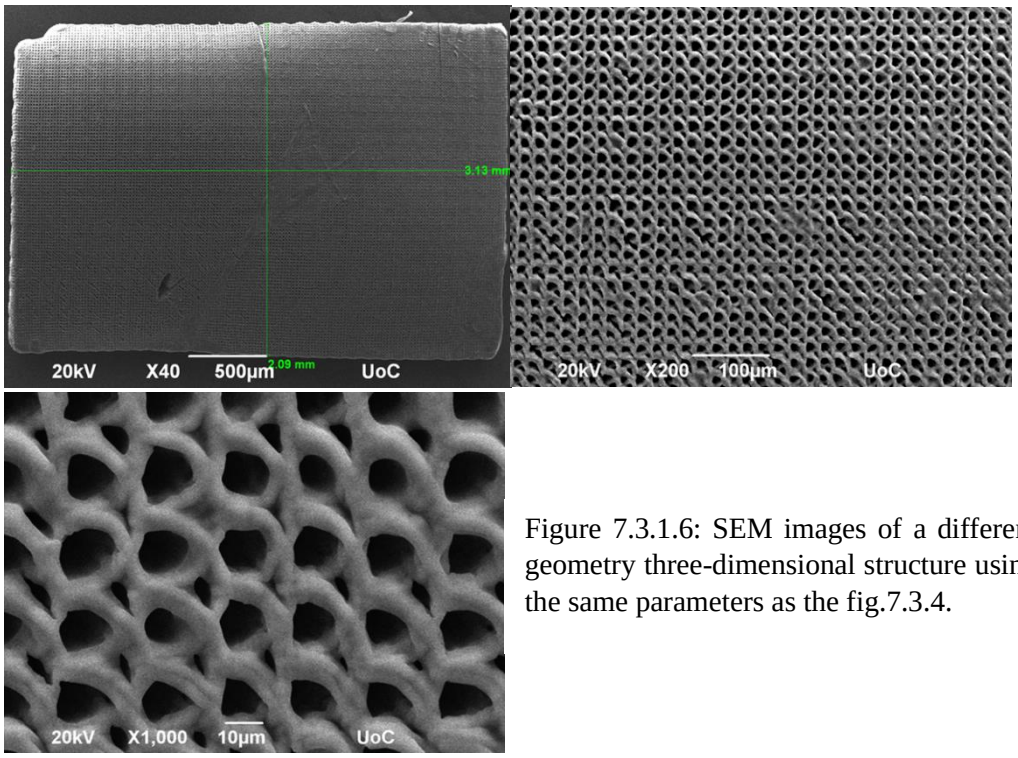

Figure 7.3.1.6: SEM images of a different geometry three-dimensional structure using the same parameters as the fig.7.3.4.

However, two major problems were noticed when larger area was fabricated. Specifically, the structures presented low mechanical stability such as cracks in different points along the array and the edges were raised due to the surface tension between the structure and the cover glass (see figure 7.3.1.7). As the time passed, the edges came back to normal but this behavior led to further cracks. As a result, we tried to dope to the photoresist hybrid material (SZ2080) DMAEMA and EOSIN-Y but the result remained the same.

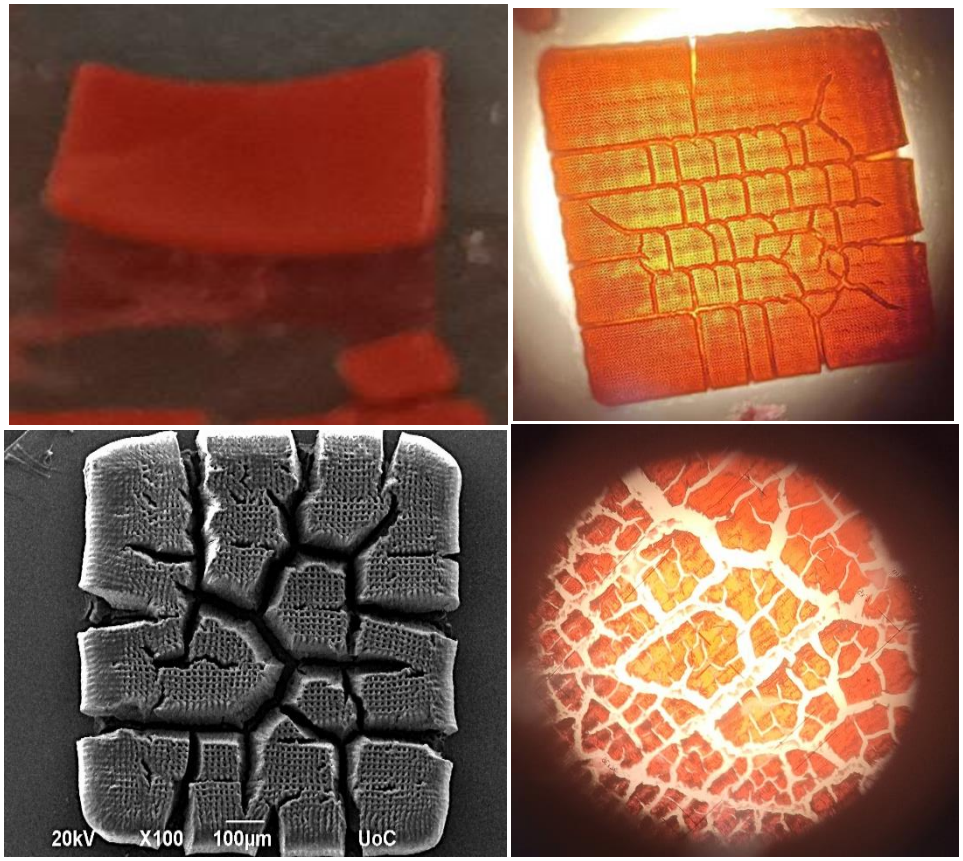

Figure 7.3.1.7: Illustration of the problems that we faced with EOSIN-Y a) unorthodox behavior

b) Optical microscope shot (SZ2080+DMAEMA+EOSIN-Y)

c) SEM image of the “damaged” structure with PI: EOSIN

d)Optical microscope shot of the “damaged” structure (SZ2080+PI: EOSIN)

After the previous attempts we tested a new material. The new material was Ormocer - PI: EOSIN. Photopolymer ORMOCER® (ORganically-MOdified-CERamic, MicroResist) is a widely used hybrid material and it is the commercially available. This material comprises an inorganic (–Si–O–Si–) backbone which can be functionalized with a range of organic functionalities. ORMOCERs are often used as dental composites, as electrolytes for lithium batteries, as membrane materials for fuel cell applications and in optical interconnect technology. It is considered as a very attractive option for the fabrication of photonic crystal structures and devices based on its good mechanical, optical and processing properties.[43] Unfortunately, this material was not ideal for our purpose because it needed more fabrication time and this was dissent to our initial cause of this particular bachelor thesis.

Following the decision to reuse photoinitiator BIS (absorbs at 348 nm), the fabrication of large cm-scale three-dimensional periodic porous structures was obtained. Looking again at 7.3.1.4 we tried to improve the conditions of that structure because now we were in the process of construction not 1000μm x1000 μm but 1.0 cm x 1.0 cm which is 10 times larger. The following figure shows a 1.0 cm x 1.0 cm structure with total fabrication time 8 hours and 30 minutes. The energy used by the Pharos Laser was 720mW or 3.6 μJ, the velocity of the processing was 50 μm/sec. It can also be noticed that the structure had a high in volume porosity. Finally, it is really important to mention that we achieved **100 times faster fabrication than the conventional point by point writing technique.**

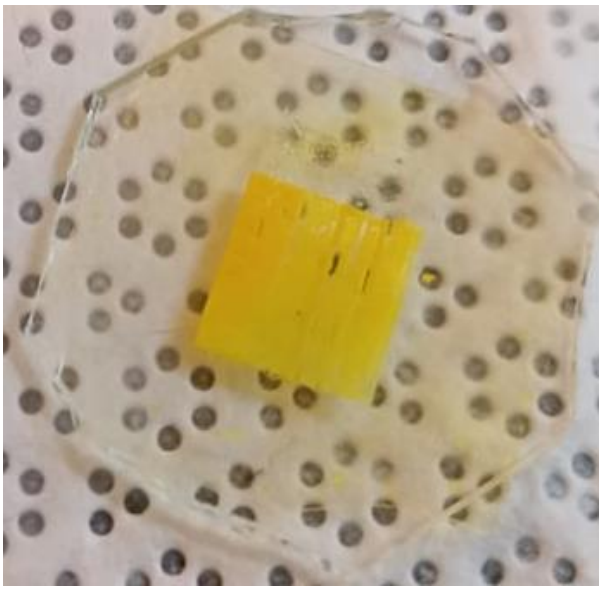

Figure 7.3.1.8: Real capture image of the fabricated three-dimensional periodic structure of total array 1.0 cm x 1.0 cm

The visual representation of the structure as shown in the following figures were recorded using the JEOL JSM-6390 LV model, at an accelerating voltage of 15 kV with the help of Ms. Manousaki Aleka. Scanning Electron Microscope (SEM) is a technology that uses a beam of electrons to scan a sample and create images of it. The electrons interact with the various atoms present on the sample surface, producing a variety of signals that give information about the shape and composition of the sample surface. (Resolution 1nm-20nm). Before placed the samples to the SEM, our samples have been sputtered for sputtering coating with Au for 39´´. The sputtering device that has been used was a Sputter-coater SCD050. [44]

Figure 7.3.1.8: SEM device: JEOL JSM-6390 LV
Sputtering device: a Sputter-coater SCD050.

Chapter 8: Pulsed Laser Deposition and ZnO growth results

8.1 Pulsed Laser Deposition technique

8.1.1 Experimental process and set-up

As we mentioned earlier, for the process of PLD we need an outside energy source (laser). In the following experiment the energy source that has been used was a KrF excimer laser (Lambda-Physik LPX 200) operating at 248nm and its pulse's duration last 30 nanoseconds (ns). Also, we were capable of adjusting its repetition rate as well as its operating voltage. A set of mirrors was used in order to guide the laser beam to a vacuum chamber. There was a spherical lens (f=+30cm) before the chamber, with aim to focus the laser beam into a spot irradiating the target. A power meter was utilized to measure the laser beam energy just before the chamber, thereby the error from the measurement is minimized. The laser beam was introduced to vacuum chamber through an optical window and a quartz glass which allows only light from the laser beam to pass. The chamber comprised a vacuum pumping system, a vacuum gauge, a rotating target holder and a substrate holder. The pumping system consists of a mechanical pump which is employed to create a preliminary low-vacuum on the order of 10^{-2} mbar and a turbomolecular pump which was activated at this point in order to reach the pressure on the order of 10^{-6} mbar. These vacuum conditions were essential for plume propagation and pure film growth. A Pirani and a Penning gauge were used to check the vacuum conditions. The first gauge was used to measure pressures between (10^{3}-10^{-3}) and (10^{-3}-10^{-8}) mbar, while the second gauge was used to measure pressures between (10^{-3}-10^{-8}) mbar.

The target material was a bulk zinc pellet (Zinc foil 99,95 percent. Goodfellow), and the substrate sample was a 3D microstructure. Since it was a way to minimize crater formation, the target was rotated during laser ablation of material. Optical windows ran the length of the vacuum chamber, allowing the PLD process to be monitored. The pressure of an ambient gas within the chamber, as well as the temperature of the substrate, were two critical parameters in traditional PLD studies, however they were not investigated in this study. The first stage in the PLD process preparation was to align the optical path of the beam so that the laser beam irradiates the target material. In this technique, instead of irradiating a photosensitive paper with one pulse, it is possible to determine the laser spot size at the target. The laser spot size profile was captured in the paper, allowing its measurements to be measured. The vacuum chamber was sealed once the 3D structure is placed on the substrate holder with a target-to-substrate distance of 4cm and a 45° angle to the target surface. The desired vacuum conditions are achieved using the pumping system as well as the vacuum gauge described above. A power meter is used to measure the energy of the laser beam at this position. Since the laser beam's spot size was measured later, the laser fluence (energy/surface) could be calculated, and the fluence could be made to suit the desired

value by adjusting the laser beam's energy. The repetition rate is set to 10Hz, and the motor that moves the target holder is turned on. For all depositions in this experiment, the target's rotation speed and the target-to-substrate distance are kept constant.

The number of pulses (2000 pulses) on the target throughout the experiment can be adjusted, either by the repetition rate or the total time of the deposition:

$$total\ time(s) = \frac{number\ of\ pulses}{repetition\ rate(Hz)} = \frac{2000}{10\ Hz} = 200s = 3.20\ minutes$$

Consider that the previous procedure has been completed both pumps were isolated from the chamber and turned off. Then the laser ablation and the film growth can be completed too. When the chamber got unsealed, we could observe that the three-dimensional structure was now coated by a thin film of Zn. In the follow picture it is illustrated the experimental set-up which was used in this thesis. [45], [46] , [38] , [47]

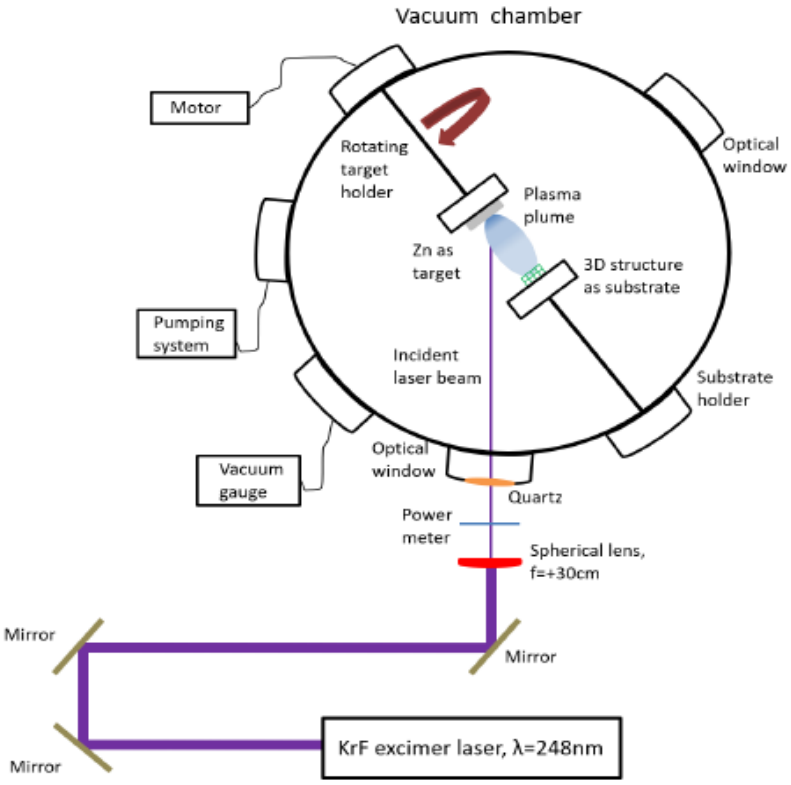

Figure 8.1.1.1: Pulsed Laser Deposition experimental set-up

8.1.2 Results

8.1.2.1 Deposition of thin fim of Zn in polymer film

Initially, in order to check the efficiency but also the smooth operation of both the process of PLD and the aqueous chemical growth of ZnO NRs, we placed our photoresist material (SZ2080) on a microscope glass. This sample was placed under a UV lamp to achieve polymerization and then was ready for the process. Once the vacuum of the chamber had reached the desired number (6.3 x 10^{-6} mbar) ,we placed the sample in the chamber and the irradiation of the sample began. The irradiation duration was a total of 3 minutes and 20 seconds having a repetion rate at 10 Hz ,the total number of pulses was 2000 and the polymer film was placed on the substrate holder with a target-to-substrate distance of 4cm and a 45° angle to the target surface. The total energy was 3 J/cm^2. Note that during irradiation the sample was rotating. After the irradiation was completed, we opened the chamber we noticed that our sample had changed color (tends to dark gray). This indicates that the PLD experiment was successful. The following picture is a real capture during the plasma creation and expansion during PLD (see figure 8.1.2.1.1). The following figure (8.1.2.1.2) show the polymer film before and after irradiation based on the Pulsed Laser Deposition technique

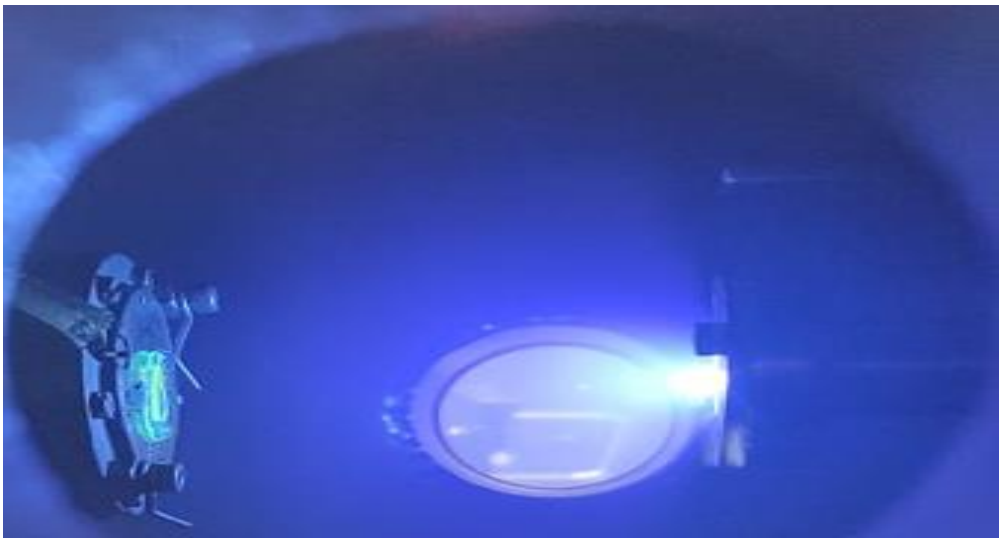

Figure 8.1.2.1.1: Real capture of the plasma creation and simultaneously plasma expansion to the sample

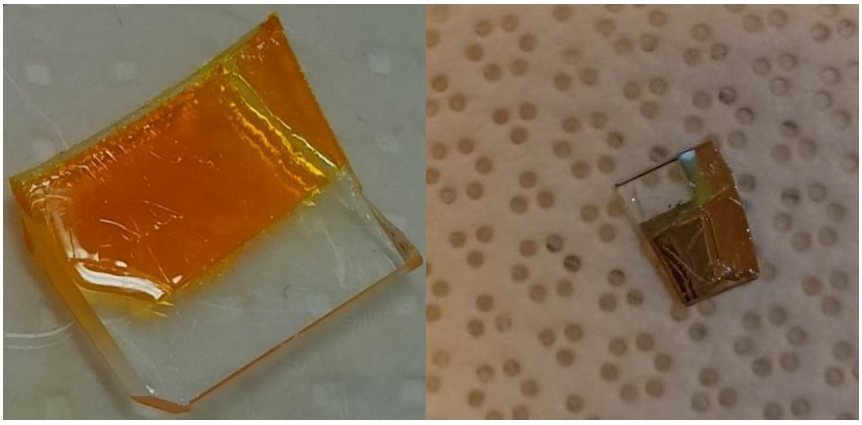

Figure 8.1.2.1.2: Polymer film before PLD (left) and polymer film after PLD (right).

8.1.2.2 Deposition of thin film of Zn in the three-dimensional porous structures.

Since the procedure that was followed for the synthesis of ZnO Nanorods was successful, we repeat the same steps and parameters for coating with a thin film of Zn the three-dimensional cm scale periodic porous microstructures. After the irradiation was completed, we opened the chamber waiting to calm down the mecahnical forces and noticed that our sample had changed color (tends to gray). The following figures show the three-dimensional porous structures before and after irradiation based on the Pulsed Laser Deposition technique.

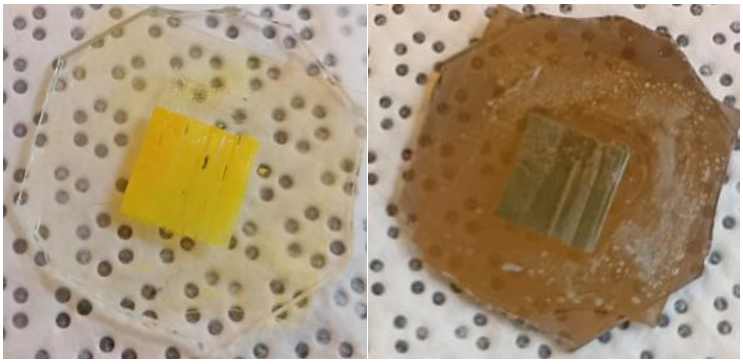

Figure 8.1.2.2.1: Fabricated three-dimensional periodic structure before PLD (left) and after PLD (right).

8.2 ZnO growth technique

8.2.1 Aqueous Chemical Growth

Aqueous chemical growth (ACG) is a simple solution growth approach for growing nanostructures of diverse materials that is fairly straightforward. It is carried out at low temperatures, which has various advantages, including the use of low-cost equipment, the employment of inexpensive and non-toxic chemicals, and the existence of non-hazardous by-products. The large size of development area combined with the fact that low temperatures are required is one of ACG's major benefits over other growth processes such as physical vapor deposition (PVD) and vapor liquid solid (VLS). [48],[49]

8.2.1 Aqueous Chemical Growth Process

Sigma-Aldrich provided all of the chemicals utilized in this bachelor's thesis. Zinc nitrate hexahydrate ($Zn(NO_3)_2 \cdot 6H_2O$, 98%) and ammonium hydroxide solution in water (28 wt% NH_3 in H_2O). To make a 0,02M growth solution, a calculated amount of zinc nitrate hexahydrate was dissolved in 100mL of deionized water. The pH of the growth solution was adjusted using ammonia water. The amount of ammonia water added was 3.1 ml. As previously stated, a Zn thin film deposited on 3D structures is a critical parameter for the growth of ZnO nanorods because it serves as a seed layer to promote nanorod alignment on 3D substrates. Hydrothermally ZnO nanorods growth was carried out by suspending the 3D structures deposited with zinc, bottom up in a glass bottle filled with the growth solution. The growth temperature was selected at 95°C and growth time was 2 hours and 10 minutes approximately. After the chemical growth, the samples were removed from the solution and were immersed for few minutes in a solution of deionized water and they had been drying in air for another 15 minutes. The following figures represent a schematic illustration of the aqueous chemical growth of ZnO NRs and a real-time capture of the homemade chemical growth experiment. [38]

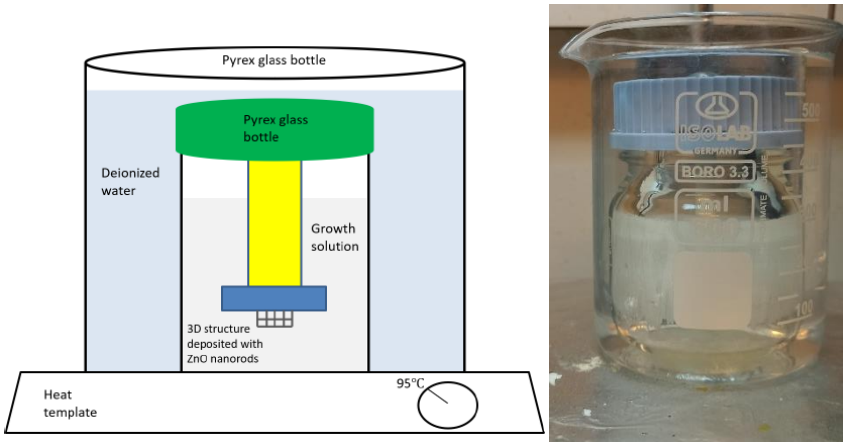

Figure 8.2.1.1: Presentation and real image of the chemical growth experimental set-up. The 3D structures are localized bottom-up in growth solution in order to form ZnO nanorods on them without gravitational effects.

8.2.1.1 Aqueous Chemical Growth on polymer film

As we mentioned earlier in the paragraph ***8.1.2.1***, we wanted to study the effectiveness of PLD and the Aqueous Chemical Growth as concern the photoresist material (SZ2080). Based on the [38] the following procedure for the ZnO growth started by counting 100mL of deionized water and we insert into a small Pyrex bottle together with 3.1ml ammonia and 0.02 M of Zinc nitrate hexahydrate ($Zn(NO_3)_2 \cdot 6H_2O$, 98%). When the water reached 95 degrees, we started counting for 2 hours and 10 minutes and then we placed small magnets outside the small bottle so that hitting the wall of the inner bottle would create a light stirring that would help the zinc to stick on the film which we had placed upside down.

During the experiment we checked in random times the amount of water that was in the outer bottle to permanently cover the inner bottle as well as the inner bottle not to rest on the thermometer that we had placed or on the walls of the outer bottle. After completing the experiment and dipping it in water and drying it in the air, we took images from the Scanning Electron Microscope (SEM) in various magnifications in order to see if either on the glass or in the polymer there were ZnO nanorods. (Figure 8.2.1.1.1 and 8.2.1.1.2). What we observe was that ZnO nanorods were developed in the surface of the glass and the polymer. The ZnO nanorods had uniformly growth because before the growth we deposited a seed layer of Zn in the sample. At this moment we were able to conclude that the technique works correctly and we could freely use it to develop ZnO nanorods on our three-dimensional fabricated periodic porous structures.

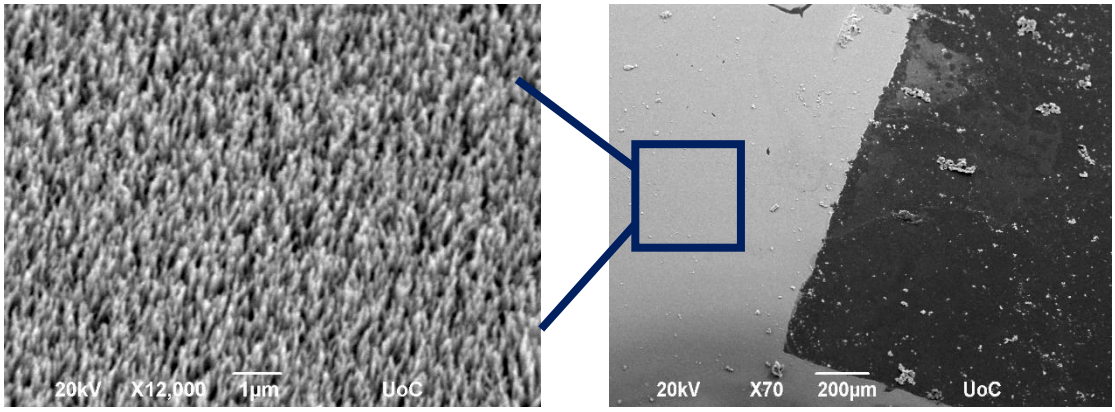

Figure 8.2.1.1.1: SEM images from ZnO nanorods on top of the glass after PLD and ACG technique

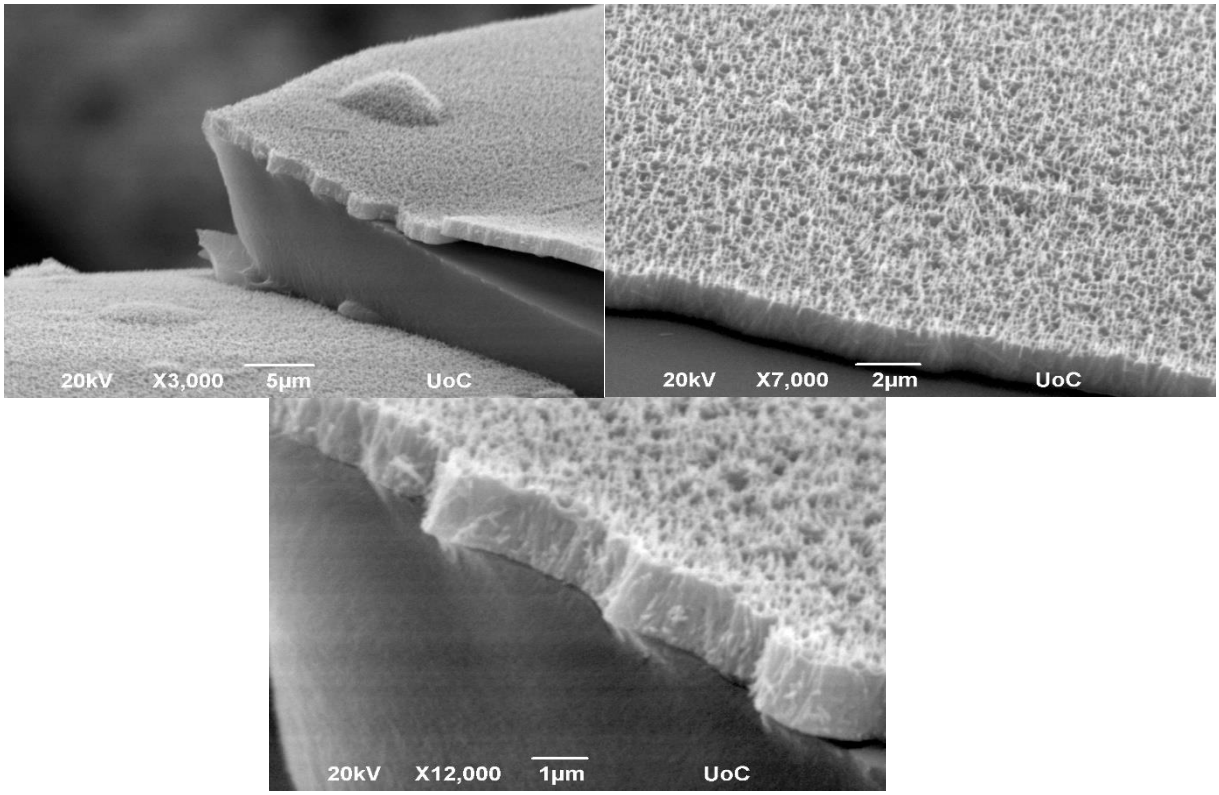

Figure 8.2.1.1.2: SEM images from ZnO nanorods on top of the photoresist material (SZ2080) after PLD and ACG technique

8.2.1.2 Aqueous Chemical Growth on the fabricated three-dimensional porous structure

Strictly maintaining once again the chemical synthesis procedure that we mentioned in the paragraph **8.2.1** [38] , when the water reached 95 degrees, we started counting for 2 hours and 10 minutes. From what we could able to see is that the color was less yellow than before tending to white giving as an early conclusion that the ZnO nanorods have been decorated on the fabricated porous structure. Figure 8.2.1.2.1 shows the sample after the ACG procedure which was used for testing its photocatalytic efficiency as three-dimensional nanodevice. The photocatalytic activity of the ZnO NRs-coated 3D porous devices will be quantified by measuring the decolorization of methylene blue (MB) in aqueous solution.

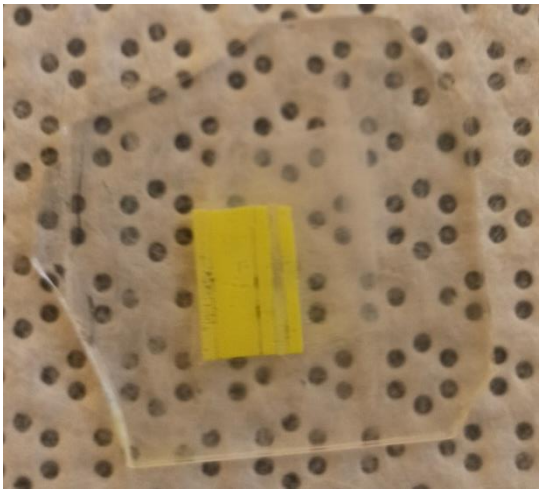

Figure 8.2.1.2.1: Real capture image of the fabricated three-dimensional periodic porous structures after the growth of ZnO nanorods via the Aqueous Chemical Growth technique

Chapter 9 : Photocatalytic activity Results

9.1 Introduction

The activity of photocatalytic surfaces can be determined using a variety of techniques. Photo-oxidation of organic films such as stearic acid, methylene blue photodegradation in aqueous solutions, and contact angle changes are all popular approaches. In this bachelor thesis in order to study the photocatalytic activity of the three dimensional porous structures , the 3D structures was quantified by measuring the decolourization of methylene blue (MB) in aqueous solution.

9.2 Experimental Set -up

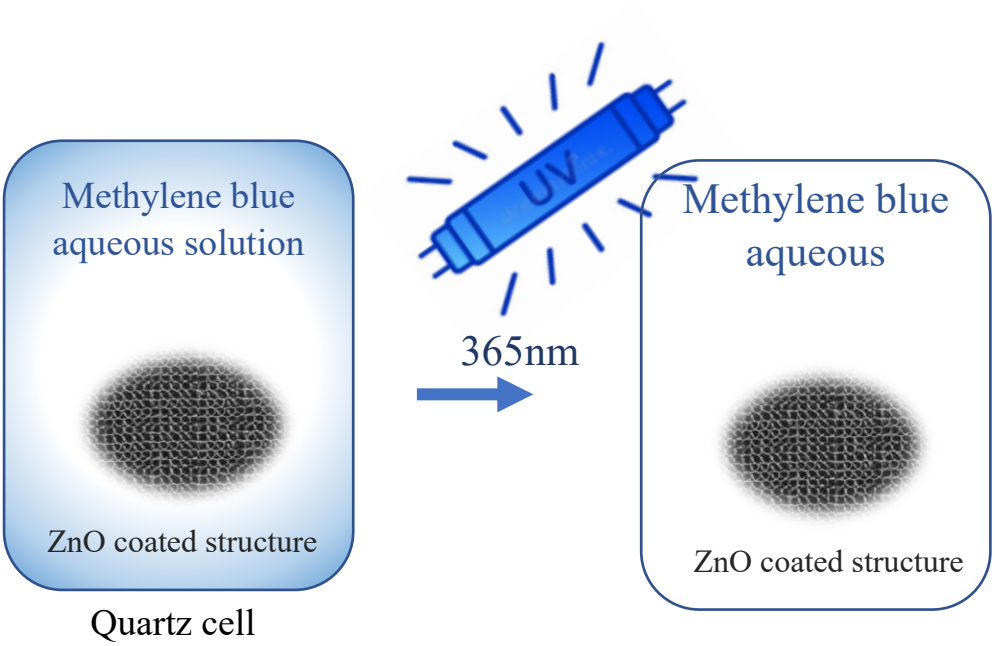

Figure 9.2.1: Schematic Illustration of the Experimental process. Decolorization of methylene blue in aqueous solution under UV illumination over time

This is a typical schematic experimental process where the samples were placed in a custom made quartz cell, and the whole setup was illumi nated for up to 60 min using a UV lamp centred at 365 nm (Philips HPK 125 W), with a light intensity of ~10 mW/ cm^2 . The cause of this experiment is the decolorazation of methylene blue in aqueous solution[38]. In generally, when ZnO is excited by UV light, the semiconductor absorbs photons whose energy is equal to or greater than their band-gap energy E_G ($h\nu \geq E_G$), and they created electrons and holes. The degradation process then consists in a succession of radical oxidations initiated by strong oxidants such as OH· and $\cdot O_2$. . Oxidants are directly generated by the photolysis of water molecules adsorbed by the

active sites of SM. Organic pollutants adsorbed on the catalyst are then degraded by successive radical reactions in non-toxic mineral species. In the following figure the chemical reactions from the UV light excitation of ZnO to the photodegration of Methalyne Blue is presented. [50] ,

$$ZnO + hv \rightarrow h^+ + e^-$$

$$H_2O + h^+ \rightarrow H^+ + {}^{\cdot}OH$$

$$h^+ + OH^- \rightarrow {}^{\cdot}OH$$

$$e^- + O_2 \rightarrow O_2^{\cdot -}$$

$$O_2^{\cdot -} + H_2O + H^+ \rightarrow H_2O_2 + O_2$$

$$O_2^{\cdot -} + \text{organic species} \rightarrow \text{organic species}-OO^{\cdot}$$

$$-OH + \text{Organic species} \rightarrow \text{oxidized product}$$

Figure 9.2: Chemical reactions during photodegradation of the pollutant

9.3 Methylene blue photodegradation Results

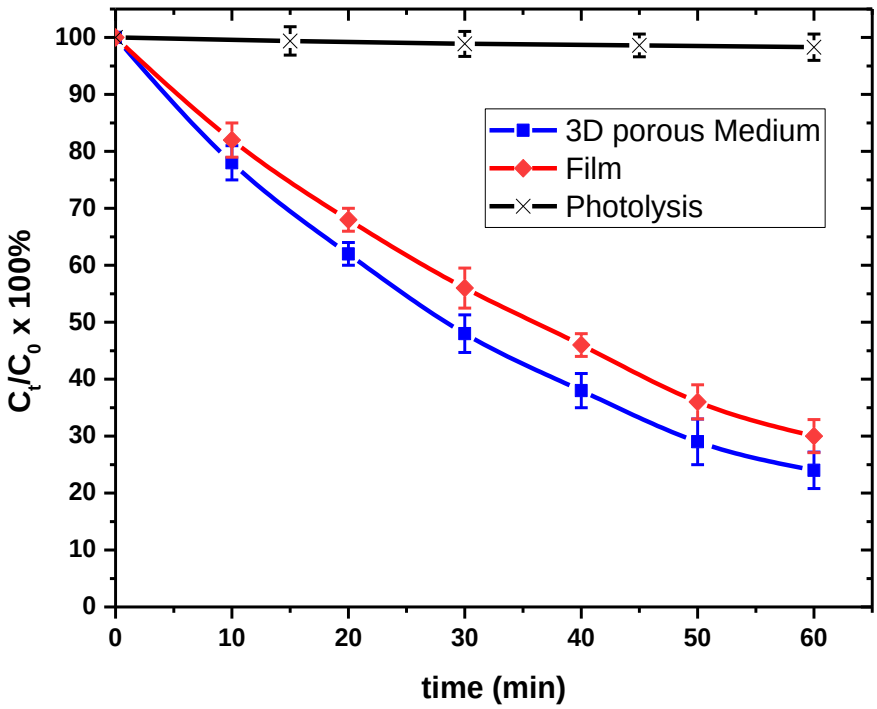

Figure 9.3.1: Graph showing the decrease of the MB concentration over time

For quantifying the ZnO induced MB concentration decrease and the photocatalytic activity of the various structures the apparent rate constant (k) has been estimated, according to :

$$\ln\left({C_t}/{C_o}\right) = -kt$$

Where C_0 is the initial MB concentration, C_t is the concentration after a time interval t and k is specific rate constant for the first order kinetics reaction.

	Photolysis	Polymer Film	3D porous media
K (rate constant)	K_{phl} = 0,0003 min^{-1}	K_{film} = 0,0201min^{-1}	K_{porous}= 0,0241 min^{-1}

The black line refers to the photolysis where the polymer film is present without ZincOxide Nanorods having developed on the surface. Thus over time the concentration of MB (Methylene Blue) does not change as there is a lack of the semiconductor. The red line indicates a polymer film where this time we have grown ZnO Nanorods through the two step process. (PLD and ACG). Finally, the blue line indicates our three-dimensional porous structure coated by the ZnO Nanorods. As someone can observe from the graph, the rate constant (K) is bigger in the fabricated 3D porous structure giving us the conclusion that the decrease of the concentration of the Methalyne Blue was occurred much faster and that give prominence to the photocatalytic activity of our 3D porous structures. As the value of the k constant increases this means that we have a strong catalyst. The upper number is an preliminary but very promising measure for future work, indicating that indeed our structure has photocatalytic efficiency and the next step is the improvement of the photodegradation rate of the methalyne blue.Compared with previous works, [38] , we can observe from the Figure 6 on the ref [38] our result have similar photocatalytic activity with the 3D ZnO NRs coated sample of a 5 x 5 array.

3D cm porous media	Reference [38]
Kporous= 0,0241 min^{-1}	K_{ref}=0.0284 min^{-1}

Chapter 10 : Future Work

10.1 Introduction

Observing the promising results from the fabricated 3D porous structures, we decided to extend our research and test the photocatalytic efficiency of the fabricated ZnO coated structures that we construct through Multi-Beam Interference Laser Lithography in a more practical application, under flow dynamics. For this reason, a special flow platform was constructed where the structure fabricated on a specially designed porous substrate, will be placed in. Two adaptors are designed, one for inlet and one for outlet, by which the water will flow under a controlled rate. Finally, light the samples will be illuminated by UV light to permit the photocatalysis to be obtained. In the following images the flow platform is depicted. (Figure 10.1.1)

Figure 10.1.1: Presentation of the special designed flow platform for more realistic photocatalysis experiments.

The fabrication of the three-dimensional porous structures was made on the top of a cover glass, not allowing flow of liquids to be achieved due to porosity blocking. For this reason, we designed and produced by our own porous substrates that we will be placed inside the flow system platform having on top of them the fabricated three-dimensional porous microstructure.

10.2 Creation of 3D printed grid substrates

At first, we printed a structure of 1.2cm x 1.2cm plexus with 1.0mm height using (Anycubic Photon One) a 3D printer which is located at Dr. Farsari lab. The reason behind the design of these substrates was that our samples should be placed in as a substrate or a film to our porous substrates that will help the catalysis process. Additionally, we tried to design as much as holes possible considering how will boost the catalysis under the flow dynamics system. Each hole of the substrate has 620μm x 660μm length. The total production time for the 3D grid substrates was 5 minutes.

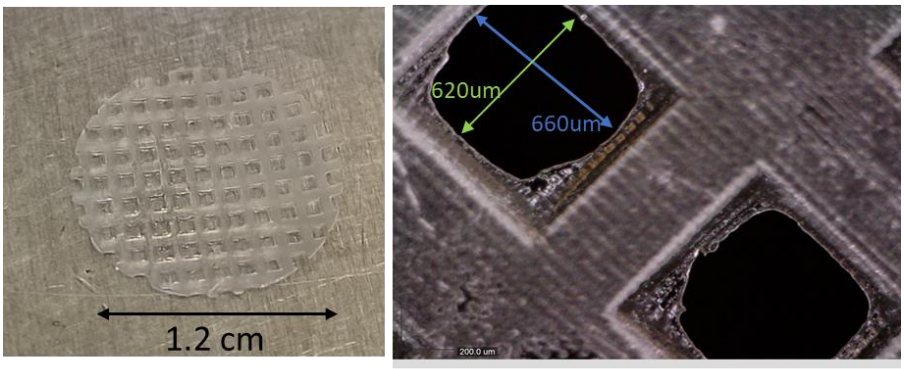

Figure 10.2.1: Optical microscope images of the 3D printed grid

We took the 3D printed grid structure and we placed a droplet of the photoresist material (SZ2080 PI:BIS).We follow exactly the same method used in the fabrication of the cm scale thrre-dimensional porous strucures. In the following figures (figure 9.2.2), we present the fabrication of the three-dimensional periodic porous structure with a clear and a exceptional porosity in approximately 1 cm x 1 cm array.(figure 7.3.2.2) and the total fabrication time was 8 hours and 30 minutes. The total energy that needed to fabricate the three-dimensional periodic structures was 720mW or 3.6 μJ. Either in a cover glass or up to a 3D printed structure the results are identical proving that multi-beam interference lithography is a trustworth technque when it comes for the fabrication of large scale and complex area microstructures. At this moment of the thesis, managing to maintain the same result was considered as a huge step for the upcoming experiments.

Sample preparation

Initially, using a pipette, we placed our photoresist sample (SZ2080) on top of the 3D printed grid substrates with the drop casting method. After that, we place the samples on heating at a constant temperature of 35-40 degrees. In order to have uniformity, we tried to make the sample as flat as possible over its entire surface. It is important to check at regular intervals because there is a possibility that a slight filling of material in some pieces is needed or sometimes in the samples have been creating bubbles. After a few hours the material is ready for photopolymerization. The following figure shows a simple schematic procedure of the sample preparation and the right image is a real capture of the sample before it placed in the processing system.

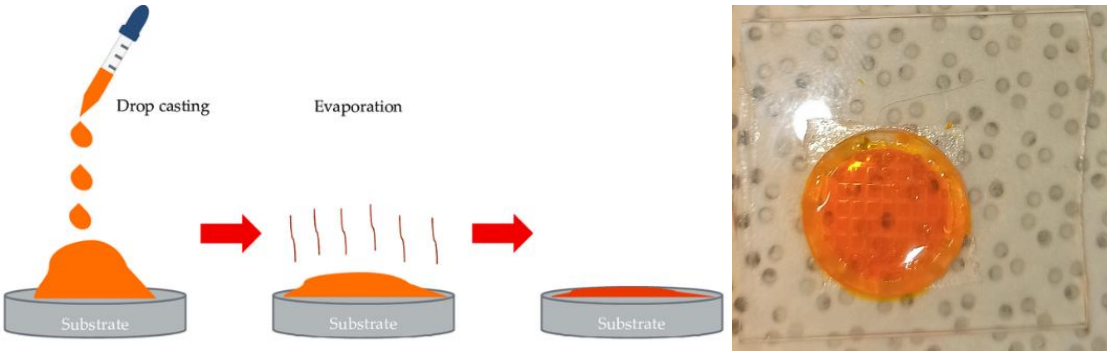

Figure 10.2.3: This is a typical process of a photoresist material is placed in the 3d grid substrate (left) and the sample before the processing system (right).

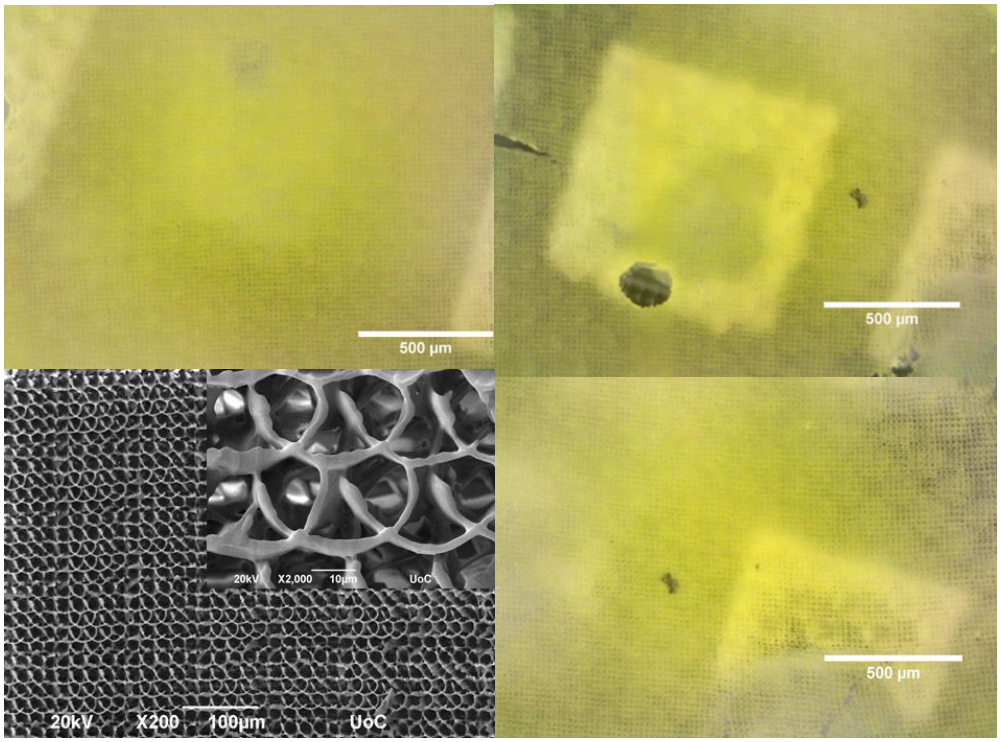

Figure 10.2.2: Optical microscope images of a three-dimensional periodic porous structure on top of a 3D printed grid structure.

Nevertheless, the 3d printed grid substrate had some mechanical instability over time, leading the corners to raise up resulting to damage the three-dimensional fabricated porous structure that we have fabricate on top of its surface. (See figure 10.1.3). For this reason, we printed a new grid structure, but this time we added a ring in the perimeter of the structure to help the mechanical stability of the fabricated periodic porous structure and to help the drop-casting process

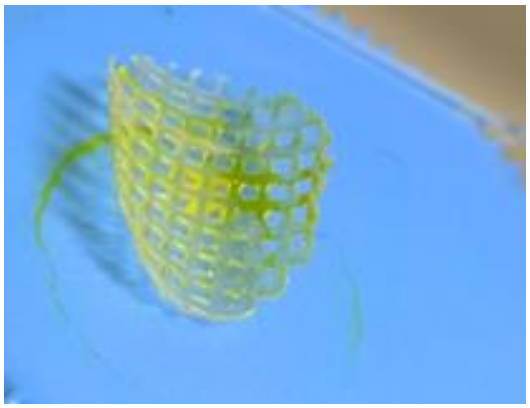

Figure 10.2.3: Real image showing the problem of the mechanical stability which lead to redesign the module of the 3D grid structure.

The new 3d grid designs were separated by two main categories: the first grid that we printed had smaller holes (150μm x 240μm) than the previous and the second one had bigger holes (800 μm x 800 μm) thinking beside the fact of how can we improve this mechanical failure but also which case will be more beneficial for the upcoming photocatalytic measurements inside a flow platform.

As concern the dimension of the first grid (See figure 7.3.2.4) we kept the same diameter (1.25 cm) and the height of the substrate was a bit taller because of the ring in the perimeter (1.56 mm). The holes size was (150μm x 240μm) diameter. The total production time for the 3D grid substrates was 7 minutes.

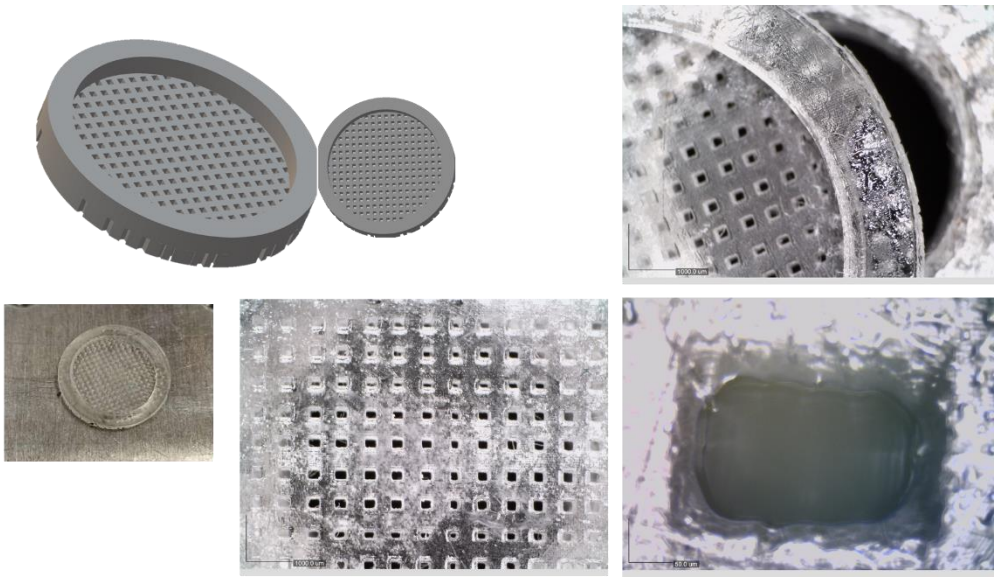

Figure 10.2.4: Optical microscope images of the 3d printed grid with ring and small holes into the surface of the structure.

In the following images, we present the fabrication of the three-dimensional periodic porous structure with a clear and a exceptional porosity in approximately 0.8 cm x 0.8cm array.(see figure 10.2.5) and the total fabrication time was 6 hours and 40 minutes. The total energy that needed to fabricate the three-dimensional periodic structures was 720mW or 3.6 μJ.

Once again there is a clear porosity but the structure never fully completed because of some software crashes. Even though the results tend to be very promising for the future.

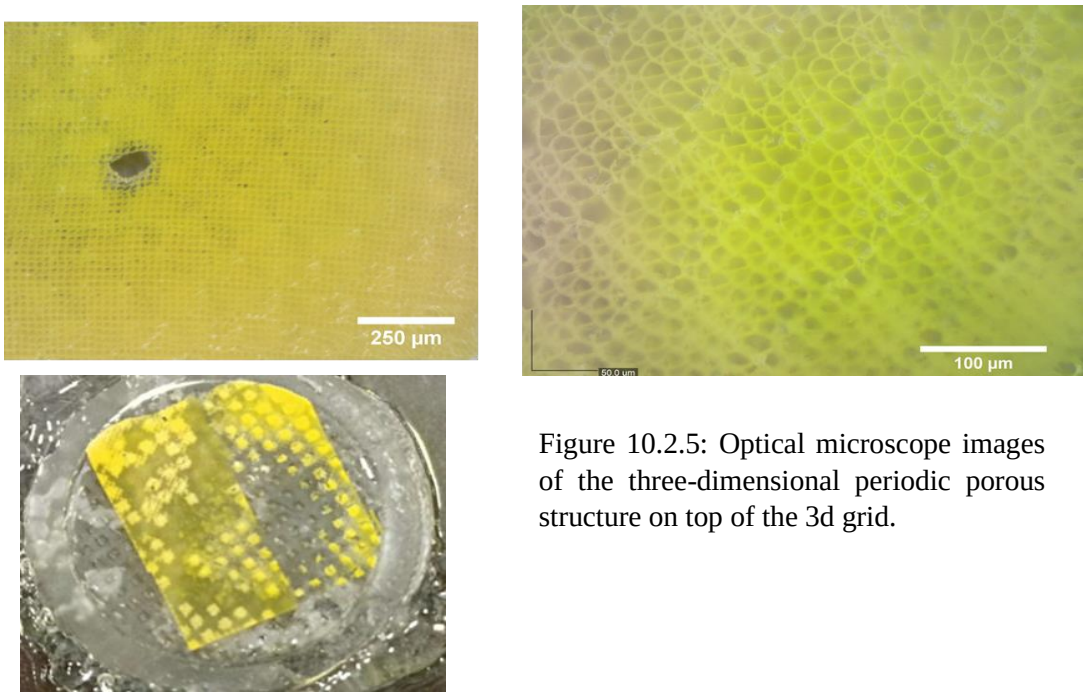

Figure 10.2.5: Optical microscope images of the three-dimensional periodic porous structure on top of the 3d grid.

The next step was to print the 3d printed grid with the larger holes (800 µm x 800 µm) to observe their efficiency. At first, we drop cast the photosensitive material (SZ2080-PI: BIS) and tried to fabricate three-dimensional periodic porous structures onto the surface of the substrate. In the following images there is the presentation of the new grid. The total production time for the 3D grid substrates was 8 minutes.

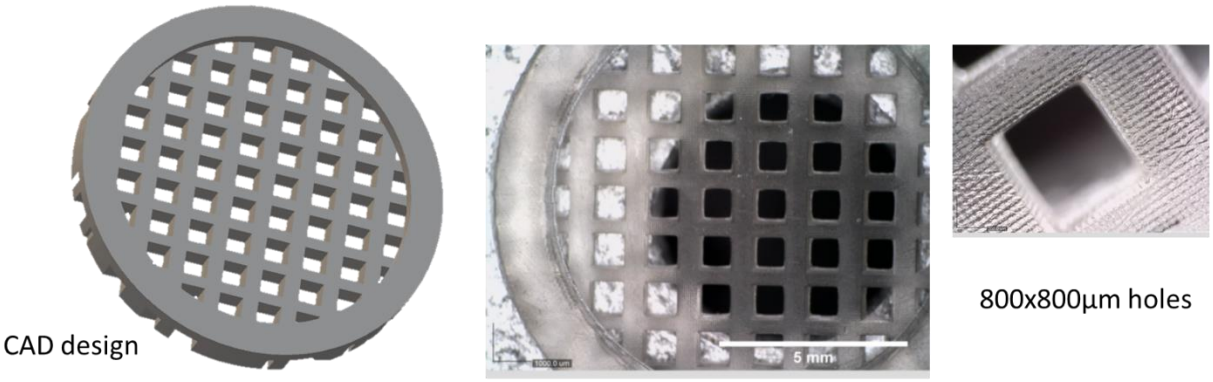

Figure 10.1.6: Optical microscope images of the 3d printed grid with ring and bigger holes into the surface of the structure.

In figure 10.2.7 we present the fabrication of the three-dimensional periodic porous structure on top of the 3d grid substrate with big holes. Once again there is clear porosity into the volume and the motif of the design once again remain the same. The total fabrication time of the structure was 8 hours 30 minutes and the structure's array were 1.0 x 1.0 cm. The total energy that needed to fabricate the three-dimensional periodic structures was 740mW or 3.7 μJ. In generally, it was very important that we manage to fabricate the periodic porous structure in both of the three different designs of the substrate because it shows that multiple-beam interference lithography is an exceptional technique which can easily respond to every circumstance that we imply it and the parameter study that we done it was correct.

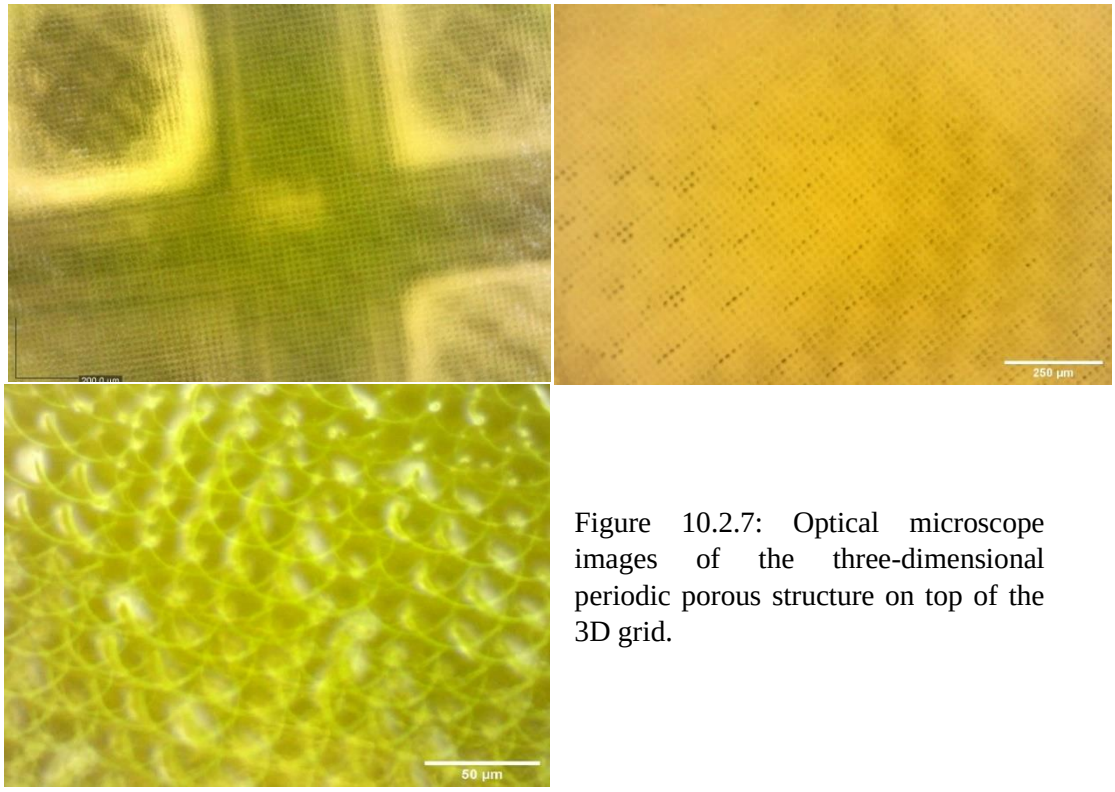

Figure 10.2.7: Optical microscope images of the three-dimensional periodic porous structure on top of the 3D grid.

10.3 Deposition of a thin film of Zn via PLD in the 3D printed substrates

The next step was to deposite a thin film of Zn into the 3d printed grid substrates.Following exactly the same experimental conditions (Repetition Rate 10 Hz , Number of Pulses 2000 , Target to distance 4 cm) cosidering the Pulsed Laser Depostion technique we noticed that after the irridation the color of the substratess was gray showing that a thin film of Zn had now covered the surface of the substrates.In the following pictures we present the 3D printed grid structures coated by a thin film of Zn. The two 3d printed substrates that been presented are the substrates with the ring holder for both the two categories that we have mentioned earlier. See figures (10.2.4 and 10.2.6). Also in figure 10.3.2 it presented the moment when our sample was removed from the vaccum chamber of the PLD.

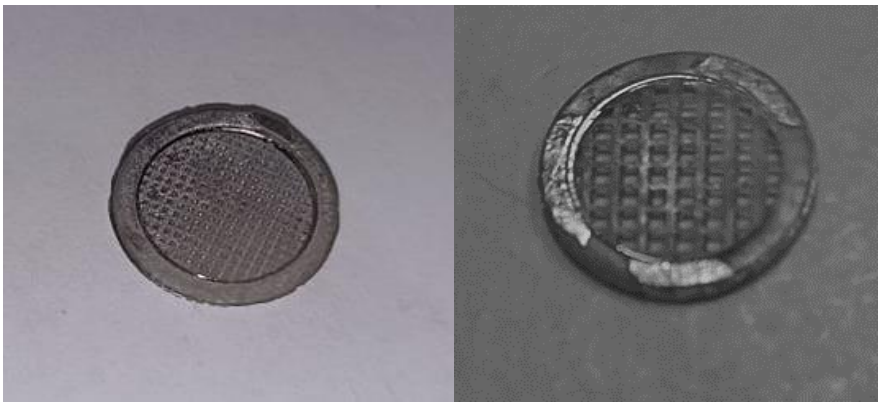

Figure 10.3.1: 3D printed substrates coated with a thin film of Zn using Pulsed Laser Deposition technique

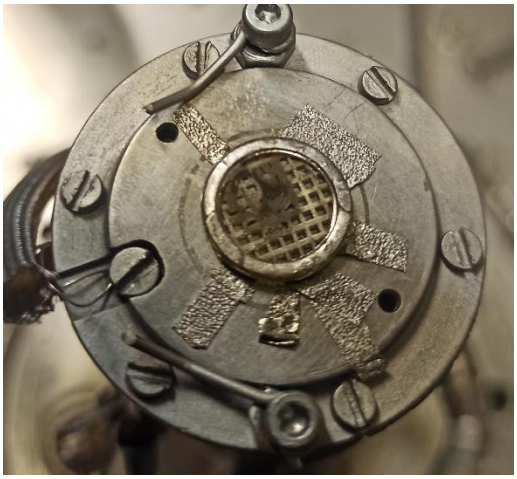

Figure 10.3.2: Real image after the irradiation of the 3D printed substrate coated with a thin film of Zn using Pulsed Laser Deposition technique

Since we used the Pulsed Laser Deposition technquie in the 3d printed grid substrates the next step was to make a thin film of Zn coating on the samples where the three-dimensional periodic strucutres were fabrcirated on the surface of these grids. In this case, too, the radiation parameters of the PLD were the same. After the end of the procedure, removing the target from the chamber, we noticed that the three-dimensional periodic strucutres had changed color (from yellow to dark gray) as well as the grit that surrounded it. The following photo shows the moment when our sample was removed from the vaccum chamber of the PLD (see figure 10.3.3).The following structure was the semi-completed strucutre that we have mentioned earlier (see figure 10.2.5) with an array of total 0.8cm x 0.8cm and total fabrication time 6 hours and 40 minutes.

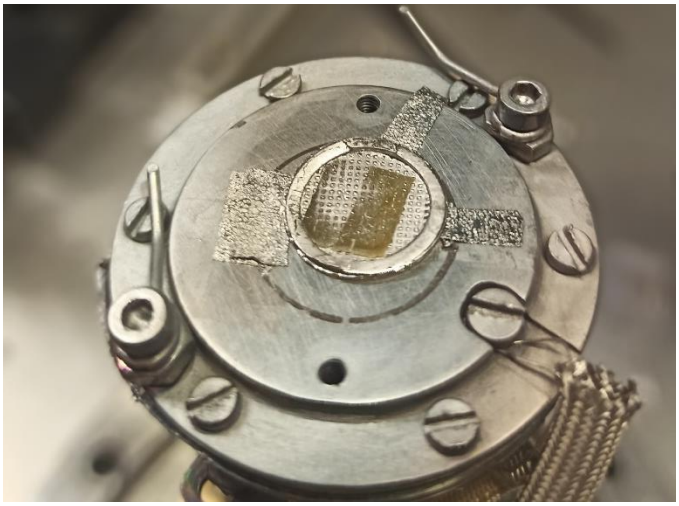

Figure 10.3.3: Real image after the irradiation of the fabricated three-dimensional porous structure on top of the 3D printed substrate coated with a thin film of Zn using Pulsed Laser Deposition technique

Our future perspective, having successfully coated the 3D printed grid substrates with a thin film of Zn, the next step will be to hydrothermally growth on these substrates ZnO Nanorods with the Aqeuous Chemical Growth technique. Keeping the same conditions regarding the chemical process and the proportions of the materials based on [38] we hope that there will be a successful development of nanorods on our samples. Finally, the three-dimensional nanodevices will be able to be measured within the specific flow platform with the aim of measuring their photocatalytic activity.

Chapter 11: Conclusion

In conclusion, Multi-beam Interference Laser Lithography by Multi-Photon Polymerization (MPP) is proposed as an alternative processing approach, for reducing the total fabrication time of centimeter-scale area complex micro-featured porous structures. A Spatial Light Modulator was employed for the direct generation of periodic laser interference patterns that were actively employed for the parallel processing of a photosensitive material by MPP. The rapid fabrication of cm-scale periodic three-dimensional porous microstructures was achieved while this promising method accelerated the processing time up to 100 times in comparison with the conventional single point by point Direct Laser Writing technique. Such large-scale area micro-porous structures can be ideal candidates for practical applications, such as photocatalysis, due to the high active surface they offer.

For this reason, ZnO nanorods were grown onto the surface of the fabricated structures based on a two-step process, Pulsed Laser Deposition (PLD) of a thin Zn seed layer followed by Aqueous Chemical Growth (ACG) hydrothermal synthesis of ZnO. The photocatalytic efficiency of the ZnO NRs-coated 3D porous structures was quantified by measuring the photodegradation of organic pollutants over time under UV light irradiation. The results showed that indeed our 3D porous structures present a promising photocatalytic activity and efficiency. Based on that, we design a flow dynamics platform that will allows us to test the photocatalytic activity of our 3D porous structures in a more realistic model. For this reason, the fabrication of the cm-scale periodic three-dimensional porous microstructures were accomplished on top of a 3D printed substrates and in future steps the growth of ZnO nanorods following the previous two-step process, and the photocatalytic efficiency under flow dynamics will be investigated.

References

[1] D. G. Papazoglou, M. Farsari, M. Manousidaki, and S. Tzortzakis, “3D holographic light shaping for advanced multiphoton polymerization,” *Opt. Lett. Vol. 45, Issue 1, pp. 85-88*, vol. 45, no. 1, pp. 85–88, Jan. 2020, doi: 10.1364/OL.45.000085.

[2] M. Manousidaki, D. G. Papazoglou, M. Farsari, and S. Tzortzakis, “Abruptly autofocusing beams enable advanced multiscale photo-polymerization,” *Optica*, vol. 3, no. 5, p. 525, 2016, doi: 10.1364/optica.3.000525.

[3] K. Terzaki *et al.*, “3D conducting nanostructures fabricated using direct laser writing,” *Opt. Mater. Express*, vol. 1, no. 4, p. 586, 2011, doi: 10.1364/ome.1.000586.

[4] PhotonicsWiki, “Two Photon Absorption PhotonicsWiki,” *PhotonicsWiki*, vol. 49, no. 3, pp. 1–13, 2018, [Online]. Available: http://photonicswiki.org/index.php?title=Two_Photon_Absorption.

[5] M. Farsari, M. Vamvakaki, and B. N. Chichkov, “Multiphoton polymerization of hybrid materials,” *J. Opt.*, vol. 12, no. 12, 2010, doi: 10.1088/2040-8978/12/12/124001.

[6] A. Selimis, V. Mironov, and M. Farsari, “Direct laser writing: Principles and materials for scaffold 3D printing,” *Microelectronic Engineering*, vol. 132. Elsevier B.V., pp. 83–89, Jan. 25, 2015, doi: 10.1016/j.mee.2014.10.001.

[7] B. S. Haq, H. U. Khan, K. Alam, M. Ajmal, S. Attaullah, and I. Zari, “Determination of two-photon absorption cross sections of photosensitizers and its implications for two-photon polymerization,” *Appl. Opt.*, vol. 54, no. 1, p. 132, 2015, doi: 10.1364/ao.54.000132.

[8] K. A. I. X. Αρακτηρισμου, X. A. Y. Λικων, Σ. Παρούτη, and K. Χρυσοπούλου, “Ε α σ χ χ υ,” 2004.

[9] R. Schwalm, “Photoinitiators and Photopolymerization,” *Encycl. Mater. Sci. Technol.*, pp. 6946–6951, 2001, doi: 10.1016/b0-08-043152-6/01230-4.

[10] D. S., L. De, A. J. G. Otuka, V. Tribuzi, and C. R., “Two-Photon Polymerization Fabrication of Doped Microstructures,” *Polymerization*, 2012, doi: 10.5772/36061.

[11] J. Fischer and M. Wegener, “Three-dimensional optical laser lithography beyond the diffraction limit,” *Laser Photonics Rev.*,

vol. 7, no. 1, pp. 22–44, 2013, doi: 10.1002/lpor.201100046.

[12] Y. Jun, P. Nagpal, and D. J. Norris, “Thermally stable organic-inorganic hybrid photoresists for fabrication of photonic band gap structures with direct laser writing,” *Adv. Mater.*, vol. 20, no. 3, pp. 606–610, 2008, doi: 10.1002/adma.200702021.

[13] M. Gon, “Combining Patterned Optogenetics Using a Digital Micromirror Device and Light - sheet Whole - Brain Imaging in Behaving Fish Miguel Gonçalo Salgueiro do Paço,” no. November 2017, pp. 1–10, 2005.

[14] E. H. Waller and G. von Freymann, “Multi foci with diffraction limited resolution,” *Opt. Express*, vol. 21, no. 18, p. 21708, 2013, doi: 10.1364/oe.21.021708.

[15] E. Stankevičius, M. Gedvilas, B. Voisiat, M. Malinauskas, and G. Račiukaitis, “Fabrication of periodic micro-structures by holographic lithography,” *Lith. J. Phys.*, vol. 53, no. 4, pp. 227–237, 2013, doi: 10.3952/physics.v53i4.2765.

[16] L. N. Hazra, “Laser beam shaping,” *2008 2nd Natl. Work. Adv. Optoelectron. Mater. Devices, AOMD 2008*, pp. 108–109, 2008, doi: 10.1364/opn.14.4.000030.

[17] F. M. Dickey, “Laser beam shaping techniques,” pp. 338–348, 2004, doi: 10.1117/12.407361.

[18] D. Papazoglou, “Wavefront shaping,” 2013.

[19] N. Franata, F. P. Sari, L. Hakim, A. Sudarmaji, Handoyo, and D. Handoko, “4F Imaging System Method To Determine Optical Properties of Thin Film Magnetic Material,” vol. 2202, no. December, 2019, doi: 10.1063/1.5141642.

[20] C. Rosales-Guzmán and A. Forbes, *How to Shape Light with Spatial Light Modulators*. 2017.

[21] S. D. Gittard, A. Nguyen, K. Obata, A. Koroleva, R. J. Narayan, and B. N. Chichkov, “Fabrication of microscale medical devices by two-photon polymerization with multiple foci via a spatial light modulator,” *Biomed. Opt. Express*, vol. 2, no. 11, p. 3167, 2011, doi: 10.1364/boe.2.003167.

[22] K. Dholakia and T. Čižmár, “Shaping the future of manipulation,” *Nat. Photonics*, vol. 5, no. 6, pp. 335–342, 2011, doi: 10.1038/nphoton.2011.80.

[23] “Two-Beam Interference Equation Interferometric optical testing,” pp. 1–10.

[24] M. Vala and J. Homola, “Multiple beam interference lithography: A

tool for rapid fabrication of plasmonic arrays of arbitrary shaped nanomotifs," *Opt. Express*, vol. 24, no. 14, p. 15656, 2016, doi: 10.1364/oe.24.015656.

[25] J. H. Moon, J. Ford, and S. Yang, "Fabricating three-dimensional polymeric photonic structures by multi-beam interference lithography," *Polym. Adv. Technol.*, vol. 17, no. 2, pp. 83–93, 2006, doi: 10.1002/pat.663.

[26] G. M. Burrowg and T. K. Gaylord, "Multi-beam interference advances and applications: Nano-electronics, photonic crystals, metamaterials, subwavelength structures, optical trapping, and biomedical structures," *Micromachines*, vol. 2, no. 2, pp. 221–257, 2011, doi: 10.3390/mi2020221.

[27] L. Wang, Z. H. Wang, Y. H. Yu, and H. B. Sun, "Laser interference fabrication of large-area functional periodic structure surface," *Front. Mech. Eng.*, vol. 13, no. 4, pp. 493–503, 2018, doi: 10.1007/s11465-018-0507-9.

[28] X. Deng *et al.*, "Five-beam interference pattern model for laser interference lithography," *2010 IEEE Int. Conf. Inf. Autom. ICIA 2010*, no. Cd, pp. 1208–1213, 2010, doi: 10.1109/ICINFA.2010.5512128.

[29] A. Vorobiev, "Pulsed laser deposition of thin films of functional materials," *Micro- Nanoprocessig Technol.*, vol. 20, pp. 1–49, 2016, [Online]. Available: https://www.chalmers.se/en/researchinfrastructure/NFL/Documents/Lecture_9.pdf.

[30] H. Fujioka, *Pulsed Laser Deposition (PLD)*, Second Edi., vol. 3. Elsevier B.V., 2015.

[31] M. C. RAO, "Pulsed Laser Deposition — Ablation Mechanism and Applications," *Int. J. Mod. Phys. Conf. Ser.*, vol. 22, pp. 355–360, 2013, doi: 10.1142/s2010194513010362.

[32] C. N. Afonso, J. Gonzalo, R. Serna, and J. Solás, "Pulsed laser deposition for functional optical films," *Springer Ser. Opt. Sci.*, vol. 129, pp. 315–338, 2006, doi: 10.1007/978-0-387-30453-3_13.

[33] P. R. Willmott and J. R. Huber, "Pulsed laser vaporization and deposition," *Rev. Mod. Phys.*, vol. 72, no. 1, pp. 315–328, 2000, doi: 10.1103/revmodphys.72.315.

[34] R. K. Singh and J. Narayan, "Pulsed-laser evaporation technique for deposition of thin films: Physics and theoretical model," *Phys. Rev. B*, vol. 41, no. 13, pp. 8843–8859, 1990, doi: 10.1103/PhysRevB.41.8843.

[35] S. S. Harilal, B. E. Brumfield, N. L. Lahaye, K. C. Hartig, and M. C. Phillips, "Optical spectroscopy of laser-produced plasmas for standoff isotopic analysis," *Appl. Phys. Rev.*, vol. 5, no. 2, 2018, doi: 10.1063/1.5016053.

[36] P. Mandade, *Introduction, basic principles, mechanism, and challenges of photocatalysis*. Elsevier Inc., 2021.

[37] X. Yang and D. Wang, "Photocatalysis: From Fundamental Principles to Materials and Applications," *ACS Appl. Energy Mater.*, vol. 1, no. 12, pp. 6657–6693, 2018, doi: 10.1021/acsaem.8b01345.

[38] A. N. Giakoumaki *et al.*, "3D micro-structured arrays of ZnO nanorods /639/166 /639/925 /142/126 article," *Sci. Rep.*, vol. 7, no. 1, pp. 1–9, 2017, doi: 10.1038/s41598-017-02231-z.

[39] P. K. Aspoukeh, A. A. Barzinjy, and S. M. Hamad, "Synthesis, properties and uses of ZnO nanorods: a mini review," *Int. Nano Lett.*, no. 0123456789, 2021, doi: 10.1007/s40089-021-00349-7.

[40] A. Galdámez-Martinez, G. Santana, F. Güell, P. R. Martínez-Alanis, and A. Dutt, "Photoluminescence of zno nanowires: A review," *Nanomaterials*, vol. 10, no. 5, 2020, doi: 10.3390/nano10050857.

[41] A. Di Mauro, M. E. Fragalà, V. Privitera, and G. Impellizzeri, "ZnO for application in photocatalysis: From thin films to nanostructures," *Mater. Sci. Semicond. Process.*, vol. 69, no. March, pp. 44–51, 2017, doi: 10.1016/j.mssp.2017.03.029.

[42] P. K. Samanta and A. K. Bandyopadhyay, "Chemical growth of hexagonal zinc oxide nanorods and their optical properties," *Appl. Nanosci.*, vol. 2, no. 2, pp. 111–117, 2012, doi: 10.1007/s13204-011-0038-8.

[43] M. Farsari, G. Filippidis, and C. Fotakis, "Fabrication of three-dimensional structures by three-photon polymerization," *Opt. Lett.*, vol. 30, no. 23, p. 3180, 2005, doi: 10.1364/ol.30.003180.

[44] A. M. F. R. Pinto, V. B. Oliveira, and D. S. Falcão, *Experimental methods of characterization*. 2018.

[45] A. Klini, A. Manousaki, D. Anglos, and C. Fotakis, "Growth of ZnO thin films by ultraviolet pulsed-laser ablation: Study of plume dynamics," *J. Appl. Phys.*, vol. 98, no. 12, 2005, doi: 10.1063/1.2149498.

[46] M. Konstantaki, A. Klini, D. Anglos, and S. Pissadakis, "An ethanol vapor detection probe based on a ZnO nanorod coated

optical fiber long period grating," *Opt. Express*, vol. 20, no. 8, p. 8472, 2012, doi: 10.1364/oe.20.008472.

[47] T. Hellas, "UNIVERSITY OF CRETE DEPARTMENT OF PHYSICS FOUNDATION FOR RESEARCH AND TECHNOLOGY HELLAS INSTITUTE OF ELECTRONIC STRUCTURE AND LASER « Fabrication of 3D structures of ZnO nanorods for gas sensing at room temperature » IOANNIS SYNGELAKIS," no. October, 2019.

[48] G. Kenanakis and N. Katsarakis, "Chemically grown TiO2 on glass with superior photocatalytic properties," *J. Environ. Chem. Eng.*, vol. 2, no. 3, pp. 1748–1755, 2014, doi: 10.1016/j.jece.2014.07.015.

[49] A. Klini, A. Mourka, V. Dinca, C. Fotakis, and F. Claeyssens, "ZnO nanorod micropatterning via laser-induced forward transfer," *Appl. Phys. A Mater. Sci. Process.*, vol. 87, no. 1, pp. 17–22, 2007, doi: 10.1007/s00339-006-3811-x.

[50] R. Sabouni and H. Gomaa, "Photocatalytic degradation of pharmaceutical micro-pollutants using ZnO," *Environ. Sci. Pollut. Res.*, vol. 26, no. 6, pp. 5372–5380, 2019, doi: 10.1007/s11356-018-4051-2.

[51] S. L. Lachinova and M. A. Vorontsov, "Exotic laser beam engineering with coherent fiber-array systems," *J. Opt. (United Kingdom)*, vol. 15, no. 10, 2013, doi: 10.1088/2040-8978/15/10/105501.

[52] C. Maibohm, O. F. Silvestre, J. Borme, M. Sinou, K. Heggarty, and J. B. Nieder, "Multi-beam two-photon polymerization for fast large area 3D periodic structure fabrication for bioapplications," *Sci. Rep.*, vol. 10, no. 1, pp. 1–10, 2020, doi: 10.1038/s41598-020-64955-9.

[53] A. Nisar, M. Saeed, M. Muneer, M. Usman, and I. Khan, "Synthesis and characterization of ZnO decorated reduced graphene oxide (ZnO-rGO) and evaluation of its photocatalytic activity toward photodegradation of methylene blue," *Environ. Sci. Pollut. Res.*, vol. 29, no. 1, pp. 418–430, 2022, doi: 10.1007/s11356-021-13520-6.

[54] M. Yasmina, K. Mourad, S. H. Mohammed, and C. Khaoula, "Treatment heterogeneous photocatalysis; Factors influencing the photocatalytic degradation by TiO2," *Energy Procedia*, vol. 50, pp. 559–566, 2014, doi: 10.1016/j.egypro.2014.06.068.